La borsa di dottorato è stata cofinanziata con risorse del
Programma Operativo Nazionale Ricerca e Innovazione 2014-2020 (CCI 2014IT16M2OP005),
Fondo Sociale Europeo, Azione I.1 "Dottorati Innovativi con caratterizzazione Industriale"

UNIONE EUROPEA
Fondo Sociale Europeo

Ministero dell'Università e della Ricerca

PON RICERCA E INNOVAZIONE 2014 - 2020

Dottorato in Energy

Dipartimento di Ingegneria

ING-IND/33

Integrated Planning and Management Strategies for Hybrid AC/DC Microgrids: Self-Healing Capability Evaluation, Short-circuit Calculations, and Hierarchical Power Flow Optimization

IL DOTTORE

SALAR MORADI

IL COORDINATORE

Ch.ma Prof.ssa Eleonora Riva Sanseverino

IL TUTOR

Ch.mo Prof. Gaetano Zizzo

CICLO XXXVII

ANNO CONSEGUIMENTO TITOLO 2024

Abstract

The present thesis deals with various aspects related to the integrated planning and management strategies for hybrid AC/DC Microgrids, comprising Self-Healing Capability Evaluation, Short-circuit Calculations, and Hierarchical Power Flow Optimization. For this reason, five different focus areas can be identified in the thesis.

The first area of focus of the present thesis is to implement a resilience assessment in AC/DC hybrid microgrids using a stochastic simulation approach. The focus is on simulating self-healing measures such as load shedding, distributed generation control, and utilization of flexible devices like Battery Energy Storage Systems (BESS) and Electrical Vehicles (EVs) to ensure the supply of critical loads in islanded mode following a disconnection from the main AC grid due to a fault. The analysis follows a two-stage process: first, employing a Monte Carlo simulation-based stochastic approach to generate samples simulating intermittent loads, renewable energy generation, and grid faults; second, for each sample indicating islanded mode, formulating a grid-connected daily Optimal Power Flow (OPF) in Mixed-Integer Linear Programming (MILP) form. This aims to minimize operation costs by optimizing the withdrawal of the State of Charge (SoC) of stationery and traction batteries and electrical vehicles before microgrids transition to islanded mode. The resilience of islanded microgrids is evaluated through various indices. Additionally, different strategies are explored for modelling the behaviour of two types of electrical vehicles, V1G and V2G. Simulation results indicate that distributed generation and flexible devices may enhance resilience in islanded microgrids, although optimal daily planning in grid-connected mode could have adverse effects due to the limited energy availability of flexible devices at the moment of islanding.

In the second area, a planning framework for active buildings as an Energy Nano-Grid (ENG) is presented, focusing on determining the optimal size and generation mix of distributed energy resources (DERs) and BESS. The framework considers whether the ENG should be AC or DC based on economic factors, given the increasing penetration of battery energy storage devices, EVs, and DC loads. DC ENGs are deemed potentially more useful due to their ability to reduce the number of converters, simplify interfaces for various distributed energy resources and loads, and mitigate losses associated with AC/DC energy conversion. The selection of the ENG type becomes an economic issue, encompassing investment, operation, and maintenance costs of energy resources, as well as costs and revenues for energy transactions with the upstream grid or neighbouring ENGs. This approach aims to achieve optimal load sharing. However, optimal results may be influenced by system specifications such as the ratio of DC

load at the ENG, the maximum permissible installation capacity of BESSs, and the maximum discharge power of EVs.

Furthermore, in this thesis, the growth of small-scale microgrids with diverse distributed generations has prompted a focus on their effective energy management. Herein, an energy management system is adopted to minimize the energy purchased by a hybrid AC/DC microgrid from the upstream grid, particularly during high peak-hour energy prices. The system also aims to maximize generation from renewable sources while adjusting optimal charge/discharge control strategies for flexible loads like electric vehicles and storage systems, as well as managing the supply of non-controllable loads. Additionally, peak shaving is implemented within this model without considering minimum power deviation as an objective function. Simulation of this methodology on a real-world solar-vehicle park lot at the University of Palermo demonstrates its effectiveness and practicality for microgrid operators.

In the fourth area of this thesis the focus shifts to the challenges associated with short-circuit calculations in hybrid AC/DC microgrids. The current reference standard for short-current calculations in DC systems, IEC 61660, addresses the issue by providing a mathematical formulation. However, this standard primarily considers radial DC grids and does not account for more complex systems such as meshed DC systems or hybrid AC/DC microgrids. To address this gap, a generalized approach is proposed in this thesis, which can be applied independently of the characteristics of the hybrid system. This approach is then tested on four microgrids with varying distributed sources and numbers of nodes. The results obtained from this approach are compared with those obtained by simulating the same grids using Neplan 360.

Finally, To achieve stable and reliable load flow control amid varying load, generation, and charging/discharging strategies for BESS and EVs parking facilities, a hierarchical control scheme is proposed. Specifically, the thesis introduces an hourly power flow (PF) analysis within an Energy Management System (EMS) designed for AC/DC Hybrid Microgrids interconnected via an Interlinking Converter (IC) in grid-connected and islanded modes. This framework operates within a two-level hierarchically controlled platform. At the top level, tertiary control optimizes DGs' reference power for generation and consumption, thereby minimizing power purchase costs and load shedding in grid-connected and islanded modes, respectively. DG converters employ current control mode to share their power references as the primary controller. While no secondary controller is adopted, the battery energy storage system in islanded mode utilizes P/Q droop control to maintain voltage and frequency in the AC subsystem. Power sharing between AC and DC sub-grids through IC is determined by the difference between AC grid frequency and DC link voltage. The integration of controlled converters' buses into PF equations enables solving the unified system using the traditional Newton-Raphson (NR) method. A segment of a real distribution grid planned for installation in Italy under the HYPERRIDE project serves as a case study. Comparison with MATLAB/Simulink results confirm the effectiveness, precision, and convergence speed of the proposed model and control schemes, thereby demonstrating efficient load distribution and voltage/frequency restoration in islanded mode.

Table of Contents

List of Figures

List of Tables

Chapter 1 Introduction

In recent decades, international decarburization goals, infrastructure development, demand side management, socioeconomic issues, and the advent of new technologies such as renewable-based energy sources, battery energy storage systems (BESSs) as well as electrical vehicles (EVs), have increased interests to rebuilt traditional power systems. Microgrids, which are self-controlled networks that can operate in both grid-connected and isolated modes, are a practical approach to handle this challenge [1, 2].

Although the traditional AC power system has been the most developed system in the past few decades and many of our existing loads are of AC in nature, the appearance of power electronics and RESs with DC power generation, such as solar and fuel cells, has led to DC supply implementation in modern grids. Today, the modern appliances — laptops, mobiles, remote controllers, EVs, etc. are operating on DC supply that facilitates easy control without power factor, phase sequence, power angle and frequency issues [3]. AC/DC microgrids offer a promising solution for enhancing the resilience, efficiency, and flexibility of power distribution systems. By combining both alternating current (AC) and direct current (DC) technologies, these microgrids can integrate various distributed energy resources (DERs), storage systems, and electric vehicles parking facilities to create a more robust and adaptable energy infrastructure.

Over the past decade, the concepts of DC and hybrid AC/DC microgrids have become a popular topic among engineers, fuelling the debate on pros and cons of transforming an AC distribution system into a DC. This matter has been examined from different perspectives and by considering structural, design, and operational concerns. As an example, in [4] and [5], the authors present a comprehensive review of power architectures, applications, and standardization issues, control strategies and stabilization techniques for DC microgrids. The voltage control issue is discussed in [6], where the authors propose an energy management strategy of active distribution systems with a grid-connected DC microgrid, as well as for an isolated DC microgrid with hybrid energy resources. In [7], a power architecture for residential buildings consisting in a multilevel DC microgrid is presented, together with a method for maximizing the energy efficiency of parallel DC/DC converters. In [8], a microgrid based on solar PV-battery energy storage with a multifunctional voltage source converter is presented.

In [9], a new and more flexible architecture for hybrid AC/DC microgrids with a multi-port interconnected converter is proposed. Finally, in [10] and [11] a simulation analysis for assessing the reliability of AC/DC hybrid microgrids is performed on four test grids and some system's indicators are assessed.

One of the key benefits of AC/DC microgrids is their ability to optimize energy distribution and management. With the capability to support both AC and DC loads, these microgrids can effectively balance supply and demand, utilize renewable energy sources more efficiently, and mitigate grid instability issues [12, 13].

Additionally, AC/DC microgrids offer improved energy conversion efficiency and reduced power losses compared to traditional AC-only grids. By allowing for direct integration of DC sources such as solar panels and batteries, these microgrids can minimize the need for multiple conversions between AC and DC, thereby improving overall system efficiency [12-14].

Furthermore, AC/DC microgrids enable greater flexibility and resilience in power distribution. With the ability to operate in both grid-connected and islanded modes, these microgrids can continue supplying power to critical loads even during grid outages or emergencies. This resilience is further enhanced by the decentralized nature of microgrids, which reduces reliance on centralized power generation and distribution infrastructure [15].

Despite these benefits, AC/DC microgrids also face several challenges that need to be addressed for widespread adoption. These challenges include interoperability issues between AC and DC systems, standardization of equipment and communication protocols, and the development of advanced control and energy management strategies to optimize microgrid operation [13-16].

Each subsequent subsection deals with the challenges and significance addressed in the papers published during the three-year PhD programme. These study areas include self-healing capability analysis, within the context of resilience, in AC/DC hybrid microgrids, planning and optimizing energy management in small-scale AC/DC microgrids, known as nano-grids, short circuit calculation, and hierarchically controlled power-flow-based energy management in AC/DC hybrid microgrids.

1.1 Self-healing capability analysis

1.1.1 Challenges

With the advent of modern AC/DC hybrid microgrids, new challenges have arisen especially in term of sustainable power supply. Self-healing capability assessment is one of the most significant issues. In particular, it is fundamental to find out to what extent a smart hybrid microgrid in island mode is capable to provide customers with safe electrical energy in emergencies and in different energy scenarios. Self-healing capability is one of the main features of smart distribution systems and an effective way to increase the network reliability by having recourse to the control of flexible loads, renewable energy sources (RESs), energy storage systems and electrical vehicles in an emergency due to a fault causing the interruption of supply from the main grid. So, it appears to be critical to define some resilience indices for assessing the effects of the self-healing measures mentioned above. In this context, an important challenge is posed by the intermitted behaviour of RESs generation, loads, and the changing state of charge (SoC) of ESSs and EVs which must be considered to obtain a more realistic result from the analysis.

1.1.2 Literature review

For better understanding the importance of the present analysis, it must be analysed the state of the art. In [17], authors try to implement a new networked microgrids formation which aims to minimize unused generation capacity in islanded mode through a nested restoration decision system. Energy exchange in this paper is based on a layered control strategy from outer layers to inner ones. In [18], a new self-healing and operation strategy analysis of distribution networks are performed using a stochastic rolling-horizon optimization in grid-connected mode to make an optimal decision for sectionalizing isolated sections into self-adequate microgrids. In [19-21], the authors present self-healing measures such as generation re-dispatch, load shedding and network reconfiguration. This problem is optimized and solved using mixed-integer quadratic/linear programming to obtain an optimal island switching. In [22], the authors propose an operational plan for performing an optimum self-healing actions including load shedding, system reconfiguration and Distributed Generation (DG) output control, considering self-adequacy, total energy losses, and total supplied loads based on their priority. Both planning and real-time phase’s restoration as self-healing actions are combined into one optimization problem to respond to contingency situations in [23]. The works [24, 25] propose self-healing capabilities by coordination strategy of wind and pumped-storage hydro units in restoration phase and speeding up the recovery process using partitioning islanded power grid and considering technical limits, respectively. A two-layer metaheuristic algorithm is proposed in [26] for the optimal operation of smart distribution networks in self-healing mode considering wind turbines and energy storage systems. In the first layer, a graph theory finds an optimal formation, while the second one aims to find the optimal energy management. The works [27, 28] propose a Fuzzy multi-agent system applied in distribution networks to restore the maximum loads and minimize the number of switching time intervals. The works [29, 30] implement a decentralized two-layer Energy Management System (EMS) for a networked microgrid which operates independently. In emergency analysis, EMSs in both layers make the optimal decision to supply the on-emergency microgrid through an average consensus algorithm and a bi-level stochastic optimization algorithm, respectively. A heuristic algorithm has been proposed in [31], which presents self-healing strategy to mitigate cyberattacks. The work [32] employs a four-layer multiagent concept including different energy management and control strategies as self-healing capabilities to improve dynamic performance of microgrids. Finally, in [10, 11] a simulation analysis is presented, and some reliability indices are defined for three different hybrid AC/DC microgrids showing the behavior of the microgrids in islanded modes in different energy scenarios. Table 1-1 represents comparison between some of these works indicating their methods, advantages, and disadvantages.

1.2 Optimal Nano-grid planning

1.2.1 Aims and scopes

With the advent of new technologies such as renewable-based micro-energy sources, energy storage systems and small-scale co-generations in the building sector, there is a need for a systemic approach to the planning of building energy systems. The whole systems approach involves evaluating the various components of the system and rethinking the relationships between each of them and even redesigning the system. Confidently, such a complex energy system, faces conflicting challenges of security, equity, and sustainability, which are often referred to as the energy trilemma (see **Error! Reference source not found.**) [33-35].

Table 1-1. Previous works comparison.

Ref. No.	Method	Advantages	Disadvantages
[17]	Nested Restoration Decision System (minimizing unused DGs output in microgrids)	• Apply to complex networked microgrids • Increase resilience in island mode • Facilitate frequency and voltage restoration in island mode	• Not consider intermittent nature of RESs and loads • Not apply to whole a day, so not analysis the effect of different consumption cases • Not consider RESs and EVs • Applicable only to AC grids

[18]	Stochastic rolling-horizon optimization to sectionalize	• Using dispatchable DGs and controlling them in islanded mode • Apply to networked microgrids • Self-healing assessment for multiple faults	• Not consider EVs • Applicable only to AC grids • Not evaluate how different DGs capacity may affect the goals.
[19]	re-dispatch, load shedding and network reconfiguration using mixed-integer quadratic programming	• Apply to active multi microgrids enabling buying/selling energy from/to the main grid • To assess different generation and load scenarios	• Not consider intermittent nature of RESs and loads • Not consider RESs and EVs • Applicable only to AC grids
[20, 21]	re-dispatch, load shedding and network reconfiguration using mixed-integer linear programming	• Multi-objective optimization • Comparison of different methods • Control of technical parameters like voltage and frequency	• Not consider RESs, ESS and EVs • Not considering the intermittent nature of loads • Applicable only to AC grids
[22]	re-dispatch, load shedding and network reconfiguration using daily optimal power flow	• Probabilistic generation and load model • Different control strategies	• Not consider EVs • Applicable only to AC grids
[25, 26]	Two-stage robust optimization	• Fast and reliable self-healing process • Cover comprehensive restoration process • To address uncertainty for wind generation • Voltage stability assessment	• Just consider wind farm and hydro pump storage system • Not evaluate uncertainty for load • Applicable only to AC grids
[27]	Mixed-integer programming for network partitioning	• Taking into account network constraint • Implement RESs and storage system • Load, fault and generation estimation • To handle technical tasks like feeders' congestion, voltage violations, active and reactive power devices coordination • To analysis the importance of a communication protocol system	• Not to take into account EVs • Use flexible sources discharge only in off-grid mode • Applicable only to AC grids
[28, 29]	Two-layered metaheuristic algorithm for optimal formation and optimal DERs allocation		• Not consider RESs and flexible sources • Not address load and fault uncertainty • Not implementing energy management
[30, 32]	Two-layered optimal power flow	• To control in both normal and self-healing modes • Application of multiple faults • Different energy scenario assessment	• Evaluating self-healing mode only for a few times slots • Not including EVs • Applicable only to AC grids
[31]	Four-layered agent-based control scheme	• Real-time monitoring • Dynamic performance assessment • Control scheme for all component	• Self-healing mode is evaluated only for a few hours • EVs are not included • Applicable only to AC grids

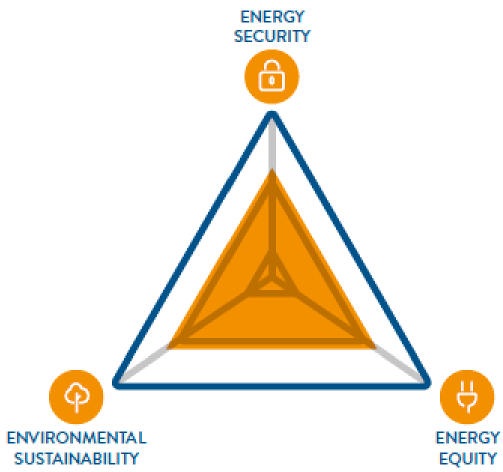

Figure 1-1. The energy trilemma triangle [33].

Nowadays, buildings are responsible for about 40% of carbon emissions and any solution to the energy crisis will have to address the issue of energy use in buildings [36]. Recent developments in smart building technologies clearly show that the buildings of the future have the potential to be active and energy self-sufficient entities which, when connected with other active buildings or to the upstream electricity grid, could have the ability to trade energy [37, 38]. To enable energy resilient communities that are powered by solar and wind plants and are able to share energy with neighbours and transport systems, a comprehensive techno-economic framework for the optimal planning and load sharing in energy management system (as a tertiary level controller) is proposed for the buildings as an Energy Nano-Grids (ENG) that can actively participate in the two-vector energy and transport system.

1.2.2 Challenges

The main point of the challenge is to decide on the optimal type of the building-based nano-grid, either AC or DC, based on system specifications such as the DC load ratio at the ENG, the maximum capacity of the installed BESs devices and the maximum energy that EVs can deliver to the ENG or the upstream network; thus, determining the optimal mix of solar and wind power (S and WP) generators and BESs as generation portfolio.

1.2.3 Literature review

Table 1-2 presents a taxonomy of existing approaches where previous research is reviewed and compared. In [39], a networked nanogrid and a battery swapping station (BSS) are considered where nanogrids can share their energy surplus or store it at the BSS to supply power to electric vehicles during peak hours. One of the challenging issues in this study is that energy must be transmitted to the BSS by the delivery system with an increase in the operation and investment costs. The study in [40] presents a planning model for microgrids connected to the upstream grid to measure the optimal size, generation mix of distributed energy resources (DERs) and type of the microgrid. The work evaluates how various factors, such as the entity of the DC and of the critical load and converter efficiency, determine whether microgrids should be DC or AC. In [41], authors developed the proposed model in [40] and show that in some cases, hybrid AC/DC microgrids can be more economical than other types by reducing the number of converters. In ref. [42], power and voltage control of a hybrid building nanogrid with two AC and DC buses are performed in both grid-connected and off-grid states. In [43], residential units are represented as energy hubs, so, in addition to electrical components, the optimal structural dimensioning of the cogeneration unit, gas boiler and heat storage systems must be considered. Some residential DC nanogrids connected to each other and to the main grid are illustrated in [44]. The import and export of electricity is controlled by an online cyber-physical approach, emulated by Lyapunov optimization. The market-based advantages of nanogrids with photovoltaic energy storage systems are discussed in [45]. In [46], different types of renewable and non-renewable resources like wind turbines, photovoltaic (PV) systems, and fuel cells are taken into consideration in grid-connected nanogrids. In contrast to other studies, the costs of environmental damage from pollutant gases and battery power losses are taken into account in the optimization of the operation management process. A new multi-objective optimization model for energy management in microgrid/nanogrid is proposed in [47] to determine the time of buying or selling electricity to or from the main grid. Ref [48] aims to gain optimal daily power schedule for energy storage systems in microgrids, while the uncertainties associated with load and RESs' available power as well as the time and duration of unscheduled islanding events are considered. In [49] a robust planning is depicted to determine the optimal expansion of distribution networks with electric vehicle penetration, where the objectives are the expansion/construction of substations and/ or charging stations for electric vehicles and the determination of the capacity of renewable resources. The main feature of this study is that the uncertainty of the load and EV demand, the level of which changes in various time intervals, is modelled through a normal distribution variable, so a scenario-based model such as Monte Carlo simulation is required to solve the program. Ref [50] presents a dynamic programming (DP) technique to optimize load sharing in solar-based DC nanogrids in presence of battery storage. In addition to an optimal load sharing, that paper achieves maximum availability of the solar energy system, minimum fuel consumption and an increase in the battery life cycle. Kumar.J. et al. have published some recent research regarding energy management in DC and hybrid microgrids [51-54]. In references [51] and [52], a control based energy management is implemented for a mini and vast DC microgrid respectively, where Maximum Power Point Tracking (MPPT) algorithm is applied to PV system to provide high utilization, and charging/discharging of battery storage system and super capacitors are controlled to respond to dc voltage regulation/load changing and fluctuation, respectively. These works consider only DC nanogrid, where lower control level (usually is called secondary level) is conducted as energy management system, and upper level that includes planning, generations' size and mix are not modeled. However, in [53], authors have proposed a new configuration for DC microgrids in isolated communities like a village, where the system aims to utilize unused stored water to generate electricity through solar pumping units. The same controllers as those in [51, 52] are characterized, and numerical analysis is done for designing the size of water tank, pumps, PV arrays, and small batteries, whereas economic study has been ignored. Ref. [54], however, provides a more comprehensive approach to determine the most optimized combination of AC and DC mini grids in hilly districts in India, so that minimizes the total costs. The objective function incorporates environmental and reliability-based constraints, and the program is solved using Genetic algorithm.

Table 1-2. Taxonomy of planning and energy management of Nanogrids

References	Network level	Planning result			Bus type analysis	BES penetration	EVs penetration	Mathematical modeling
		Energy management	Optimal sizing	Generation mix				
[39]	nanogrid	✓	✓			✓		MILP
[40]	microgrid		✓	✓	✓	✓		MILP
[41]	microgrid		✓	✓	✓	✓		MILP
[42]	nanogrid	✓				✓		
[43]	nanogrid	✓	✓					NLP
[44]	nanogrid	✓						
[45]	nanogrid		✓			✓		LO
[46]	nanogrid	✓				✓		MO
[47]	nanogrid	✓				✓		LP
[48]	microgrid	✓				✓		MILP
[49]	EDS		✓	✓			✓	MILP
[50]	nanogrid	✓				✓		DP
[51]	nanogrid	✓				✓		
[52]	microgrid	✓				✓		
[53]	microgrid	✓	✓			✓		
[54]	nanogrid	✓		✓	✓			GA
This thesis	nanogrid	✓	✓	✓	✓	✓	✓	MILP

LO= Lyapunov Optimization MO= Multi-Objective EDS= Electrical Distribution Systems DP= Dynamic Programming GA=Genetic Algorithm

1.3 Energy management in AC/DC nanogrids

1.3.1 Challenges

In recent years, new technologies such as flexible and controllable electrical vehicles (EVs), battery energy storage systems (BESSs), distributed generations (DGs) and renewable sources (RS) like solar and wind sources, have made traditional electricity grids smaller and smaller on the microgrid (MG) scale [55]. Such grids can operate in both grid-connected and islanding modes. Components mentioned above can supply load demand, deliver energy to the main grid, and save energy to use at peak hours to shave load profile and reduce the cost of purchasing energy from the upstream network. Anyway, due to intermitted behaviour of these sources, especially EVs demand profile, loads, and power generation of photovoltaic (PV) systems, the challenges in energy management have increased, in addition to other technical challenges [6].

1.3.2 Literature review

Many researchers have been working on energy management in different scales of microgrids such as small scales and home area ones. In [56], a home area energy management has been applied to a home to allocate day-ahead electrical and thermal energy sources to both controllable and non-controllable loads, considering minimum energy cost. This study considers user behaviour and preferences, weather conditions and social factors as constraints, modelled by probabilistic and random factors. The study in [57] proposes a model for maximizing social welfare of customers in a microgrid by defining controllable and uncontrollable appliances. A two-stage energy management system for multi grid-connected microgrids is carried out in [58], in which all MGs are controlled by their own controller and then by the central controller as the first stage to gain a day-ahead economical dispatch. After that, in a second stage, a real time optimal dispatch is done considering the results of the first stage to minimize the imbalance cost between day-ahead and real time models. The authors of [59] allocate an intelligent agent for each component like EVs, renewable sources, and loads. The aim is to manage charging and discharging rate/time for EVs so that they should be charging from the renewable energy resources. The study in [60] provides a review of home energy management systems focusing on their challenges and complexities such as uncertainty, multiobjective scheduling, and computational considerations. In [61], flexible loads and renewable sources in a smart home are all managed for a minimum energy cost, in the first stage, and then to shave peak load in the second stage. Battery energy storage is adopted in [62] to shave peak load and mitigate unbalanced voltage in microgrids due to renewable energy resources. In [63], three control strategies, including noncontrollable, controllable, and intelligent, were evaluated for electric vehicle charging, and a modified harmonic search algorithm was used to address optimization with uncertainties in loads, generations, and energy prices. Energy management system in [64] applies a rapid control scheme that control functional parameters of power electronic converters connecting wind and solar system to a small-scale microgrid.

1.4 Short-circuit calculations

1.4.1 Motivation of the Research and Research Gap

In this context, the topic of calculating short-circuit currents in DC networks is of interest. The standard IEC 61660 [65] proposes a short-circuit current calculation methodology but given the age of this document the most recent developments in technology and, among other things, the simultaneous presence of AC and DC sources, are not considered. The methodology proposed in this thesis tries to fill this research gaps due to the increasing importance that hybrid AC/DC systems are gaining in modern distribution grids.

1.4.2 Background and Related Works

With the aid of a power grid simulation software, some authors have tried to overcome the limitations of [65] and have proposed improvements based on simulation results. In [66], the authors develop an original package of programs used for the analysis and rating of DC protective devices in power systems. In [67, 68], two different modeling approaches to evaluate DC-side short-circuit currents in DC distribution systems fed by rectifiers are presented and validated by a time-domain simulation. The above-cited works present useful formulae that could be integrated in the IEC 61660 approach when DC distribution systems are applied to microgrids operating in island mode. Reference [69] presents an algebraic model to approximate the DC short-circuit current contribution of converters without DC fault ride-through capability. In [70], the authors analyze the limits in the application of the IEC 61660 standard to HVDC systems. In [71], the author shows that the equations of the IEC 61660 standard, originally for low-voltage (LV) systems, can also be applied to medium voltage (MV) DC networks and discusses some limitations of the standard. In [72], HVDC systems in short-circuit conditions are studied in the case of dual inverters with dual DC-link; however, the authors, although providing an interesting description of the control system, do not consider these devices in a more general methodology for calculating DC short-circuit currents. The research work in [73] proposes a fault current calculation method for DC railways. The paper presents a method to model in Matlab/Simulink railway substations, trackside paralleling huts, wayside energy storage devices, track feeders (positive and negative), overhead contact systems, running rails, and rail-to-earth resistance. The results of the short-circuit calculation are compared with those obtained from the simplified formulas of the international standard EN 50123-1 standard for DC railway systems [74]. In [75], the authors propose the wavelet transform to extract high-frequency components of fault currents to identify internal and external faults in VSC-HVDC grids. In addition, to design a protection circuit breaker in DC side, authors use the instantaneous voltage polarity difference of the current limiting reactor to determine the fault direction.

Some further steps in the simulations of DC short-circuits are done in [76] and [77]. In the first paper, the authors present an approach and some formulae for short-circuit calculation in a DC system in the case of line-to-line and line-to-ground faults and validate the results with Matlab/Simulink. In the second paper, a mathematical model and the related experimental validation are presented for short-circuit calculations in DC grids supplied by hybrid AC/DC power supply generators. The research work in [78] tries to distinguish steady-state, transient and fault operation in low voltage DC microgrids supplied by PV and battery storage systems. The proposed algorithm calculates residual current in voltage source converters and load branches, while not consider the effect of generation units. The models proposed in [70], [79] are compared to simulation results. The prior adopted a mathematic model to calculate short-circuit current in multiterminal DC grid using simplified converters and overhead line circuits, and the second one calculates short circuit current in HVDC systems considering IEC 61660. In [80], the authors model a DC-side bipolar fault current in steady-state stage for modular multilevel converters connected to AC system. Finally, in [81], an approach to extend the IEC 61660 standard to meshed systems is proposed.

All the above-mentioned works deals with the modelling of specific components of the DC system, with the dynamic behaviour of the system during the fault or propose methods that are used for DC grids with a single source.

1.5 Hierarchically controlled power-flow-based energy management

1.5.1 Challenges

Obviously, power flow (PF) analysis, as the elementary tool in power systems, plays a significant role for other important assessments such as control, protection, design, planning, and energy management, among others. Unlike the conventional power systems, where power flow is characterized using known bus types, in AC/DC hybrid microgrids, particularly in islanded mode, due to the limit and non-robust generation source as a slack bus to keep the voltage and frequency of the network at the rated values, the corresponding buses are not categorized into traditional ones. Additionally, interconnection and power sharing between AC and DC subgrids needs to adopt a proper control scheme, preventing buses to fall into PQ or PV buses [82-84]. Therefore, a comprehensive control framework is integrated to power flow analysis in coupled AC/DC microgrids. Since solving control-integrated PF in power management prospective, it is crucial to implement hierarchical control scheme, and to adopt a proper power flow calculation technique. Therefore, literature below discusses different inner control layers as primary and secondary controllers, top layer playing the role of power management, and PF analysis techniques respectively, in various AC/DC hybrid networks topologies.

1.5.2 Literature review

Power flow analysis in controlled hybrid microgrids has increased researchers' interests in the last decade. They mainly have focused on the islanded operation mode. To PF assessment in AC/DC hybrid microgrids, authors in [85-93] have tried to define new controlled buses for both AC and DC buses in islanded mode, applying well-known droop control. In [85], authors integrated a two-level, primary, and secondary, well-known drooped-based control schemes into traditional Newton-Raphson (NR) power mismatch formulations for islanded AC/DC microgrid to manage power sharing among DGs and restore AC/DC voltages and frequency at point of common coupling (PCC) bus; in addition, a voltage-frequency droop controller is characterized for IC to control power sharing between both subgrids. The same droop based primary controller has been suggested in [86-88] for DG's converters and IC in PF analysis, where [86] tries to evaluate different hybrid microgrid structures, where the model is also applicable for grid-connected mode, and [87] implements the addressed controlled power flow analysis for multiple AC-DC hybrid structures. Different droop characteristics, based on the output impedance of DGs, have been included in PF mismatch equations [89], where change the Jacobian and variable matrices. In [90], popular P-ω/Q-V droops in AC grid and P-V droop in DC one are adopted in a backward-forward sweep (BFS) algorithm for calculating load flow sequentially. This approach is developed for decomposed AC and DC subgrids which are coupled using normalized V-ω droop [85, 94] for IC. Unlike works above, [91] consider Renewable Energy Sources (RESs) and storage systems in AC and DC subgrids as well. The most significant point in this work is to control charging/discharging status of storage systems in AC and DC grids through frequency and DC terminal voltage respectively. Droop characteristics and voltage reference of DG units in [92] are extracted from Optimal Power

Flow (OPF), which play as reference roles for voltage source control converters in islanded AC microgrid. A new idea is developed in [93] to control power exchange between AC and DC subgrids in grid-connected mode, where a modified unified interphase power controller is implemented, including one line power converter and one bus power converter regulating dc link voltage.

Regarding top control level, including tertiary control in the EMS framework, some authors have addressed power management [95-100]. Ref. [95] provides a comprehensive review of power management strategies in AC/DC hybrid microgrids including different system structures, different operation modes in both steady-state and transient conditions. A hierarchical energy management for storage-photovoltaic based hybrid microgrids is applied in [96], where it comprises a centralized supervisory system to decide the control scheme and power reference sets, for both islanded and grid-connected modes, to the converters' local controllers. However, [97] and [98] adopted energy management only in tertiary level, which calculates hourly optimal charging/discharging strategies for storage systems [97], and a stochastic optimal load flow is adopted in [98] to measure power sharing among DGs and RESs considering uncertainty of variables. Authors in [99] and [100] suggested hierarchically power management, where it is divided into two system-level and devise-level perspectives [99], at which the former is implemented by mixed-integer optimization program, then power reference control mode is applied to converters as the latter level. Meanwhile, [100] includes only autonomous primary and centralized secondary controllers. In addition, small-signal stability analysis is conducted to investigate the influence of the communication delays on the system stability.

In general, power flow calculations in AC/DC hybrid grids are solved using two methodologies: sequential and unified. In the former [88, 90], and [101], parameters in one system (usually in DC one) are estimated, then power flow for another one is solved, and finally estimated parameters are updated till convergence is reached. However, in the latter approach [85-87, 91], AC and DC power flow equations are solved simultaneously. Since convergence problem in sequential method might rise [102], and to have better convergence characteristics in unified one [103], power flow equations are solved as a unified system.

Almost all the works mentioned above have only considered islanded mode. Modern microgrids consist of RESs, storage systems, and modern loads such as Electrical Vehicles (EVs), where they can operate in grid-tied or islanded modes. On the one hand, the steady-state dynamics in each operation mode require specific decision making taken by the top control (tertiary level in this thesis) and might change the control scheme of some sources. On the other hand, the intermittent dynamics of RESs and EVs during a day cause changes in load supply, charging/ discharging states for BESS and EV parking lots. Therefore, a top control layer is needed for daily power flow analysis in both operating modes. A few works have studied controlled-power-flow analysis in both grid-connected and islanded operating modes [101], and [104]. These articles do not address the research gaps mentioned above, as authors propose constant power DGs in hybrid microgrids, incorporating them into power flow formulation using droop control.

Chapter 2 Self-healing capability evaluation in active islanded AC/DC hybrid microgrids

Abstract

In this chapter, the aim is to implement a resilience assessment within AC/DC hybrid microgrids using a stochastic simulation approach. Self-healing measures including load shedding, control of distributed generation, and flexible devices such as Energy Storage Systems (ESS) and Electrical Vehicles (EVs) are simulated to enable AC/DC hybrid microgrids to supply critical loads in islanded mode, assuming a disconnection of these microgrids from the main AC grid due to a fault. To perform this analysis, a two-stage process is proposed: first, a Monte-Carlo simulation-based stochastic approach is adopted to generate samples to simulate intermittent loads, power generation from Renewable Energy Sources (RESs), and fault occurrences in the upstream grid; second, for each sample indicating islanded mode, a grid-connected daily Optimal Power Flow (OPF) is formulated in Mixed-Integer Linear Programming (MILP) form based on minimizing operational costs to manage the State of Charge (SoC) of stationary and traction batteries and electric vehicles before microgrids may go to islanded mode. Finally, the resilience of islanded microgrids is evaluated through various indices. Additionally, different strategies are considered for modelling the behaviour of both types of electrical vehicles V1G and V2G. Simulation results show that distributed generation and flexible devices might improve resilience in islanded microgrids; however, optimal daily planning in grid-connected mode could affect it adversely due to the low energy available from flexible devices at the islanding moment.

With the emergence of modern AC/DC hybrid microgrids, there have been new challenges, particularly regarding sustainable power provision. An essential aspect is assessing the self-healing capability, especially concerning the ability of smart hybrid microgrids in island mode to deliver safe electrical energy to customers during emergencies and various energy scenarios. Self-healing capability stands out as a key feature of smart distribution systems, offering an effective means to enhance network reliability through the management of flexible loads, renewable energy sources (RESs), energy storage systems, and electric vehicles in the event of a fault disrupting supply from the main grid. Consequently, it is imperative to establish resilience indices for evaluating the impact of the aforementioned self-healing measures.

Within this context, a significant challenge arises from the intermittent nature of RESs generation, fluctuating loads, and the dynamic state of charge (SoC) of energy storage systems and electric vehicles, all of which must be accounted for to attain a more accurate analysis result.

In this framework, according to Table 1-1, some research gaps are discussed that have been addressed in this chapter to show the importance of applying the proposed methodology. Firstly, previous works did not take into account AC/DC microgrids self-healing capability and the impact of various energy scenarios, whereas this chapter presents a methodology for performing a comprehensive self-healing assessment for AC/DC MV/LV hybrid microgrids considering the specific characteristics of the distributed flexible resources and the impact of the energy scenario. The methodology is applied to three microgrids: an underground station, a car park, and a residential area where five energy scenarios characterized by different energy consumption, RES production, number of EVs and controllable loads are defined for assessing the self-healing capability in presence of different shares of flexible devices. The diversity of the load profiles, of the entity of the critical loads and of the flexible resources considered in the study, contribute to the novelty of the research. The scenarios refer to the years 2022, 2030 and 2040 and have been defined according to the most recent technical reports on the energy transition in Europe and Italy [105-110].

In addition, an optimal power flow (OPF) using Mixed-Integer Linear Programming (MILP), considering the connection of the main AC upstream network and proper stochastic approaches for variable parameters, is carried out to determine the SoC of ESSs and EVs before an interruption of the main MV AC grid due to a fault event by which we can recognize how optimal energy management in normal condition may affect self-healing in off-grid mode; however, other works do not calculate the SoC of flexible sources in an microgrids in this chapter are fully-equipped with all RESs and flexible sources, especially EVs that not taken account in above-mentioned works.

It is assumed that the microgrids can operate independently in islanded mode supplying with their local resources the critical loads. Furthermore, a Monte-Carlo simulation is implemented to calculate a set of resilience indices representing the capability of the islanded hybrid microgrids of supporting customer’s power supply in the different energy scenarios. These indices can be categorized into customer- energy- and microgrid-oriented groups. In brief, the main contributions of this chapter can be resumed as it follows:

- proposing a study that considers different energy scenarios for assessing the impact of the increase in the flexible energy resources on the self-healing capability;
- calculation of the SoC of ESSs and EVs as flexible units through a pre-fault daily OPF with MILP formulation, and non-critical load shedding in self-healing mode;
- defining different valuable resilience indices to show to what extent microgrids are capable of providing a reliable supply to their critical loads;
- Implementing a stochastic approach to handle intermitted nature of variables such as load and renewable energy output, and Monte-Carlo simulation to calculate the set of resilience indices.

2.1 Methodology

The methodology employed to evaluate self-healing in hybrid AC/DC microgrids comprises the steps outlined in Figure 2-1. Broadly speaking, the steps depicted in Figure 2-1 can be categorized to delineate two distinct stages of the proposed methodology.

In the first stage, a failure is assumed to occur in the main AC grid, which is simulated through random value samples called Monte-Carlo samples. Comparing the random samples to the rate of microgrid (failure rate of AC main grid [111]), island and grid-connected modes can be found out, so that if random value is less than the failure rate, it is assumed there is an islanded mode and failure in the main grid has accrued, and if it is greater than the failure rate, network operates in normal or grid-connected mode. Referring to the database from ARERA, the Italian Regulatory Authority for Energy, Networks and the Environment, the average duration of the fault is assumed 45 min for MV and LV AC distribution grids [112].

It is worth underlying that, the installed local generating capacity of each microgrid is not enough to supply all loads; therefore, when a microgrid is in islanded mode due to a failure of the main grid, the non-critical loads with high consumption are disconnected. Since the aim of this study is to evaluate the capability of hybrid microgrids of supplying critical loads during off-grid operation through RESs, load shedding, and flexible generations such as ESS and smart EVs, it is significant to identify the operation state of these resources.

Renewable energy sources' power output is completely independent from the operation modes of the network, since it depends on environment conditions, such as wind speed or solar

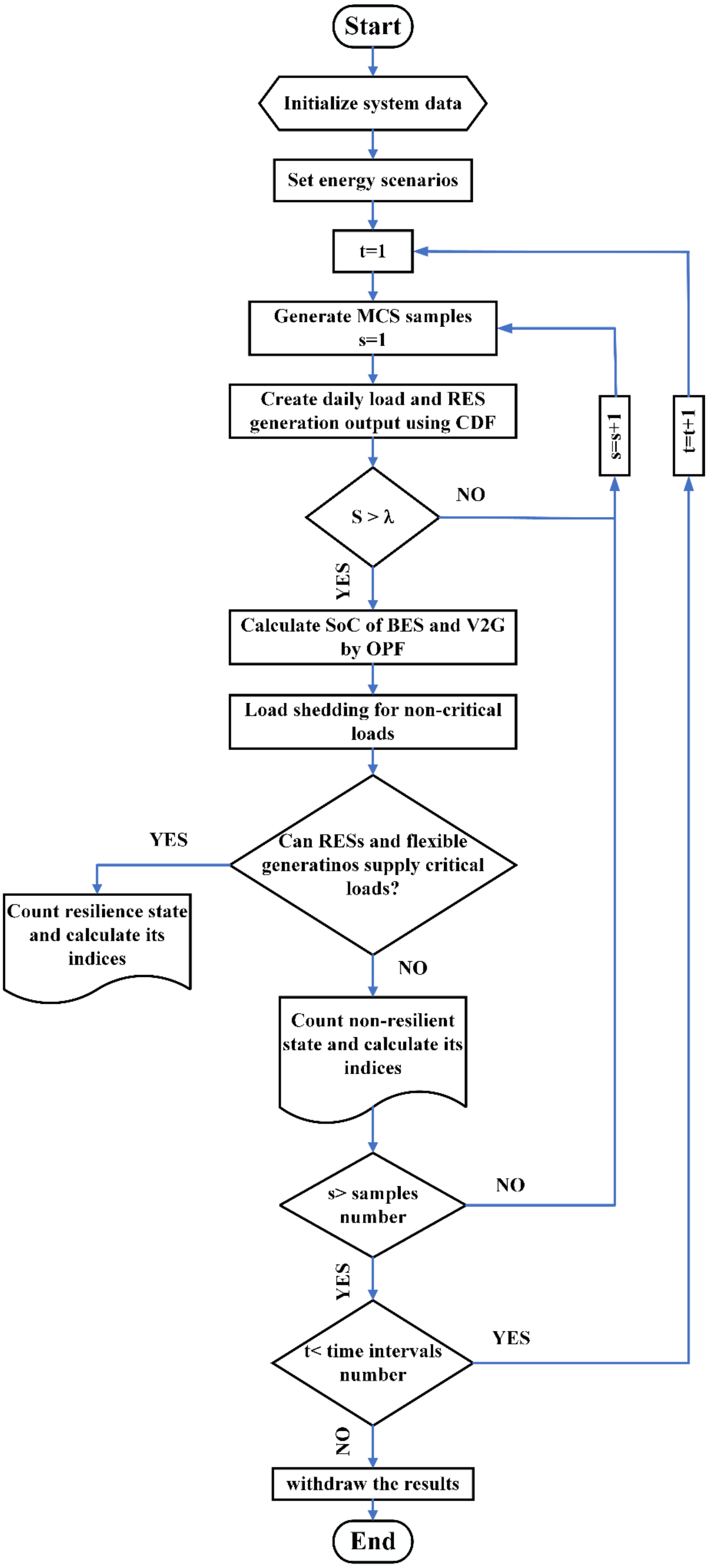

Figure 2-1. Overall process of the proposed methodology.

irradiation. Flexible resources charging/discharging states, instead, vary according to the consumption and operation mode (grid-connected or islanding) of the microgrid. Therefore, the SoC of ESSs and EVs must be calculated before the fault event occurs in the main grid. For performing this calculation, an OPF-based energy management is implemented. The OPF is formulated based on minimizing the operation cost for each time interval and random sample. There are several works addressing stochastic energy management in microgrids that one comprehensive is [113] which here simpler version is used. So, the objective function for each microgrid is:

$$C_{op} = \sum_t c_g P_g(s,t) \qquad \forall e, m, s \tag{2-1}$$

All symbols explanation is reported in Appendix 1.

Equations and inequalities (2-2) to (2-4) represent generation-related constraints. Equation (2-2) is the daily power balance for a generic microgrid; equations (2-3) and (2-4) represent the output power limit for PV and wind generators. Because the installed capacity of RES-base generators is constant and this chapter projects to analysis resilience in off-grid mode, power purchased from the AC main grid in not restricted to its limit, meaning, in grid-connected mode, microgrids' loads are surely going to be supplied, so there is no restriction in power importing from the main grid.

$$\begin{aligned} P_g(s,t) + P_{pw}(s,t) + P_w(s,t) + P_s^{dis}(s,t) + P_{v2}^{dis}(s,t) \\ = P_l(s,t) + P_s^{ch}(s,t) + P_{v2}^{ch}(s,t) \qquad \forall s,t,m,e \end{aligned} \tag{2-2}$$

$$P_{pv}(s,t) \le \eta . P_{pv}^{max}(m) \qquad \forall s,t,m,e \tag{2-3}$$

$$P_w(s,t) \le \eta . P_w^{max}(m) \qquad \forall s,t,m,e \tag{2-4}$$

Constraints (2-5) to (2-11) express ESS's operation limits. Inequalities (2-5) and (2-6) indicate that charge and discharge powers of the EES must not exceed their bounds, and (2-7) expresses the non-simultaneity of battery charging and discharging operations. Equations (2-8) and (2-9) express the hourly available energy of the ESS, while (2-10) restricts this energy to its upper and lower limits. Furthermore, equation (2-11) is introduced to ensure that the energy stored at the end of a day is equal to the energy available at the beginning of the same day.

$$I_s^{ch}(s,t).P_{ch,s}^{min} \leq P_s^{ch}(s,t) \leq I_s^{ch}(s,t).P_{ch,s}^{max} \qquad \forall s,t,m,e \tag{2-5}$$

$$I_s^{dis}(s,t).P_{dis,s}^{min} \leq P_s^{dis}(s,t) \leq I_s^{dis}(s,t).P_{dis,s}^{max} \qquad \forall s,t,m,e \tag{2-6}$$

$$I_s^{ch}(s,t) + I_s^{dis}(s,t) \leq 1 \qquad \forall s,t,m,e \tag{2-7}$$

$$E_s(s,t) = E_s(s,t-1) + P_s^{ch}(s,t) - P_s^{dis}(s,t) \qquad \forall s,t>1,m,e \tag{2-8}$$

$$E_s(s,t) = U_s(0) + P_s^{ch}(s,t) - P_s^{dis}(s,t) \qquad \forall s,t<2,m,e \tag{2-9}$$

$$E_s^{min}(m) \leq E_s(s,t) \leq E_s^{max}(m) \qquad \forall s,t,m,e \tag{2-10}$$

$$U_s(0) - \Delta U_s \leq E_s(s,t) \leq U_s(0) + \Delta U_s \qquad \forall s,t>23,m,e \tag{2-11}$$

The following equations represent the constraints for EVs. They are formulated only for V2G EVs because they are the only EVs that can be managed by the network operator with an intelligent charge/discharge strategy. It means the SoC of V2G is variable unlike V1G whose charging is imposed as an input of the problem. Equations (2-12) to (2-18) have the same definition as those for ESS above. When V2G EVs are out of the zone, there is no charge and discharge operation for their batteries, which is expressed by (2-19) and (2-20). Finally, equation (2-21) implies that V2G must have a minimum energy at their battery when they leave the parking lot.

$$I_{v2}^{ch}(s,t).P_{ch,v2}^{min} \leq P_{v2}^{ch}(s,t) \leq I_{v2}^{ch}(s,t).P_{ch,v2}^{max} \qquad \forall s,t,m,e \tag{2-12}$$

$$I_{v2}^{dis}(s,t).P_{dis,v2}^{min} \leq P_{v2}^{dis}(s,t) \leq I_{v2}^{dis}(s,t).P_{dis,v2}^{max} \qquad \forall s,t,m,e \tag{2-13}$$

$$I_{v2}^{ch}(s,t) + I_{v2}^{dis}(s,t) \leq 1 \qquad \forall s,t,m,e \tag{2-14}$$

$$E_{v2}(s,t) = E_{v2}(s,t-1) + P_{v2}^{ch}(s,t) - P_{v2}^{dis}(s,t) \qquad \forall s,t>1,m,e \tag{2-15}$$

$$E_{v2}(s,t) = U_{v2}(0) + P_{v2}^{ch}(s,t) - P_{v2}^{dis}(s,t) \qquad \forall s,t<2,m,e \tag{2-16}$$

$$E_{v2}^{min}(m) \leq E_{v2}(s,t) \leq E_{v2}^{max}(m) \qquad \forall s,t,m,e \tag{2-17}$$

$$U_{v2}(0) - \Delta U_{v2} \leq E_{v2}(s,t) \leq U_{v2}(0) + \Delta U_{v2} \qquad \forall s,t>23,m,e \tag{2-18}$$

$$P_{v2}^{ch}(s,t) = 0 \qquad \forall s,q,m,e \tag{2-19}$$

$$P_{v2}^{dis}(s,t) = 0 \qquad \forall s,q,m,e \tag{2-20}$$

$$E_{v2}(s,t) \geq N.\lambda.D \qquad \forall s, T_l, m, e \tag{2-21}$$

In this chapter a mixed-integer linear programming (MILP) formulation is considered to solve 24-hourly optimal power flow in GAMS/Cplex tool. GAMS/Cplex is a GAMS solver that allows users to combine the high level modeling capabilities of GAMS with the power of Cplex optimizers. Cplex optimizers are designed to solve large, difficult problems quickly and with minimal user intervention [114]. In the OPF problem with the contribution of flexible sources, there are integer variables such as charge/discharge of these units which cannot be done simultaneously. Therefore, mixed-integer solver is implemented to address this dilemma. In islanded mode, it is assumed that the technical parameters such as voltage and frequency are controlled by the microgrid operator. So, this chapter only analyses the microgrid capability of providing power supply to the critical loads.

In the second stage of the methodology, the SoC of ESSs and smart EVs calculated from the first stage is referred as input for the resilience assessment. A stochastic Monte-Carlo simulation generates random samples to distinguish grid-connected and islanded modes. In off-grid mode, it is proposed to find out whether available generation can supply critical loads or not. To evaluate this aspect, in island mode, it is necessary to evaluate some indicators, distinguishing between two sets. The first set consists of factors showing the resilience rate of microgrids, formulated as follows:

- The Resilience Frequency Rate (RFR) factor indicates how flexible microgrids are in supplying critical loads in island mode in a year:

$$RFR = \frac{total\ number\ of\ resilient\ samples}{total\ number\ of\ islanding\ samples} \tag{2-22}$$

The Loss of Load Expectation (*LOLE*) index shows the number of days in which microgrids are not capable to provide enough power to supply critical loads in a year in islanded mode in a microgrid:

$$LOLE = (1 - RFR).365 \tag{2-23}$$

The Resilience Duration Rate (RDR) represents the rate between the time T_r the microgrids are able to self-heal in islanded mode and the failure time in a year T_f:

$$RdR = \frac{T_r}{T_f} \tag{2-24}$$

The second set includes energy-oriented factors that imply generation status of RESs and flexible sources comparing to the energy consumed by the critical loads. These factors are defined below:

- The Renewable Energy Rate (RER) index shows the percentage of renewable sources energy available E_{RES}^{i} compared to the total energy consumed by critical load in a year E_{l}^{c} in islanded mode in a microgrid:

$$RER = \frac{E_{RES}^{i}}{E_{l}^{c}} \tag{2-25}$$

- The Flexible Energy Rate (FER) index shows the percentage of energy from flexible sources like EVs and ESSs E_{F}^{i} compared to the total energy consumed by critical load in a year E_{l}^{c} in islanded mode in a microgrid:

$$FER = \frac{E_{F}^{i}}{E_{l}^{c}} \tag{2-26}$$

- Energy not Supplied (ENS) factor which calculates the amount of energy not supplied by RESs and flexible resources in non-resilient cases during a year:

$$ENS = \sum_{i} (1 - RDR).P_{l}^{c} \tag{2-27}$$

2.2 Application to a Hybrid AC/DC Microgrids

Figure 2-2 shows a MV/LV hybrid AC/DC distribution network defined for resilience studies like those presented in [10, 11] and called “city area network”. This network is supplied by a MV 20 kV AC upstream network through transformers. AC/DC converters are installed to support DC loads power and connect photovoltaic systems and ESSs to the DC buses. As it is clear from Figure 2-2, three zones can be identified within the city area network: an underground station, a car park, and a residential area, which can be operated as three independent microgrids when they are isolated from the main grid.

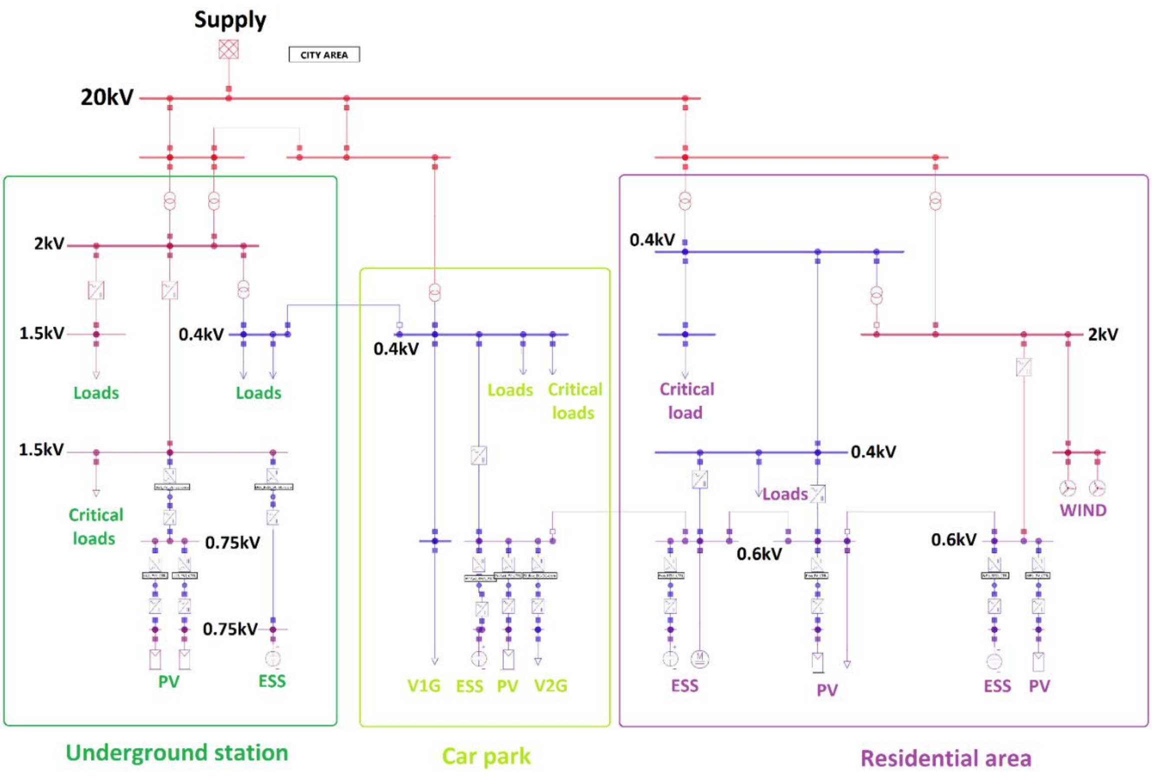

Figure 2-2. City Area Network.

The underground station includes a DC system to provide electrical energy to the traction system and its relative services like lighting, air conditioning, commercial loads, etc. furthermore, there is a 400 V AC bus to supply surface station services. The car park microgrid comprises two buses: an AC bus supplying road services such as security point, video surveillance, lighting, etc, and a DC bus connecting PV, ESS, slow and fast EVs charging stations. As regards the residential zone, a 400 kVA substation provides power to the customers and there is a DC node connecting PV, ESS, and DC load [111]. Finally, in the same zone, a wind park provides energy to the loads.

When a fault at the AC main grid occurs, if permanent, microgrids switch to off-grid operation and maintain it until service is restored or until local resources are able to supply critical loads. Assuming microgrid operators control the technical parameters like voltage and frequency, microgrids could be able to continue supplying loads through RESs, flexible resources like ESS and EVs, and load shedding. Therefore, these elements are modeled as follows to implement a simulation-based analysis.

2.2.1 Load

Daily consumption is one of the most significant uncertain variables in distribution systems. Therefore, it is vital for microgrid operators to manage this challenge in order to achieve a more realistic analysis. Probability analysis is a practical technique for obtaining a reliable estimate of these variables. According to the studies in the literature and looking at the trend of the daily consumption of the loads in the LV microgrids in Figure 2-2, a normal Probability Density Function (PDF) is the best choice to refer to load uncertainty. The PDF for the load is expressed as follows:

$$N_m(l) = \frac{1}{\sigma\sqrt{2\pi}} exp\left[-\frac{(l-\mu)^2}{2\sigma^2}\right] \tag{2-28}$$

where the mean of the load (μ) and the standard deviation (σ) can be extracted from the historical data reported in [111]. The above function is used for a Monte-Carlo simulation: it is assumed to generate a random probability number indication Cumulative Distribution Function (CDF) and return load variable at any given time using CDF inverse function.

2.2.2 Renewable Energy Sources

Photovoltaic and wind generation are other important elements which need to be modeled. In order to incorporate the RESs behavior in the microgrids' analysis, data regarding wind speed and solar irradiation are needed. Different PDFs for these types of variables have been proposed, anyway, Weibull and normal probability density function are used in this chapter for the wind speed and PV power output, respectively, as follows:

$$W(w) = \frac{\beta w^{\beta-1}}{\alpha^\beta} exp\left[-(\frac{w}{\alpha})^\beta\right] \tag{2-29}$$

$$N_m(P_{pv}) = \frac{1}{\sigma\sqrt{2\pi}} exp\left[-\frac{(P_{pv}-\mu)^2}{2\sigma^2}\right] \tag{2-30}$$

Then, for any given wind speed which is calculated from the same Monte-Carlo simulation mentioned for the load above, the corresponding wind power output can be calculated as [115]:

$$P_w = \begin{cases} 0 \quad for\ w < w_i\ and\ w > w_o \\ P_w^r\left(\frac{w-w_i}{w_r-w_i}\right) \qquad for\ \ w_i \le w \le w_r \\ P_w^r \qquad for\ \ w_r \le w \le w_o \end{cases} \tag{2-31}$$

Figure 2-3 shows the normalized daily PV generation for each month of a year assumed in the present study, which proves why normal PDF matches PV power output.

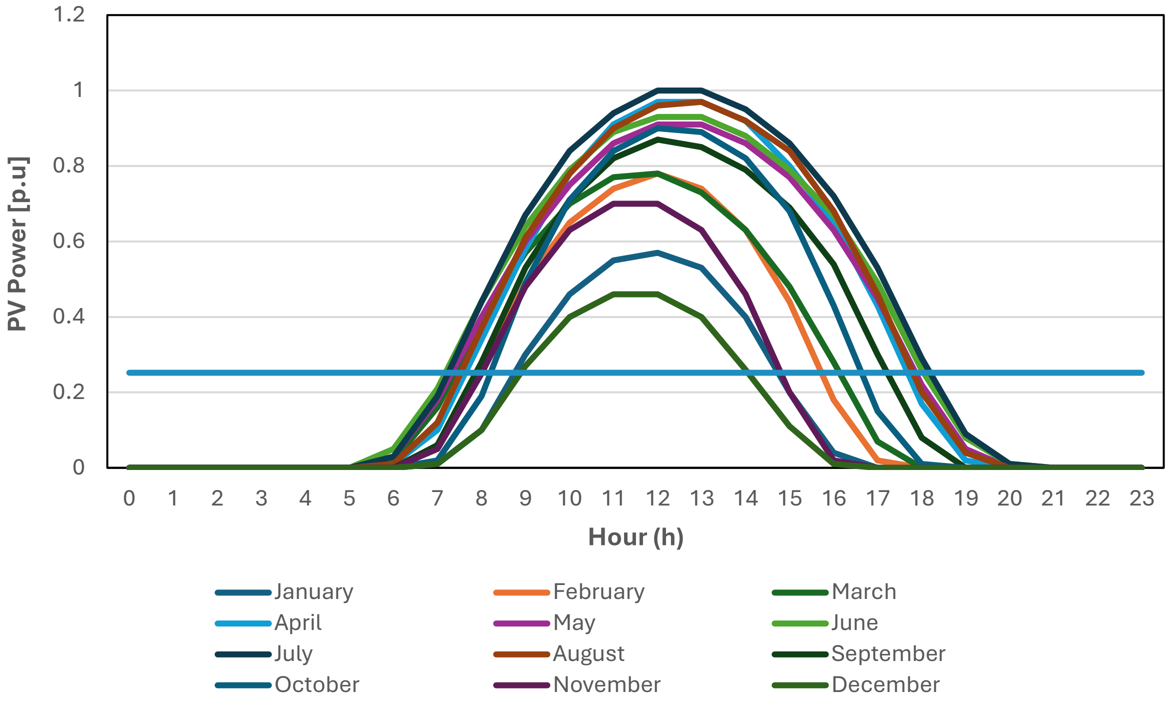

Figure 2-3. Daily PV generation at LV network.

2.2.3 Electrical Vehicles

EVs are playing an important role in demand side management issue. They are considered as flexible load and resources which can be supplied during normal operation mode or can compensate power shortage for critical loads during islanded operation mode. In this study, two types of EVs with different charge/discharge characteristics are considered:

- V1G EVs with dump charging strategy in which vehicles owners are completely free to connect and charge their vehicles whenever they want. The charging starts automatically when an EV plugs-in. Figure 2-4 shows a daily average V1G EVs consumption for different seasons in the car park microgrid;
- V2G EVs with smart charging strategy. When this strategy is adopted, owners have to accept a commitment at which they share EVs' battery when the network needs this resource at both on-grid and islanded operation modes in technical and economical perspectives.

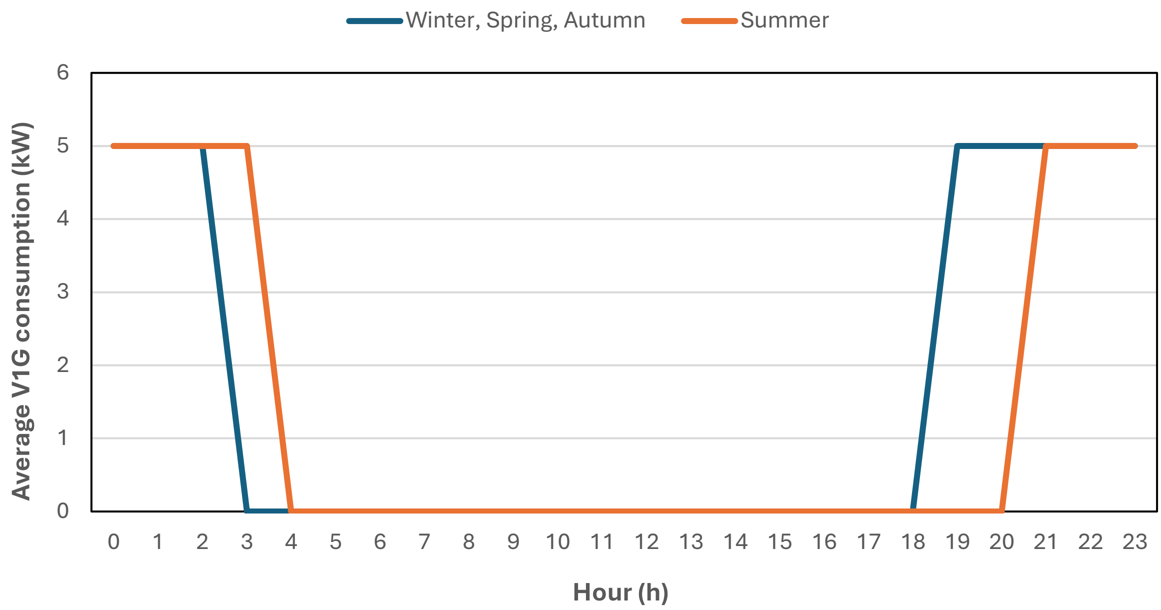

Figure 2-4. Daily V1G consumption in Car Park area.

2.2.4 Energy Scenarios

As explained in this chapter earlier, the microgrid is studied considering different energy scenarios since it is interesting to assess to what extent the increase in RES production, available flexible resources such as controllable loads, ESSs and smart EVs is able to influence the self-healing capacity of the network.

The energy scenarios have been defined by analyzing the most recent technical report on the European and Italian energy transition [105-110] and are synthetized in Table 2-1. The data in Table 2-1 are reported in p.u. so that they can be adapted to the characteristics of any microgrid. In fact, it is not so much the absolute values of the quantities involved that characterize a scenario as the ratios between the sizes of the flexible resources and the energy/power requirements of each specific microgrid. Scenario 2020 is the base scenario representing the current situation, while scenario 2030 and 2040 represents the energy scenario in the next two decades. The suffixes BC and DEC indicates two different possibilities considered for the Italian energy transaction in the PNIEC (Italian Plan for Energy and Climate [116]). In particular, BC indicates the scenario Business-as-Usual, which inertially projects current trends and is characterized by technological development based on economic merit alone, and DEC indicates the scenario Decentralized, which achieves the decarburization, RES share and energy efficiency targets and the non-binding long-term CO_2 emission targets using a logic of minimizing decarburization costs and alternative technological developments. In the following, defined the rated power of the generators, the load power, the energy consumption, and the characteristics of the flexible resources for the Scenario 2020 and for each microgrid, automatically, applying the coefficient in Table 2-1, the same data for the other scenarios will be defined.

Table 2-1. Energy scenarios.

	2020	2030BC	2030DEC	2040BC	2040DEC
Final energy consumption	1 p.u.	1.08 p.u.	1.14 p.u.	1.16 p.u.	1.26 p.u.
Energy production from RES with respect to total energy consumption	0.178 p.u.	0.212 p.u.	0.283 p.u.	0.287 p.u.	0.369 p.u.
Total RES generators rated power with respect to the total load power	0.47 p.u.	0.56 p.u.	0.70 p.u.	0.70 p.u.	0.83 p.u.
Total stationary EES rated power with respect to the total load power	8.7e-4 p.u.	1.23e-2 p.u.	1.16e-2 p.u.	8.70e-2 p.u.	8.10e-2 p.u.
Stationary storage capacity with respect to the load	1e-6 p.u.	1.12e-5 p.u.	1.07e-5 p.u.	8.03e-5 p.u.	7.42e-5 p.u.
Number of EVs	1 p.u.	83 p.u.	180 p.u.	180 p.u.	233 p.u.
Number of users participating in Demand Response programs	1 p.u.	1.000 p.u.	1000 p.u.	2500 p.u.	2500 p.u.

2.3 Numerical Results

In the simulations, it is assumed the failure rate of the MV network is 0.48 per year. All data for simulating total and critical load, electrical vehicles and battery energy storage system characteristics, PV and wind generation are taken from [112] and [111]. Referring these data, V2G vehicles with smart charge/discharge strategy leave the parking lot at 7 a.m. and arrive there at 7 p.m., with a 40 km average journey a day. V1G EVs are considered detachable load during off-grid operation. Table 2-2 shows the load, RESs and flexible resources data for the various energy scenarios in the three microgrids, calculated according to Table 2-1. In the stochastic Monte-Carlo simulation 1000 random samples are considered. Since the islanding mode takes 45 minutes, time horizon is 15-minute intervals in the OPF simulation. Therefore, there are 1000×96 samples in the proposed Mont-Carlo simulation.

Table 2-2. City Area Energy Scenarios

	Energy Scenarios for Underground Microgrid				
	2020	2030 BC	2030 DEC	2040 BC	2040 DEC

Daily energy consumption [kWh]	3694	3694	3694	3694	3694
PV systems rated power [kW]	109	130	170	175	175
ESS maximum capacity [kWh]	500	500	500	500	500
	Energy Scenarios for Car Park Microgrid				
	2020	2030 BC	2030 DEC	2040 BC	2040 DEC
Daily energy consumption [kWh]	653.5	973.5	973.5	1993	1993
PV systems rated power [kW]	20	35	45	90	120
ESS maximum capacity [kWh]	50	50	50	50	50
V1G EV [n]	5	10	10	25	25
V2G EV [n]	5	10	10	25	25
	Energy Scenarios for Residential area Microgrid				
	2020	2030 BC	2030 DEC	2040 BC	2040 DEC
Daily energy consumption [kWh]	3696	3991.68	4213.44	4287.36	4656.96
PV systems rated power [kW]	33	43	60	62	87
Wind system rated power [kW]	33	43	60	62	87
ESS maximum capacity [kWh]	540	600	580	580	620

Table 2-3 to Table 2-5 report the indices defined in section 2.1 and calculated for the various energy scenarios and for the three microgrids.

Table 2-3. Resilience indices for Underground area.

Underground Area						
Scenarios	*RFR*	*LOLE* [day]	*RDR*	*RER*	*FER*	*ENS* [GW]
2020	0.59	149.1	0.65	0.2	0.23	7.6
2030 BC	0.74	93.6	0.79	0.24	0.36	2.6
2030 DEC	0.8	70.3	0.84	0.31	0.46	1.19
2040 BC	0.86	50	0.88	0.31	0.48	0.6
2040 DEC	0.86	50	0.88	0.31	0.48	0.6

Table 2-4. Resilience indices for Car Park area.

Car Park Area						
Scenarios	*RFR*	*LOLE* [day]	*RDR*	*RER*	*FER*	*ENS* [GW]
2020	0.5	183.6	0.62	0.43	0.5	0.5
2030 BC	0.66	122.5	0.8	0.68	0.47	0.1
2030 DEC	0.56	158.9	0.77	0.9	0.25	0.12
2040 BC	0.81	66.3	0.92	1.4	0.36	0.05
2040 DEC	0.92	22.3	0.97	1.9	0.32	0.01

Table 2-5. Resilience indices for Residential area.

Residential Area						
Scenarios	*RFR*	*LOLE* [day]	*RDR*	*RER*	*FER*	*ENS* [GW]
2020	0.9	36	0.93	0.11	0.47	0.13
2030 BC	0.82	64.5	0.87	0.14	0.42	0.78
2030 DEC	0.87	44.7	0.91	0.18	0.42	0.27
2040 BC	0.82	63.2	0.87	0.18	0.4	0.8
2040 DEC	0.65	127.5	0.72	0.25	0.33	3.9

According to the data in Table 2-3, in the underground area it can be observed that a 37% increase in the installed PV power from the 2020 to the 2040DEC scenario results in an increase in *RFR* and *RDR* of 33% and 26%, respectively, indicating an increase in the self-healing capacity of the microgrid due to more availability of local generation from RESs in islanded mode. For the same reason the Loss of Load Expectation (*LOLE*) and the Energy not Supplied *(ENS*) indices decrease considerably in off-grid mode.

Figure 2-5 and Figure 2-6 show the average available PV power output, the critical load, and the average ESS energy for each month for the operation of the underground microgrid in islanded mode. A significant note here is the sharp drop in ESSs available energy in the summer months. As the load increases in the three summer months, and in all scenarios the PV power is less than the critical load in both on- and off-grid modes (Figure 2-5), the OPF algorithm optimally determines the contribution of the ESS to supply the critical load. In fact, equation (6) implies that it is necessary to have a greater contribution from the ESS (Figure 2-6) in the energy balance in order to purchase less energy from the main grid, resulting in lower operating costs. This situation is more evident in scenarios with low PV capacity and where the PV systems may not provide enough energy to charge the ESS in grid-on mode. On the other hand, the OPF causes the ESS to be fully discharged in daily operation. Therefore, during a failure (islanded mode), the average amount of energy of the ESS is not significant in July, August, and September for 2020 and in August for 2030 BC.

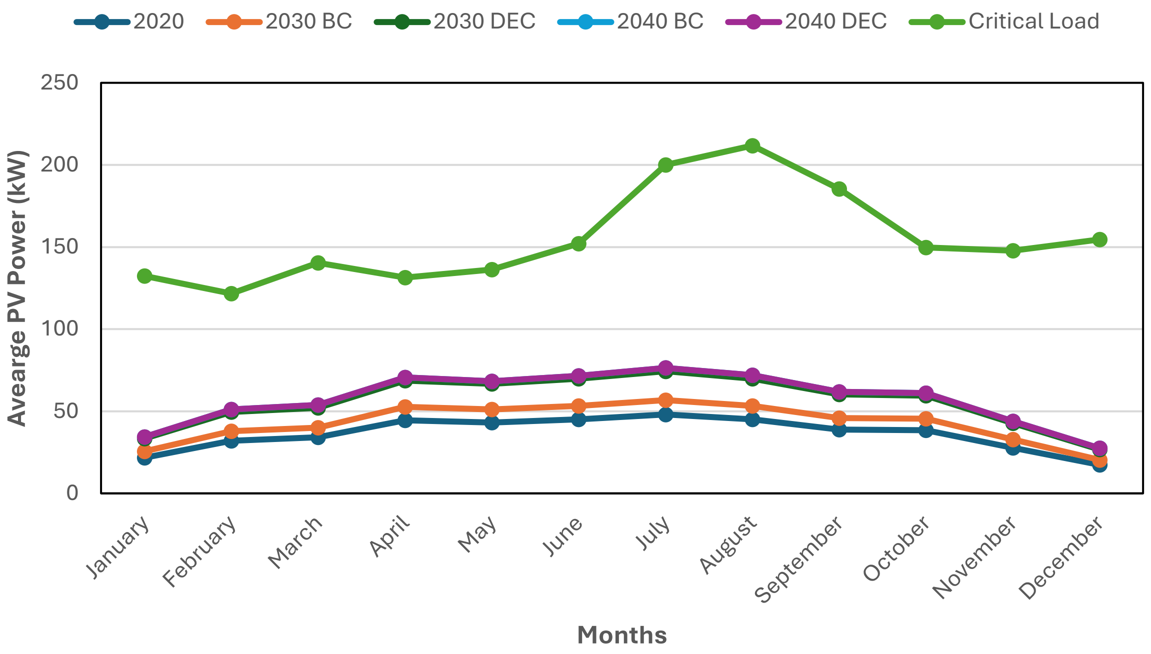

Figure 2-5. Average available PV generation and critical load in islanded mode in the underground station microgrid.

Looking at Figure 2-7, it can be seen that in the car park microgrid the average PV energy production available for the 2020, 2030 BC and 2030 DEC scenarios is just below the average critical load, while in both 2040 scenarios PV energy production far exceeds this load. Therefore, it is obvious that the increase in PV power leads to an increase in the island resilience of this microgrid, which results in an increase in the RFR, RDR, LOLE and ENS indices, so that, in the 2040 DEC scenario, we are faced with a highly resilient microgrid in which the RFR index takes on a value of 92%, as is shown in Table 2-4. Ultimately, since there is a significant difference between the available PV generation and the critical load in the last scenarios, this system can charge the ESSs and V2G EVs. Figure 2-8 and Figure 2-9 show the average available energy in isolated mode for all seasons.

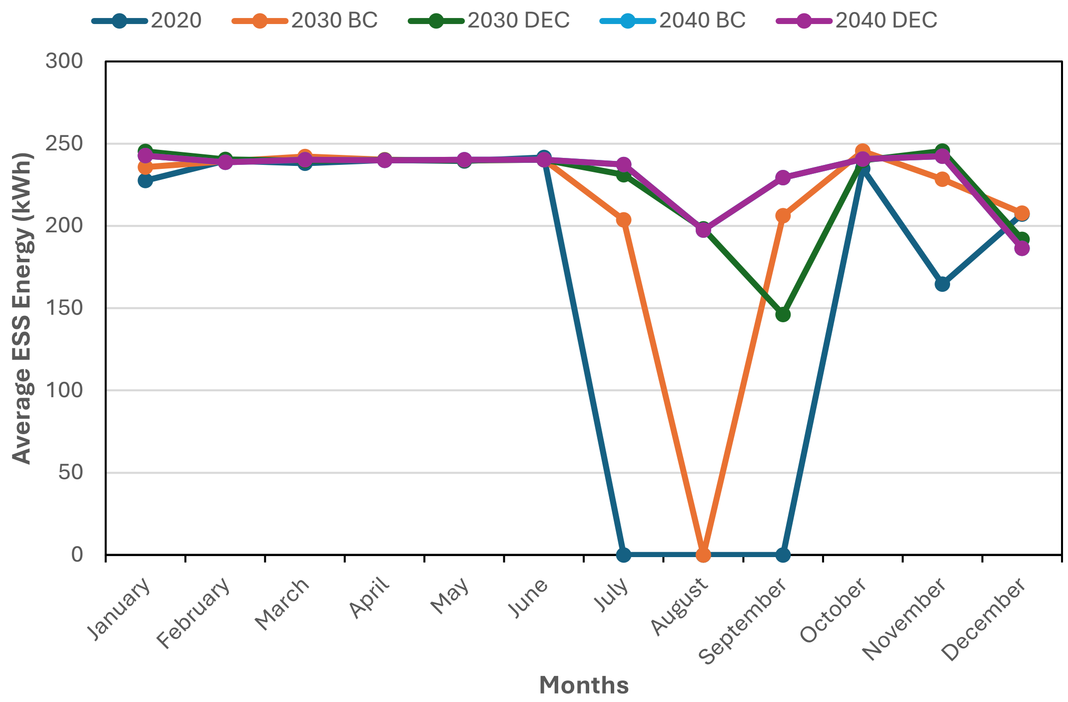

Figure 2-6. Average available energy from ESS in islanded mode in the underground station microgrid.

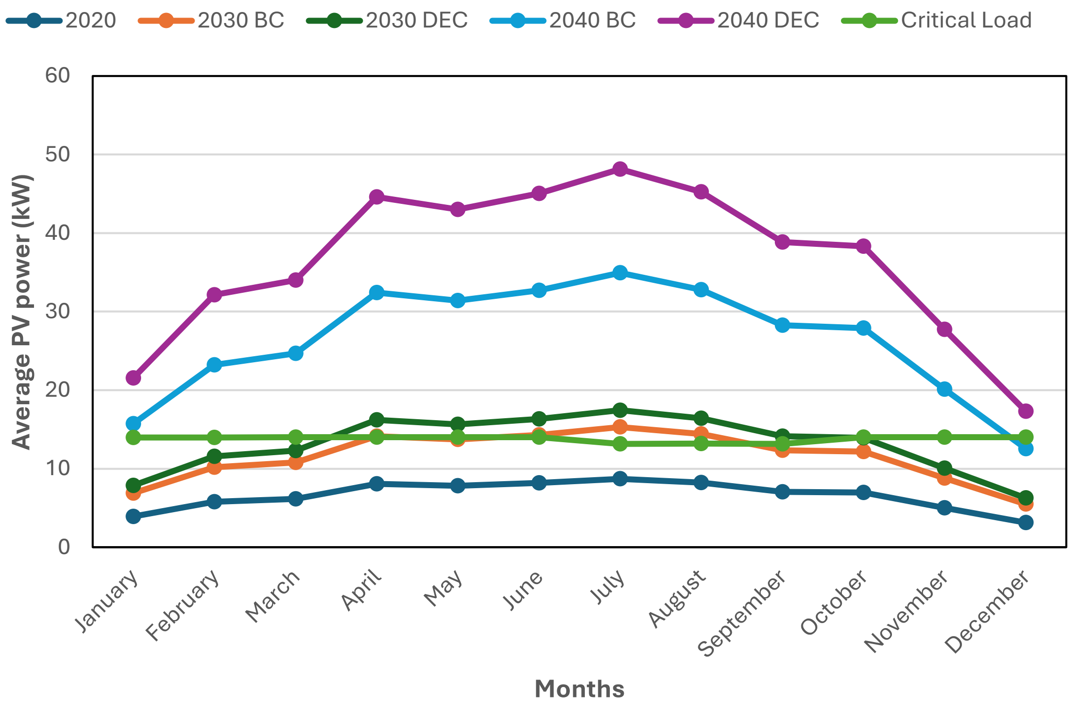

Figure 2-7. Average available PV generation and critical load in islanded mode in the car park microgrid.

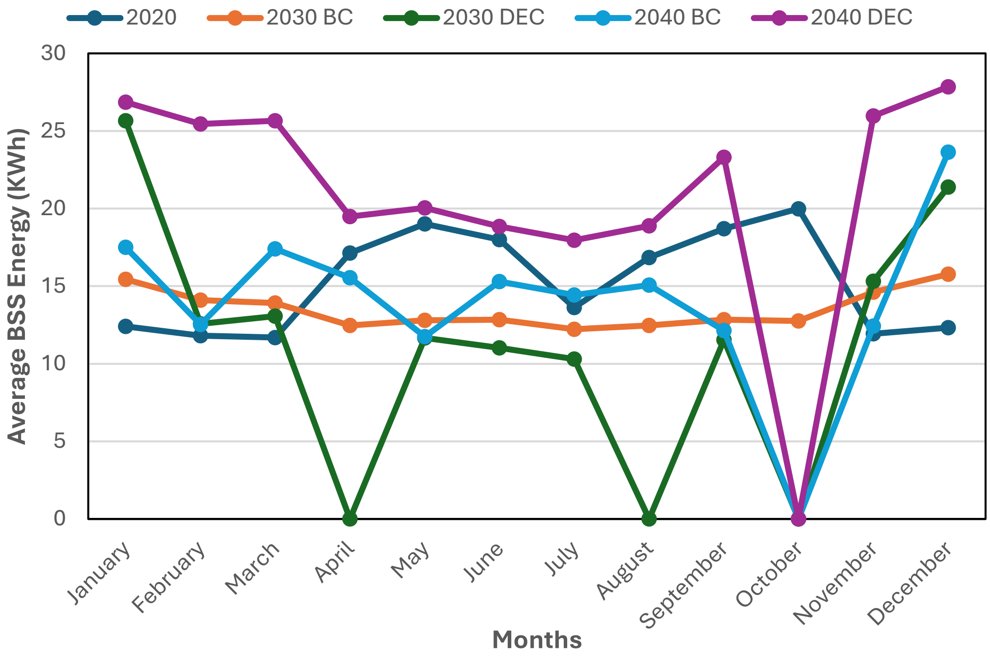

Figure 2-8. Average available ESS energy in islanded mode in the car park microgrid.

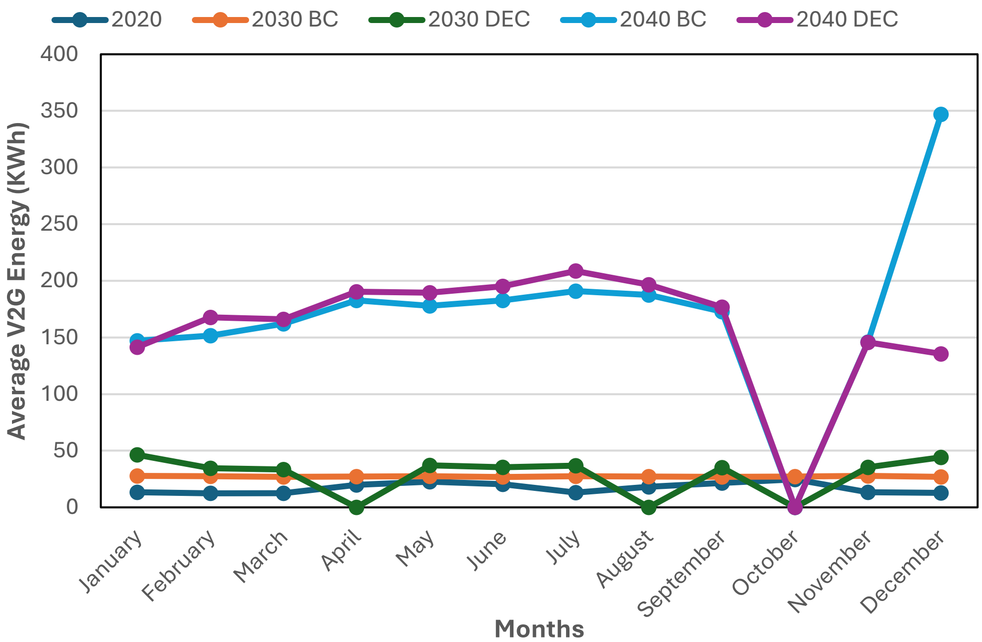

Figure 2-9. Average energy available of V2G in island mode in car park microgrid.

These figures imply that, in first two scenarios with lower PV capacity, flexible resources do not contribute in daily OPF, because it is not optimal to charge these resources frequently during a day. Consequently, their average available energy in islanded mode is quite high. Whereas, in the 2030 DEC, 2040 BC, and 2040 DEC scenarios, the figures show a greater fluctuation in the available energy of flexible resources in isolated mode. In the 2030 DEC scenario, the OPF algorithm uses a lot of this energy to minimize operating costs, so that in the three months of April, August, and October there is no energy available in island operation. Thus, this case is the worst from the resilience point of view (Table 2-4). For both 2040 scenarios, higher values of the available energy and thus of the SoC of the flexible resource batteries can be seen, as the sizes of the PV generators are significantly higher. Although these plants cannot provide enough energy in October, overall, the scenarios show higher energy availability in island operation than in other scenarios, especially in December. These fluctuations in last three scenarios determinates a drop in the flexible contribution (*FER*), as shown in Table 2-4.

Considering Table 2-5, it is worth mentioning that from the 2020 to 2040 DEC scenario, even if the size of PV and wind installations increases, the resilience of the residential microgrid worsens, as indicated by the decrease in the RFR and RDR indices, and the increase in LOLE and ENS indices. Indeed, by increasing consumption and RES capacity by 20 and 62% respectively, the RFR index decreases by 31%. Therefore, the microgrid in islanded mode might be more resilient in the former scenarios than in the latter. Observing Figure 2-10, it can be seen that there is a significant difference between the average power output of RES and the critical load in off-grid mode, the consumption decreases in spring, summer, and autumn, while the generation of PV and wind systems increases. Therefore, the average ESS energy in different months extracted from the OPF execution could influence the resilience of the microgrid.

Figure 2-11 represents this situation. The energy available in the ESS during the islanded operation for the most resilient energy scenarios (2020 and 2030 DEC) has a straight line in a year, while for other scenarios, especially those with more power from renewables, the average energy of ESS is reduced in some months of the year because the optimization of the daily operation causes storage systems to share their energy to reduce the energy purchased from the main grid. Therefore, in these scenarios, the contribution of ESSs in islanded operation decreases (RES factor) and due to the large difference between the critical load and the generation from RES, a large increase in non-supplied energy is expected. Consequently, in the residential area, increased power flow from renewable sources, which is one of the most significant self-healing techniques, does not necessarily lead to increased resilience, given the role that OPF plays in the management of the ESSs.

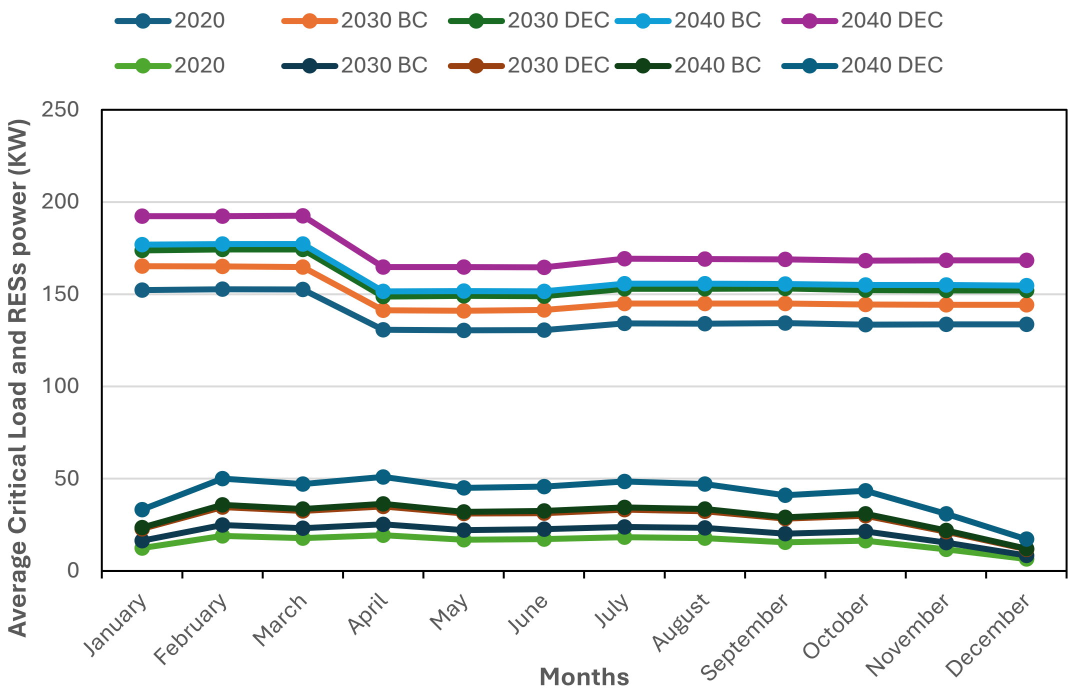

Figure 2-10. Average available RESs generation and critical load in islanded mode in Residential area.

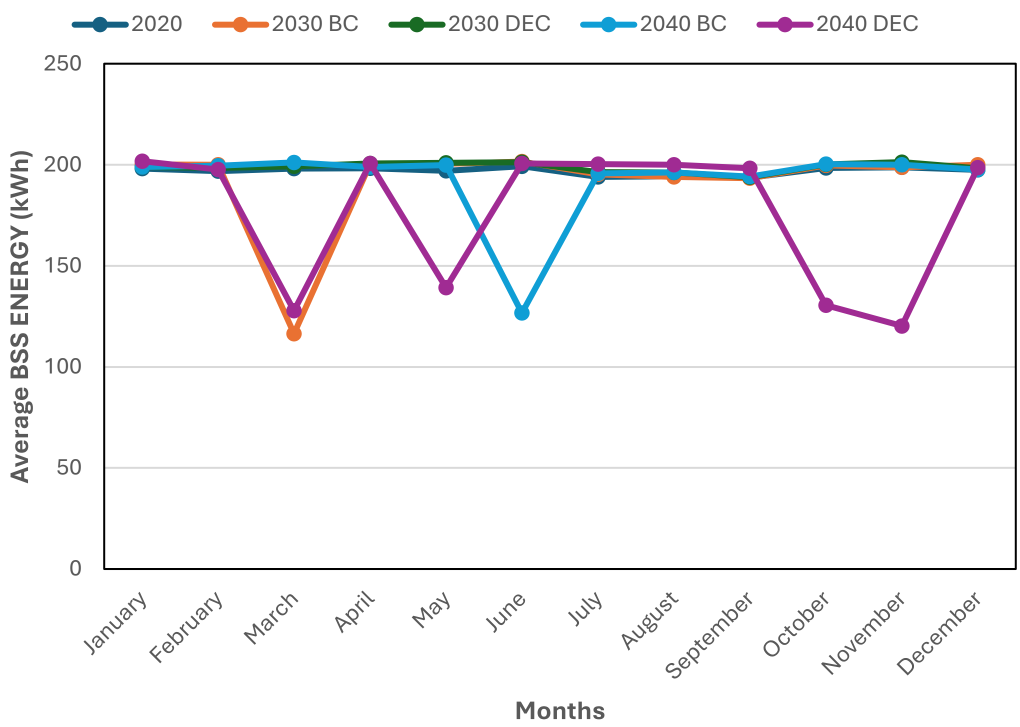

Figure 2-11. Average BSS energy available in island mode in Residential area.

2.4 Key findings and conclusion

In this chapter, a stochastic simulation-based approach has been proposed to evaluate self-healing capacity in hybrid AC/DC microgrids with flexible distributed resources in various energy scenarios. Microgrids operates in islanded mode when a fault occurs in the main AC grid and the goal of the simulations is to determine how likely these microgrids are able to supply their critical loads during island operation, using some self-healing measures such as the implementation of renewable resources, load shedding, and flexible resources (EVs and ESS systems). The performed analysis on three test microgrids shows how the consumption of critical loads in island mode, the installed capacity of RESs, the type of flexible resources, and a suitable OPF may affect self-healing factors. In the underground area, that is the simplest microgrid considered in our study, an increase in PV capacity leads to an increase in resilience; so here it would be said that capacity of RES plays the most significant role. However, in the car park zone, although in the future scenarios there is a higher RESs capacity, OPF sometimes have an adverse impact on self-healing capacity because before the island operation the optimization algorithm decides to discharge V2G smart vehicles and ESS. Residential area shows a completely different behavior comparing to the underground one due to the much more consumption than RESs capacity. In this area, in the scenarios with more RESs capacity, OPF plays a significant role to change the SoC of flexible resources leading to a decrease in these sources in island mode and resilience rates consecutively. Therefore; this chapter showed clearly how different parameters and operation control modes might change resilience factors in island mode. For future works, the author is interested in attacking different control strategies in power sharing among resources and demand response techniques. In addition, it would be worth to consider other AC/DC components like converters in self-healing capability since they can operate or blocked depending on technical parameters like voltage and frequency.

Appendix 1

Nomenclature

Sets

e	Set of energy scenarios
m	Set of microgrids
t	Set of time intervals a day
s	Set of simulation samples
l	Set of loads
i	Set of island modes
q	Set of time intervals that V2G vehicles are out

Parameters

σ/μ	Normal distribution parameters
β/α	Weibull distribution parameters
$w_i/w_o/\ w_r$	Cut-in, cut-out and rated wind speed
P_w^r	Rated power of wind turbines
c_g	Electricity price of the power purchased from the main grid
P_{v1}^{ch}	Power consumption by V1G vehicles
η	Efficiency of generation for RESs
P_{pv}^{max}/P_w^{max}	Upper limit for RESs generation
$P_{ch,s}^{max}/P_{ch,s}^{min}$	Upper and lower limits for storage system charge
$P_{dis,s}^{max}/P_{dis,s}^{min}$	Upper and lower limits for storage system discharge
$P_{ch,v2}^{max}/P_{ch,v2}^{min}$	Upper and lower limits for V2G vehicles charge
$P_{dis,v2}^{max}/P_{dis,v2}^{min}$	Upper and lower limits for V2G vehicles discharge
$U_s(0)/U_{v2}(0)$	Initial available energy at ESS and EV park

$\Delta U_s/\Delta U_v$	Small off-set energy to avoid end-of-horizon effect at BES and EV's parking
E_s^{max}/E_s^{min}	Upper and lower limit for energy at ESS
$E_{v2}^{max}/E_{v2}^{min}$	Upper and lower limit for energy at EV park
T_l	Time at which V2G vehicles leave the park
N	Number of V2G vehicles at car park
λ	Discharge rate of EVs
D	Average distance of movement each EV traverses a day
T_r	Number of time intervals microgrid is resilient
T_f	Number of time intervals during a fault (island mode)
P_l^c	Critical load consumption in each microgrids

Variables

$N(.)$	Normal distribution function
$W(.)$	Weibull distribution function
w	Wind speed
P_{pv}/P_w	Power generation of PV and wind system
C_{op}	Total operation cost
P_g	Power purchased from the main grid
P_s^{ch}/P_s^{dis}	Charge and discharge power of ESS
P_{v2}^{ch}/P_{v2}^{dis}	Charge and discharge power of V2G
I_s^{ch}/I_s^{dis}	Binary variable shows charge and discharge status of ESS
I_{v2}^{ch}/I_{v2}^{dis}	Binary variable shows charge and discharge status of V2G vehicles

E_s/E_{v2}	Available energy at ESS and V2G park
P_l	Load of microgrids before fault event
P_{RES}^i	Available power of RESs in island mode
P_F^i	Available power of flexible sources in island mode

Chapter 3 Planning and optimizing energy management in small-scale AC/DC microgrids

Abstract

This chapter proposes a planning framework for small scale power grids called energy nano-grids (ENGs) including buildings with renewable energy sources. This planning program aims to provide an energy management system in tertiary control level, where the following four problems are characterized and solved through an optimization program: A) determining the optimal energy resources mix, meaning local RESs could be PV system or/and wind turbine, their size, and installed capacity that is needed for BES; B) determining the economically optimal type of the main feeder for nanogrid (AC or DC), where RESs and flexible sources like BES and EV park lot are connected to the nanogrid; C) to conduct different scenarios correlating different range of the maximum BES's installed capacity, maximum discharge power rate in park lot, and rate of DC load to identify corresponding threshold values making a nanogrid more economically viable solution than the AC one; and D) executing properly and optimally a 24-hour load sharing among RESs, upstream network, flexible sources, and other nanogrids.

To handle and achieve abovementioned issues, the proposed nanogrid planning framework minimizes the total cost, which includes the investment costs of the energy resources and converters, the costs/revenues of energy imported/exported from/to the upstream grid or neighbouring nanogrids, and the operating costs of the nanogrids. In short, the main contributions of this chapter can be recapitulated as follows:

- Optimal planning and size of the renewable energy resources and energy storage devices;
- Determination of the economically optimal types of the main feeder in nanogrid (AC or DC);
- Determination of the optimal threshold ratios for maximum installation capacity of BESS, maximum discharge power rate of electric vehicles and DC loads rate, by conduction different scenarios, that make a DC nanogrid more affordable option than an AC one;

- Preparing a techno-economic energy management framework.

3.1 Planning formulation

3.1.1 Mathematical model

Figure 3-1 and Figure 3-2 show a precise architecture of DC and AC energy nanogrids respectively. At both types of ENGs, each ENG is connected to the upstream network through an AC common bus. In the DC ENG, a bidirectional DC/AC converter is required to connect the AC common bus (the point of common coupling) to the DC bus. The EVs' park lot, the BES and the solar systems are connected to the DC bus through DC/DC converters. In addition, wind turbine and AC loads at the ENG are connected to the DC bus using rectifiers and inverters respectively.

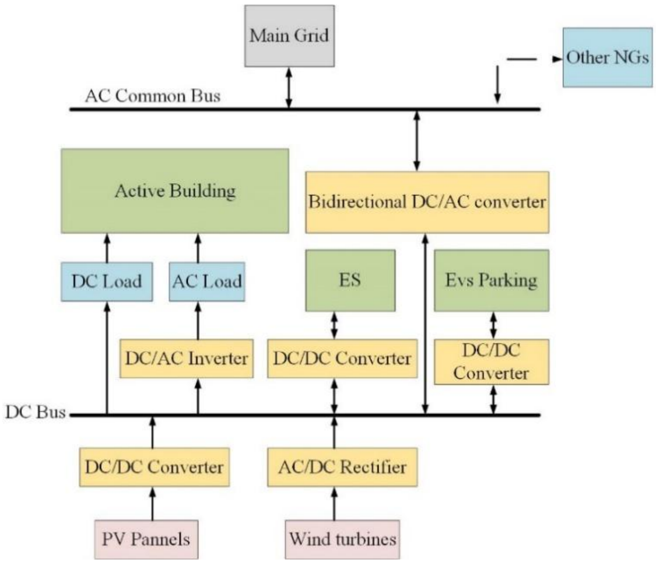

Figure 3-1. Architecture of a DC nanogrid.

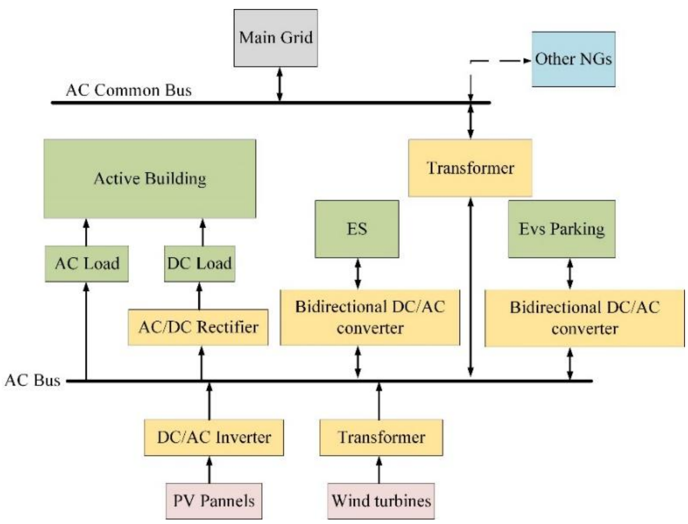

Figure 3-2. Architecture of an AC nanogrid.

In the AC ENG, the AC common bus and the wind turbine are connected to the internal AC bus by transformers. EVs' park lots and BESs are connected to the AC bus through bidirectional DC/AC converters. Inverters are needed between solar systems and the AC bus, and rectifiers to connect DC loads.

In the proposed planning model, the total cost of ENGs, including investment (IC), operation (OC) and maintenance (MC) costs, must be minimized to achieve an optimal type of ENG, and size and generation mix. Therefore, the objective function of the proposed model is as follows:

$$C_{total} = \sum_{n=1}^{NE} IC(n) + OC(n) + MC(n) \tag{3-1}$$

In this chapter, the maintenance cost is only restricted to the maintenance of DERs and not include the maintenance cost of converters since it has been supposed that all converters are not repairable and they have to be replaced with new ones after their lifetime, which is the same as the planning period horizon. Investment cost includes the capital price of all DERs and converters, and can be written as two equations below based on ENG's type DC or AC.

$$\begin{gathered} -B\big(1-\mathrm{A(n)}\big) \leq IC(n) - \Big[\sum_{y=1}^{NY} k(y) \sum_{i=1}^{NI} CR(i)P(n,i) + \sum_{y=1}^{NY} k(y)E(n)CS + \\ \sum_{y=1}^{NY} k(y)P(n,1)CRE + \sum_{y=1}^{NY} k(y)P(n,2)CC + \sum_{y=1}^{NY} k(y)\big(1- \\ l(n)\big)\, L^{max}(n)CI + \sum_{y=1}^{NY} k(y)P_{ch}^{max}CC + \sum_{y=1}^{NY} k(y)P_{ch,ev}^{max}CC + \\ \sum_{y=1}^{NY} k(y)P_{g}^{max}CB\Big] \leq B\big(1-\mathrm{A(n)}\big) \qquad \forall n \end{gathered} \tag{3-2}$$

$$\begin{gathered} -BA(n) \leq IC(n) - \Big[\sum_{y=1}^{NY} k(y) \sum_{y=1}^{NY} \sum_{i=1}^{NI} CR(i)P(n,i) + \sum_{y=1}^{NY} k(y)E(n)CS + \\ \sum_{y=1}^{NY} k(y)P(n,1)CT + \sum_{y=1}^{NY} k(y)P(n,2)CI + \sum_{y=1}^{NY} k(y)l(n)\, L^{max}(n)CRE + \\ \sum_{y=1}^{NY} k(y)P_{ch}^{max}CB + \sum_{y=1}^{NY} k(y)P_{ch,ev}^{max}CB + \sum_{y=1}^{NY} k(y)P_{g}^{max}CT\Big] \leq BA(n) \qquad \forall n \end{gathered} \tag{3-3}$$

According to Equation (3-2), if planning prefers the DC ENG, variable A sets to 1 and equation (3-3) would be free; thus, the investment cost is equal to (3-2). Conversely, if planning chooses the AC ENG, variable A is 0 and equation (3-2) would be free; in this case, the investment cost would be equal to equation (3-3). It is worth mentioning that the DERs set (i) includes both wind and photovoltaic power systems: i=1 indicates wind and i=2 indicates solar. Equations (3-4) and (3-5) below represent the operation and maintenance costs, which are the cost of purchasing and selling energy from/to the upstream network, and of the DERs' repair and refurbishment, respectively, and Equation (3-6) refers to the coefficient of the net present value.

$$OC(n) = \sum_{y=1}^{NY} k(y) \sum_{d=1}^{ND} \sum_{t=1}^{NT} C^p P_g(n,t) - \sum_{y=1}^{NY} k(y) \sum_{d=1}^{ND} \sum_{t=1}^{NT} C^s P_c(n,t) \qquad \forall n \tag{3-4}$$

$$MC(n) = \sum_{y=1}^{NY} k(y) M^w P(n,1) + \sum_{y=1}^{NY} k(y) M^p P(n,2) \qquad \forall n \tag{3-5}$$

$$k(y) = \frac{1}{(1+r)^{y-1}} \qquad \forall y \tag{3-6}$$

Other constraints can be divided into three categories: limits and constraints for the power balance equation and DER generation, constraints for energy trading between ENGs and the upstream grid, and constraints for BESs and EV's park lots.

3.1.2 Power balance and generation

Equations and inequalities (3-7) to (3-12) represent generation-related constraints. Equations (3-7) and (3-8) show the hourly power balance for both DC and AC ENGs during a day. Like for the investment cost equations, if planning prefers the DC ENG, variable A is 1, and (3-8) would be free; so, the power balance equation would match (3-7). Conversely, if planning chooses the AC ENG, variable A is equal to 0, and equation (3-7) gets free. As a result, the power balance formulation would be equal to equation (3-8).

$$-B\big(1 - \mathrm{A(n)}\big) \le Q\big[P_p(n,t) + P_w(n,t) + P_g(n,t) + P_s^{dis}(n,t) + P_{ev}^{dis}(n,t)\big] - Q[P_s^{ch}(n,t) + P_{ev}^{ch}(n,t)] - l(n)L(n,t) - \frac{(1-l(n)L(n,t)}{Q} - \frac{P_c(n,t)}{Q} \le B\big(1 - \mathrm{A(n)}\big) \qquad \forall n,t \tag{3-7}$$

$$-BA(n) \le Q\big[P_p(n,t) + P_s^{dis}(n,t) + P_{ev}^{dis}(n,t)\big] + P_w(n,t) + P_g(n,t) - Q[P_s^{ch}(n,t) + P_{ev}^{ch}(n,t)] - (1 - l(n))L(n,t) - \frac{l(n)L(n,t)}{Q} - P_c(n,t) \le BA(n) \qquad \forall n,t \tag{3-8}$$

Inequality (3-9) states that DERs in each ENG must be able to supply, at any time, at least a predefined critical load (α is the percentage of critical load on the maximum load).

Equations (3-10) and (3-11) represent the output power limit for DERs, where β is the efficiency of generation for DERs and γ is a coefficient less and equal than 1 giving sunlight intensity during the day (0 in the absence of sun and 1 at noon). Equation (3-12) expresses the upper and lower limits for the installed capacity of DERs, and equation (3-13) shows that it is obligatory for an ENG to have at least one kind of DERs in the problem formulation.

$$\sum_{i=1}^{NI} P(n,i) \geq \alpha . L^{max}(n) \qquad \forall n \tag{3-9}$$

$$P_w(n,t) \leq \beta P(n,1) \qquad \forall n,t \tag{3-10}$$

$$P_p(n,t) \leq \beta \gamma(t) P(n,2) \qquad \forall n,t \tag{3-11}$$

$$I_R(n,i) P^{min}(n,i) \leq P(n,i) \leq I_R(n,i) P^{max}(n,i) \qquad \forall n,i \tag{3-12}$$

$$\sum_{i=1}^{NI} I_R(n,i) \geq 1 \qquad \forall n \tag{3-13}$$

Since this chapter implements an energy management system in tertiary level (optimal load sharing), lower control levels (secondary and primary) are not discussed, assuming they are done well through converters' controller. The note is that the capacity (size) of DERs, that are going to be installed, is a variable calculated in the planning process. Then, these power set points are delivered to local controller of the converters. To PV system, this chapter conducts a Constant Power Generation (CPG) control scheme presented in [117, 118], where the PV output voltage is continuously perturbed away from the maximum power point in the CPG operation mode in order to match the PV output power according to the set point. Therefore, equation (3-11) is characterized to represent this concept. In this equation, parameter γ indicates maximum generation of PV system in per unit (p.u.) (in association with irradiance and temperature) that is multiplied to the size of the PV to calculate the maximum output power for each hour. To wind system, a blade pitch control is considered to generate constant power. Readers may refer to [119] to understand more blade pitch control. For both PV and wind systems, if the program chooses maximum power, controllers follow Maximum Power Point Tracking (MPPT) mode; and, inversely, for power references below than maximum value, they conduct constant power generation mode.

3.1.3 Energy Trading Constraints

Inequalities (3-14) and (3-15) restrict power trading between ENG and upstream network to their bounds, and (3-16) represents that to sell and purchase energy to/from the grid may not be happened simultaneously.

$$I_g(n,t)P_g^{min} \leq P_g(n,t) \leq I_g(n,t)P_g^{max} \qquad \forall n,t \tag{3-14}$$

$$I_c(n,t)P_s^{min} \leq P_c(n,t) \leq I_c(n,t)P_s^{max} \qquad \forall n,t \tag{3-15}$$

$$I_g(n,t) + I_c(n,t) \leq 1 \qquad \forall n,t \tag{3-16}$$

3.1.4 BES and EV constraints

Constraints (3-17) to (3-26) express BES's limits. Inequalities (3-17) to (3-19) represent that installed capacity, charging/discharging power rates of the BES must not exceed their technical bounds, while (3-20) implies that batteries must not be charged and discharged at the same time.

$$E_s^{min} \leq E(n) \leq E_s^{max} \qquad \forall n \tag{3-17}$$

$$I_s^{ch}(n,t)P_{ch}^{min} \leq P_s^{ch}(n,t) \leq I_s^{ch}(n,t)P_{ch}^{max} \qquad \forall n,t \tag{3-18}$$

$$I_s^{dis}(n,t)P_{dis}^{min} \leq P_s^{dis}(n,t) \leq I_s^{dis}(n,t)P_{dis}^{max} \qquad \forall n,t \tag{3-19}$$

$$I_s^{ch}(n,t) + I_s^{dis}(n,t) \leq 1 \qquad \forall n,t \tag{3-20}$$

Equations (3-21) and (3-22) show the hourly available energy at the storage system, while (3-23) to (3-25) restrict this energy to its upper and lower limits. Inequality (3-26) tries to prevent the energy of the last hour at BES from not being much more or lower than that of the first hour.

$$e_s(n,t) = e_s(n,t-1) + P_s^{ch}(n,t).Q - \frac{P_s^{dis}(n,t)}{Q} \qquad \forall n,t > 1 \tag{3-21}$$

$$e_s(n,t) = U_s(0) + P_s^{ch}(n,t).Q - \frac{P_s^{dis}(n,t)}{Q} \qquad \forall n,t < 2 \tag{3-22}$$

$$e_s^{min}(n) \leq e_s(n,t) \leq e_s^{max}(n) \qquad \forall n,t \tag{3-23}$$

$$e_s^{min}(n) = z.E(n) \qquad \forall n \tag{3-24}$$

$$e_s^{max}(n) = Z.E(n) \qquad \forall n \tag{3-25}$$

$$U_s(0) - \Delta U_s \leq e_s(n,t) \leq U_s(0) + \Delta U_s \qquad \forall n, t > 23 \tag{3-26}$$

The rest of the inequalities refer to EVs in which equations (3-27) to

(3-33) have approximately the same definition as those for BES because EVs can be operated like battery storage system. Equations (3-34) and (3-35) point that when EVs are out of the ENG's park lot, they cannot be charged or discharged. Finally, equation (3-36) explains that EVs have to be charged with a minimum energy level needed for daily journey.

$$I_{ev}^{ch}(n,t)P_{ch,ev}^{min} \leq P_{ev}^{ch}(n,t) \leq I_{ev}^{ch}(n,t)P_{ch,ev}^{max} \qquad \forall n, t \in T_{in} \tag{3-27}$$

$$I_{ev}^{dis}(n,t)P_{dis,ev}^{min} \leq P_{ev}^{dis}(n,t) \leq I_{ev}^{dis}(n,t)P_{dis,ev}^{max} \qquad \forall n, t \in T_{in} \tag{3-28}$$

$$I_{ev}^{ch}(n,t) + I_{ev}^{dis}(n,t) \leq 1 \qquad \forall n, t \tag{3-29}$$

$$e_{ev}(n,t) = e_{ev}(n,t-1) + P_{ev}^{ch}(n,t).Q - \frac{P_{ev}^{dis}(n,t)}{Q} - P_{ev,out}^{dis}(n,t) \qquad \forall n, t > 1 \tag{3-30}$$

$$e_{ev}(n,t) = U_{ev}(0) + P_{ev}^{ch}(n,t).Q - \frac{P_{ev}^{dis}(n,t)}{Q} - P_{ev,out}^{dis}(n,t) \qquad \forall n, t < 2 \tag{3-31}$$

$$U_{ev}^{min}(n) \leq e_{ev}(n,t) \leq U_{ev}^{max}(n) \qquad \forall n, t \tag{3-32}$$

$$U_{ev}(0) - \Delta U_{ev} \leq e_{ev}(n,t) \leq U_{ev}(0) + \Delta U_{ev} \qquad \forall n, t > 23 \tag{3-33}$$

$$P_{ev}^{ch}(n,t) = 0 \qquad \forall n, t \in T_{out} \tag{3-34}$$

$$P_{ev}^{dis}(n,t) = 0 \qquad \forall n, t \in T_{out} \tag{3-35}$$

$$e_{ev}(n,T_l) \geq N.\lambda.D \qquad \forall n \tag{3-36}$$

In this chapter a mixed-integer linear programming (MILP) formulation is considered to solve the optimal planning for residential energy nanogrids including DERs' and BES's mix and size, determining the type of ENGs (DC or AC) and the 24-hourly optimal load sharing under different situations and scenarios. The program is solve using Cplex solver in GAMS tool.

3.2 Case study

To illustrate the performance and benefits of the proposed planning model, three residential buildings are considered as three ENGs which are connected to the upstream network through an AC bus (see Figure 3-1 or Figure 3-2). Each ENG is a residential tower with a park lot for hybrid electric vehicles which is able to charge and discharge vehicles' battery. In addition, there are 100 units at each ENG, and it is assumed that all units have an EV. The ENGs are supposedly located in Australia and the load data has been extracted from 300 residential customers there [120]. Figure 3-3 displays the hourly load demand of the three residential ENGs under study.

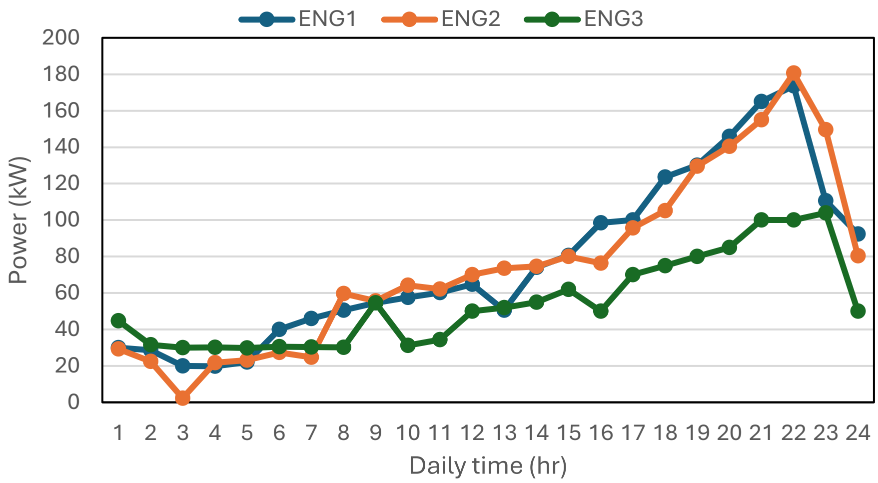

Figure 3-3. Hourly power demand of the three residential ENGs.

Mitsubishi SUV (6 charge hour, 240 V, 10 A, 54 Km, 12 kWh) as one of the popular Plug-in Hybrid Electrical Vehicles (PHEVs) is selected for this study [121]. Data related to the average daily journey in Australia is found in [122]. Planning horizon, discount rate, coefficient of upper and lower energy limit for BES, and the time at which EVs leave the ENGs are 10 years, 0.1, 0.1, 0.9, and 6:00 AM, respectively. EVs are supposed to go back park lot at 8:00 PM, so their batteries might be charged and discharged before 6 AM. Investment and maintenance cost of DERs and BESs, and investment cost of converters have been drawn from [123], [124], [125], and [126]. The cost-related characteristics of DERs and converters are provided in Table 3-1.

Table 3-1. Characteristics of converters and DERs

Converters, BES, and DERs	Investment cost ($/kW(h))	Maintenance cost ($/kW)
Inverter	58	-
Rectifier	40	-
DC/DC converter	65	-
Bidirectional DC/AC	80	-
Transformer	30	-
BES	100	-
Wind turbine	2800	30
PV system	2000	20

As it was said before, the main goal of this chapter is to evaluate how some parameters may change the type of ENG, the mix of generation, and the optimal planning and operation of ENGs. In this study, these parameters are the rate of DC load at the ENGs, changes in the maximum permissible capacity of BES, and the maximum discharge power rate of EVs. Therefore, as follows, four cases are projected to assess these aims.

Note that, the initial available energy (state of charge) inside BES at the first hour before starting the programming depends on the scenarios are defined in the following subsections, but in general, for BES system, it is about 80% of the capacity. For example, in a case that battery capacity is fixed (800 kWh), initial energy value is 650 kWh. For electrical vehicles' battery, however, this rate is 50% of the corresponding capacity.

3.2.1 Case Base

This is the first case of programming. In this case, the rate of DC load for all three ENGs is 0.5, the upper bound for permissible installation capacity of BES is set on the highest value (800 kWh), and the maximum discharge power rate of EVs to support demand supply is considered equal to its peak that is 200 kW. The results of the planning for this case are represented in Table 3-2.

Table 3-2. Planning results of the case base.

ENGs	A	PV installed capacity (kW)	Wind installed capacity (kW)	BES installed capacity (kWh)	Investment cost ($)	Operation cost ($)	Maintenance cost ($)
ENG 1	0	145.5	0	774	3040706.1	9364.4	23715.8
ENG 2	0	100	0	774	2910217	18792.7	22322.5
ENG 3	0	0	100	774	2185093.76	416083	13518

3.2.2 Case 1

In this case, the effect of changes in the rate of DC load at three ENGs on the type of nanogrid, DERs' mix and capacity, investment and operation costs and daily load sharing are evaluated. The parameter α increases from 0.4 to 1 by 0.2 steps. Other parameters are fixed at their base values as those in the case base. The results of the planning in case 1 are shown in Table 3-3.

Table 3-3. Planning results of case 1.

l	ENGs	A	PV installed capacity (kW)	Wind installed capacity (kW)	BES installed capacity (kWh)	Investment cost ($)	Operation cost ($)	Maintenance cost ($)
0.4	ENG 1	0	116.9	0	774	3035341.4	37745.7	23708.7
	ENG 2	0	110	0	774	2712376	26028.1	20277

	ENG 3	0	0	100	774	2182284.7	410684.1	13518
0.6	ENG 1	1	123.4	0	774	3136466.9	39280.4	25033.4
	ENG 2	1	100.8	0	774	2699869.2	128717.4	20438.8
	ENG 3	0	0	100	774	2187902.8	421481.9	13518
0.8	ENG 1	1	120	0	774	3057498.4	49184	24343
	ENG 2	1	100	0	774	2670392.7	97749.3	20277
	ENG 3	1	0	100	774	2170622.9	444151.3	13518
1	ENG 1	1	118.1	0	774	3006967.9	14731.4	23953
	ENG 2	1	100	0	774	2656232.8	86900.1	20277
	ENG 3	1	0	100	774	2162476.7	432238.7	13518

3.2.3 Case 2

This case analysis how an increase in the upper bound for allowable installation capacity of BES can change the type of ENG, the mix and capacity of generation and investment and operation costs, and the way that electrical energy flows as well. This parameter E_s^{max} rises from 200 to 800 kWh by 200 kWh steps. The rate of DC load and peak of EVs' discharge power are put on their basic amount (0.5, 200 kW). Table 3-4 shows the planning consequences of this case.

3.2.4 Case 3

This case evaluates how increase in the maximum discharge power rate of electric vehicles might change the type of ENG, the mix and size of generation units, investment, and operation costs, and the 24-hour load sharing. It is obvious that EVs may not supply ENGs demand power with their maximum discharge power rate because of being out of park lot and unexpected events. This type of flexible resources' behavior is unpredictable. So, this chapter considers changes in the availability amount of this parameter ($P_{dis,ev}^{max}$) rather than stochastic approaches where the number of cars and available energy are calculated stochastically. This parameter $P_{dis,ev}^{max}$ rises from 50 to 200 kW with 50 kW steps. The rate of DC load and upper bound for installation capacity of BES are fixed on their basic values (0.5 and 800 kWh). Table 3-5 illustrates the planning results for this case.

Table 3-4. Planning results of case 2.

E_s^{max}(KWh)	ENGs	A	PV installed capacity (kW)	Wind installed capacity (kW)	BES installed capacity (kWh)	Investment cost ($)	Operation cost ($)	Maintenance cost ($)
200	ENG 1	0	145.5	0	190.1	3191888.6	-130717.6	29502.5
	ENG 2	0	100	0	190.1	2322565.1	50415.2	20277
	ENG 3	0	0	100	190.1	1790400.1	425971.7	13518
400	ENG 1	0	101.1	0	390	2479171.3	94515.8	20514.2
	ENG 2	0	100	0	390	2457745.6	27575.6	20277
	ENG 3	0	0	100	390	1925580.6	413256.4	13518
600	ENG 1	1	123.4	0	579	3011429.7	25698	25033.4

	ENG 2	0	110	0	579	2585416	24473.2	20277
	ENG 3	0	0	100	579	2053251	409859.3	13518
800	ENG 1	0	116.9	0	774	3040706.1	9364.4	23715.8
	ENG 2	0	110	0	774	2910217	18792.7	22322.5
	ENG 3	0	0	100	774	2185093.7	416083	13518

Table 3-5. Planning results of case 3.

$P_{dis,ev}^{max}$	ENGs	A	PV installed capacity (kW)	Wind installed capacity (kW)	BES installed capacity (kWh)	Investment cost ($)	Operation cost ($)	Maintenance cost ($)
50	ENG 1	0	117.8	0	774	3058044.3	10856	23899.6
	ENG 2	0	100	0	774	2717258.7	37494.9	20277
	ENG 3	0	0	100	774	2185093.7	416083	13518
100	ENG 1	0	119.1	0	774	3083212.8	33947.2	24166.4
	ENG 2	0	100	0	774	2717258.7	30403.8	20277
	ENG 3	0	0	100	774	2185093.7	416083	13518
150	ENG 1	0	17.8	0	774	3058044.3	7099.6	23899.6
	ENG 2	0	111.2	0	774	2932775.4	-7633.9	22561.7
	ENG 3	0	0	100	774	2185093.7	416083	13518
200	ENG 1	0	116.95	0	774	3040706.1	9364.4	23715.8
	ENG 2	0	110	0	774	2910217	18792.7	22322.5
	ENG 3	0	0	100	774	2185093.7	416083	13518

3.3 Discussion

Starting from the case base, as it can be seen from Table 3-2, it is noticeable that the program would choose AC type for all three ENGs ($A = 0$) because, in this common occasion, the cost of all converters in the DC ENGs is significantly higher than that of an AC one. Customers are supplied by photovoltaic plants at the first two ENGs and by wind plants at the third ENG. Since the installed capacity of PV systems at ENG1 and ENG2 are larger than wind system at ENG3, investment and maintenance costs of ENG1 and ENG2 are higher than those at ENG3.

Looking at both Table 3-2 and Figure 3-4, simultaneously, although solar systems cannot generate energy in the absence of sun (night hours) and the peak load at these ENGs (ENG 1 and ENG 2) is higher than peak load at ENG 3, program would prefer to install photovoltaic plants for both ENG1 and ENG 2. There are two reasons: first, the investment cost of the solar system is lower than that of the wind one, and second, they can sell electrical energy to the upstream network at noon which leads to a considerable decrease in the operation cost. To reach a balance between operation and investment cost, the program would rather set lower wind power generation than peak load at ENG 3. In this case ENG's load is provided at peak hours through purchasing energy from the upstream grid. Therefore, operation cost at this nanogrid has a meaningful value.

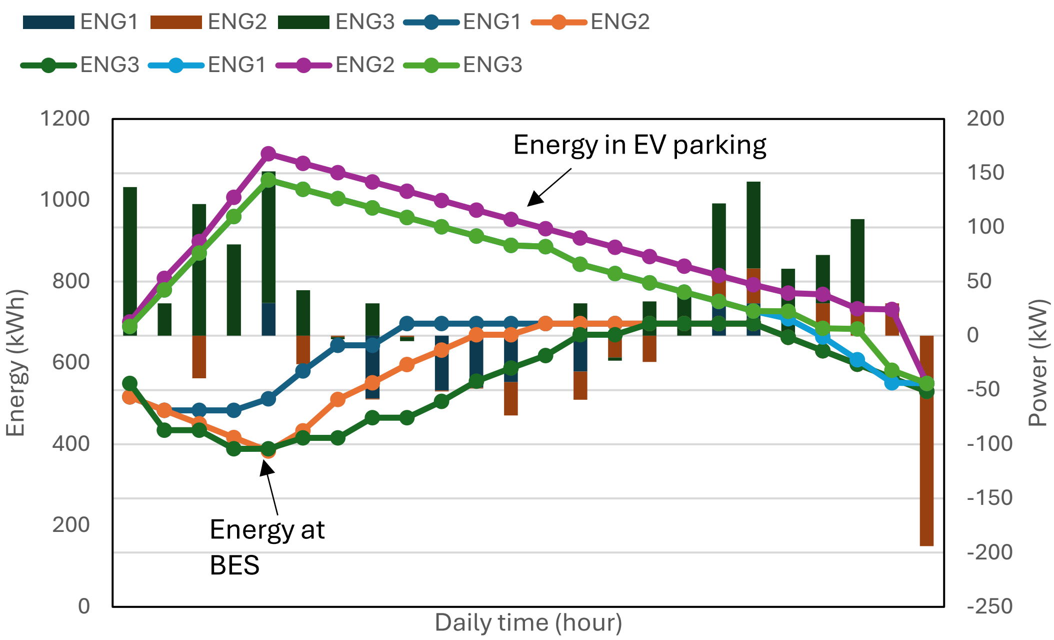

Figure 3-4. Daily energy and power trading in the case base.

Figure 3-4 shows the daily energy available at the BES system and EVs parking (line graphs) and the daily power trading (bar charts) in the case base. It is worth saying, due to this fact that all ENGs are residential buildings with similar power demand behavior, these variables at each building would change as other. It can be derived that electrical vehicles in park lot, unlike batteries at BES system, are charged at early hours of a day. This is reasonable because EVs should be prepared to go out till 20 PM. after that they can share their energy to supply load and/or trade with the main grid. Conversely, the BES system is discharged at the first hours to help supply ENGs' load demand, then it is charged to peak hours, largely by PV systems for ENG 1 and ENG 2 and by purchasing energy from the main grid for ENG 3. Finally, it has the same trend as EVs during peak hours. Figure 3-4 represents the reason why operation cost at ENG 3 is significantly more than other ones. It mostly receives electrical energy from the upstream network during a day which causes to drop in DER's investment cost.

Looking at Table 3-3, some conclusions can be drawn. First, as expected, a change in the rate of DC load affects the type of ENGs. An increase in the rate of DC load, according to investment cost equation for DC ENG (Equation (3-2)), results in a decrease in the term related to the inverter in this equation, and in the case $l(n) = 1$, where there is no AC load, it would be deleted. Conversely, according to equation (3-3), the investment cost for rectifier rises when l increases. So, investment cost in DC case would be much lower than that in AC one. Power balance equations can also make this analysis clearer. In fact, as l increases, considering converters efficiency, DC ENG needs less energy from the upstream grid and/or other sources to supply customers than AC ENG. Therefore, DC ENG would be preferable to AC one. Since the peak load at ENG1 and ENG 2 is higher than at ENG 3, less increase in l at the first two ENGs leads to a more considerable reduction in the investment cost. So, the optimal threshold ratios of l are 0.6 for ENG 1 and ENG 2 and 0.8 for ENG 3.

Moreover, due to not change in load demand and upper bound of capacities, the mix generation and installed capacity of DERs and BES have not been updated. So, investment and maintenance costs have not approximately changed, and the little fluctuations in Table 3-3 are due to an increase in l; therefore, non-meaningful changes in investment cost of rectifiers and inverters are carried out.

It is note that emerges from the examination of Table 3-3 concerns the operating cost. There is a sharp increase in the operating cost of ENG 2 with an increase of l from 0.4 to 0.6. There is an acceptable reason for this, namely that by changing the type of ENG and considering the power balance equation in the DC state (see equation (3-7)), the efficiency of the converters causes the ENG to purchase more energy from the upstream grid. Furthermore, since the sale and purchase of energy from/to the upstream grid may not occur simultaneously, the operating cost would increase (see equation (3-4)). The same assessment is valid for an increase in operation cost at ENG 1, while due to higher peak load than ENG 2, it rises when l goes up excepting when $l(n) = 1$, where AC load term in power balance equation, which is connected to converter in DC power balance equation (see equation (3-7)) would be disappeared, so there would be less needed to purchase energy. Nevertheless, its noticeable drop once l rises from 0.8 to 1 is for the term of AC load.

This point could be clearer from the bar chart Figure 3-5 showing trading energy between ENGs and the main grid. It could be said that, although the output of wind plants is not restricted by environmental parameters like irradiance for photovoltaic systems, ENG 3 would almost buy energy whole a day from the main grid; the convincing reason is expensive investment cost for this system. According to the line graph in Figure *3-5*, it is expected that a change in the DC load rate will not lead to any significant change in the energy stored by the BES and EV parking, because they are largely limited by their local parameters.

In case 2, looking at Table 3-4, the impact of increase in the upper bound of the installed capacity of BES has been assessed. It is projected that a rise in E_s^{max} may not make a considerable difference in the type of ENGs since both DC and AC investment cost equations (see equations (3-2) and (3-3)) have the term related to BES's investment cost in common. Once E_s^{max} = 600 kWh, the type of ENG 1 is DC which is caused by a change in the pattern

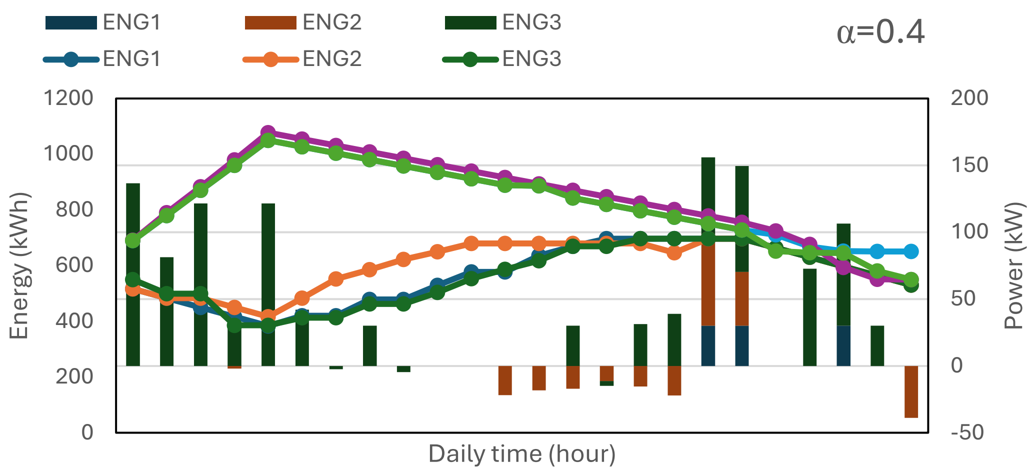

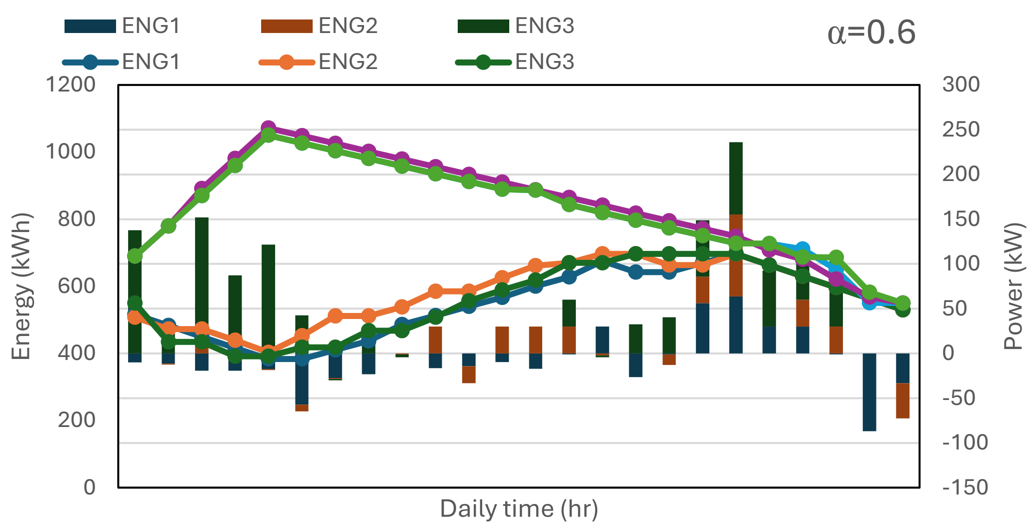

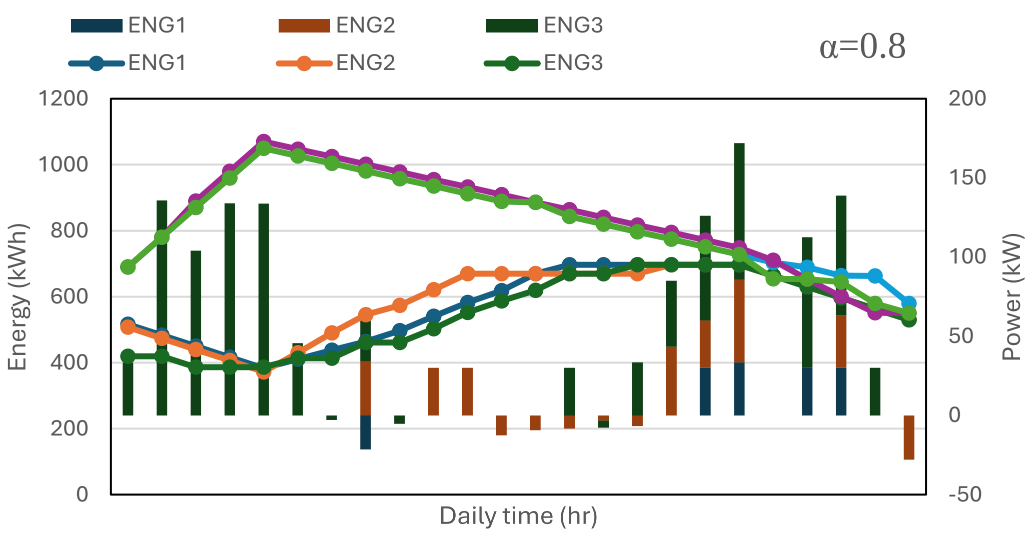

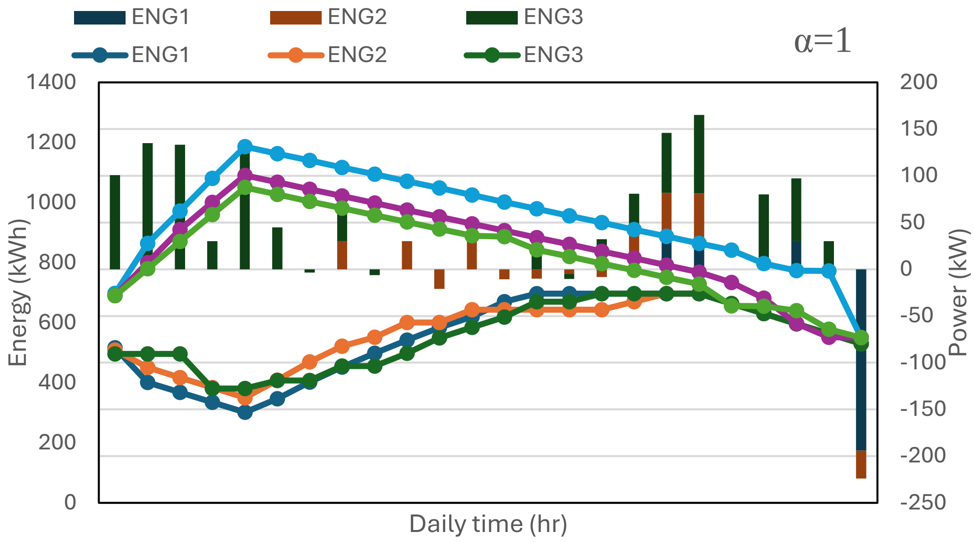

Figure 3-5. Daily energy management in case 1: energy available at BESs and EVs parking, and power trading between ENGs and upstream network.

of BES's charge and discharge so that it can decrease operation cost when DC ENG is chosen.

Another predictable point is that once $E_s^{max} = 200$ kWh, ENG1 ,where there is a higher peak load than other ones, must use a solar power system with more capacity; this leads to a surge in investment costs in this ENG. Note that the capacity of the solar system rises so much, meaning the amount of electrical energy which the ENG sells to the upstream network is more than that of ENG purchases from it; therefore, the operation cost at this ENG is negative. It can be seen that, the more amount for E_s^{max}, the more available energy for selling, and the less need to buy energy from the upstream grid. So, operation costs would decrease. While, for ENG 2 and ENG 3, a change in E_s^{max}, according to Table 3-4, might not make any sensible changes in the installation capacity of DERs. As a result, maintenance costs at these ENGs remain stable. When this parameter increases, investment cost at these two ENGs rises due to an increase in the cost of BES, whereas their operation cost dips because of more energy sold and less energy purchased.

From the line graph in Figure 3-6, it is obvious that higher E_s^{max} availability has caused more installation capacity of the BES system. Another noteworthy point is that an increase in hourly energy available at the electric vehicle park lots, due to the increase in the amount of energy at the BES, allows them to share their batteries to supply energy to the load or sell it to the main grid; therefore, the ENGs, especially ENG 3 due to its lower peak load than the others, do not need the electric vehicles to supply energy. The bar chart in Figure 3-6 advocates the evaluation above for case 2. ENG 1 with bigger installation capacity sells considerable energy to the main grid. When $E_s^{max} = 400$ kWh, it has a wild drop, making ENG 1 not trade energy with the upstream network. $E_s^{max} = 600$ kWh leads to higher capacity of the solar system, and to more balance trading. Considering both bar chart and Table 3-4, because the generation capacity at ENG 3 is low and constant, more capacity of BES system does not considerably change energy trading pattern but increases the investment cost.

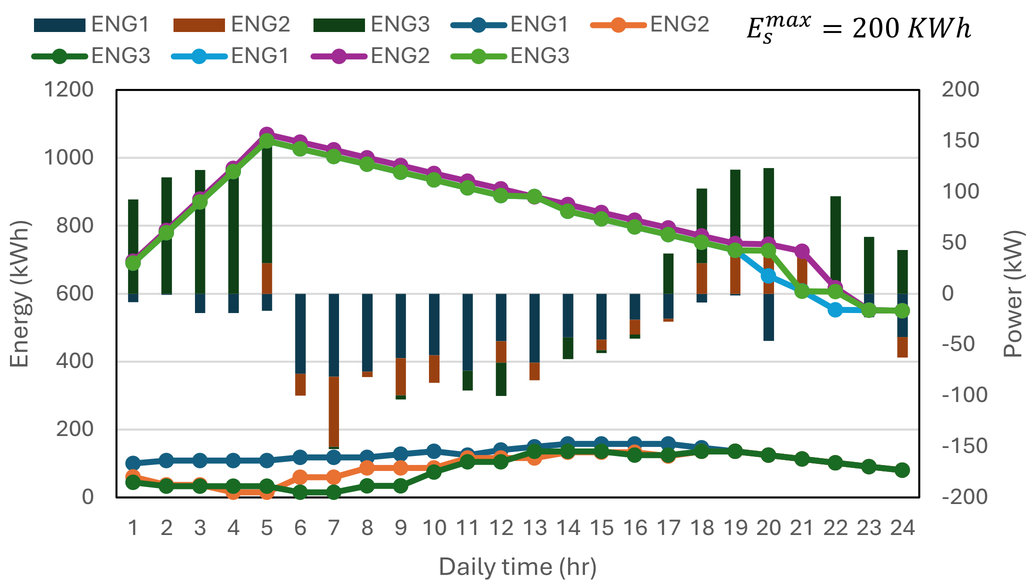

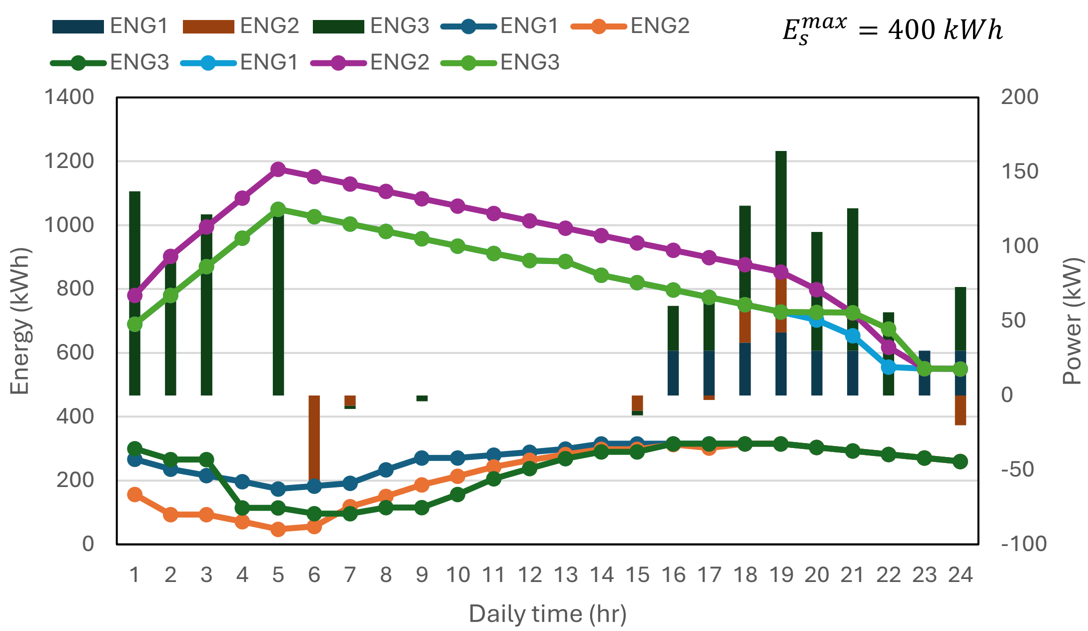

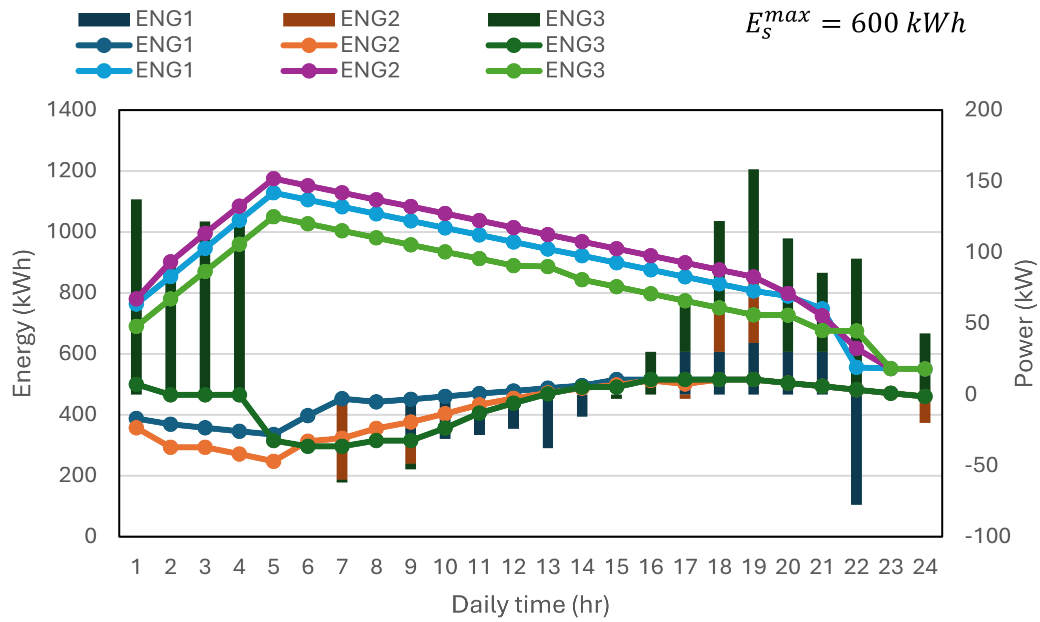

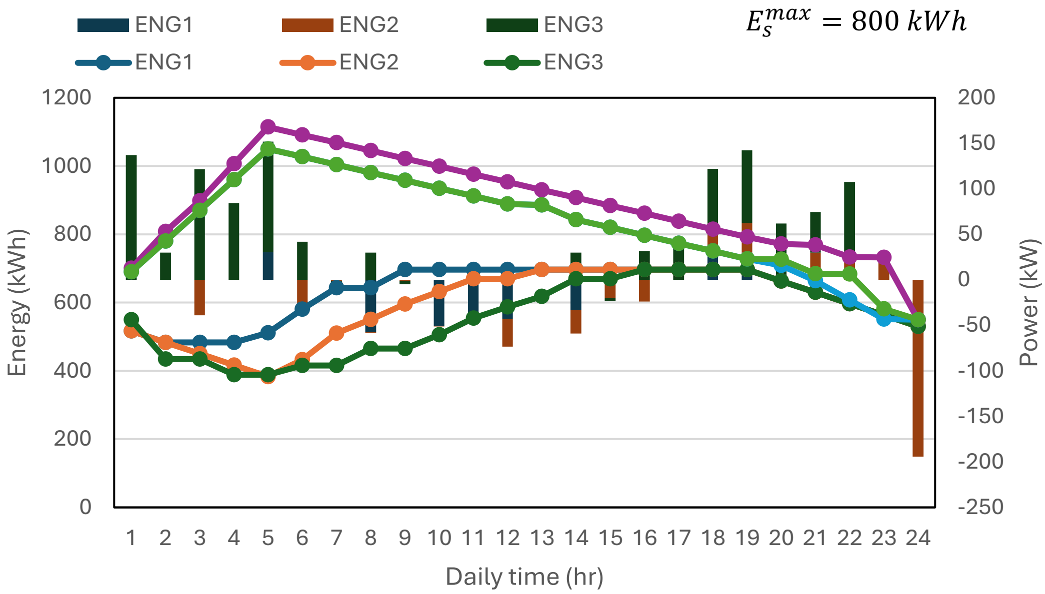

Figure 3-6. Daily energy management in case 2: energy available at BESs and EVs parking, and power trading between ENGs and upstream network.

Table 3-5 shows how different levels of maximum electric vehicle discharge power ($P_{dis,ev}^{max}$) influences the generation mix and costs. As it can be seen, the increase and decrease in this parameter might not change the type of ENGs and the three buildings are all AC nanogrids. This is predictable because changes in this parameter have similar and common effect in both DC and AC investment cost and power balance equations. On the other hand, changes in this parameter do not have a significant impact on the mix of ENGs' generation systems, corresponding installation capacity, and the capacity of the BES. Consequently, investment and maintenance costs would not have meaningful variation.

As expected, since electric vehicles should contribute to supply customer demand during peak load hours and should be charged in the morning early a day, the variation in the maximum discharge power of electric vehicles can only affect the hourly power generation pattern and the operating cost of DERs. At ENG 1, once $P_{dis,ev}^{max}$ is not more than 50 kW, the operation cost is low because there is not power enough in EVs park lot, so no need to charge them and buy electricity much from the upstream network. As a result, surplus electricity from the storage system can be sold.

By increasing $P_{dis,ev}^{max}$ to 100 kW, it reduces power sales and increases energy purchasing as EVs' charging increases. At higher values of this parameter, although the amount of charging power of EVs rises, EVs at peak load can assist generation systems in providing energy for customers, decreases power purchase, and rises the sale. As a result, the operating cost is reduced again. The bar chart in Figure 3-7 supports this idea; when $P_{dis,ev}^{max} = 100$ kW, purchasing electrical energy is considerably high, whereas for other amounts of this parameter, selling energy would overcome receiving it from the main grid.

Another noticeable point is the operation cost at ENG 2. When $P_{dis,ev}^{max} = 150$ kW, the capacity of the solar system has also increased slightly. So, the pattern of power generation and distribution at the building has changed.

In this case, electric vehicles at ENG 2 assist solar energy systems at peak time, and as the capacity of the solar system increases, there is no need to purchase electricity from the grid to charge electric vehicles at the early hours of a day. These reasons have led to a negative operation cost at this ENG. Looking at both Table 3-5 and bar chart in Figure 3-7, it is interesting that, although the increase in $P_{dis,ev}^{max}$ at ENG 3 may affect delivering and receiving electrical energy to/from the main grid, the operation cost of this active building does not vary in total. This implies that EV park lot has a neutral influence on the operation, generation mix, and the type of active building at ENG 3.

The line graph in Figure 3-7 shows that for all amount of $P_{dis,ev}^{max}$, BES system at three active buildings have to deliver electrical energy at early hours to help charge EVs' battery to be prepared for leaving the lot, with the exception of $P_{dis,ev}^{max} = 50$ kW and $P_{dis,ev}^{max} = 150$ kW at ENG 1 where energy storage at BES is stable. It is expected that, an increase in $P_{dis,ev}^{max}$ supports the generation system to supply the demand power, making EVs discharge their energy. This pattern definitely results in more charging at ENGs by purchasing from the main grid, DERs generation, and BES system. However, because the load demand at ENG 1 and ENG 3 at early hours of the day is more than that of ENG 2, energy at park lot at ENG 1 and ENG 3 dips first, then rises as ENG 2.

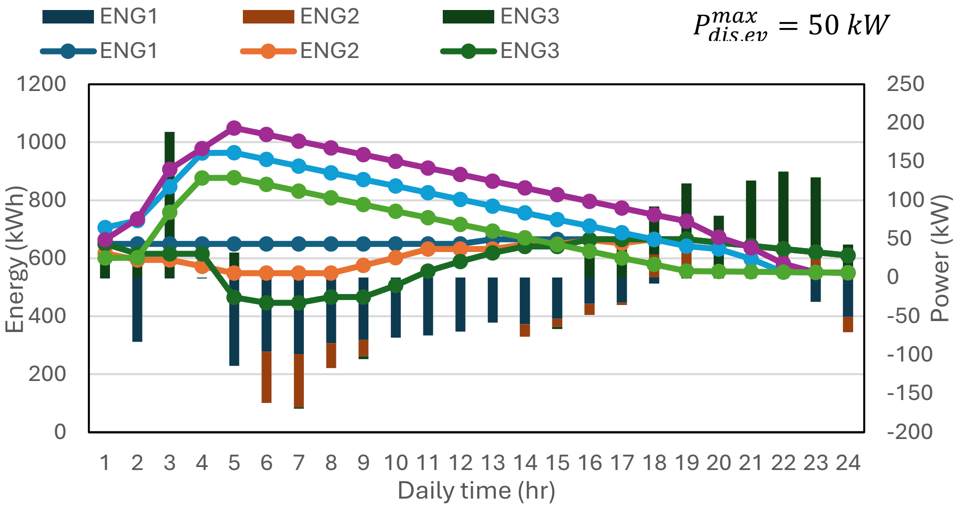

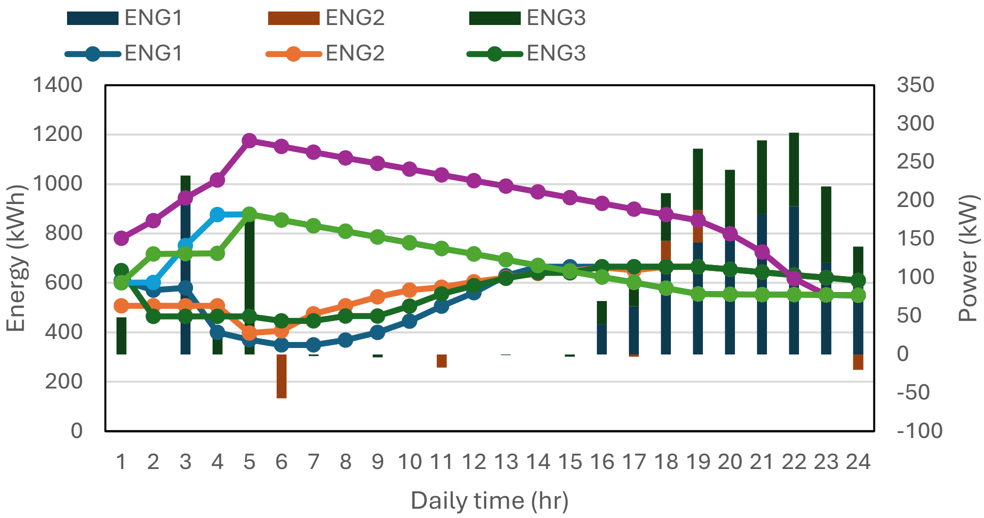

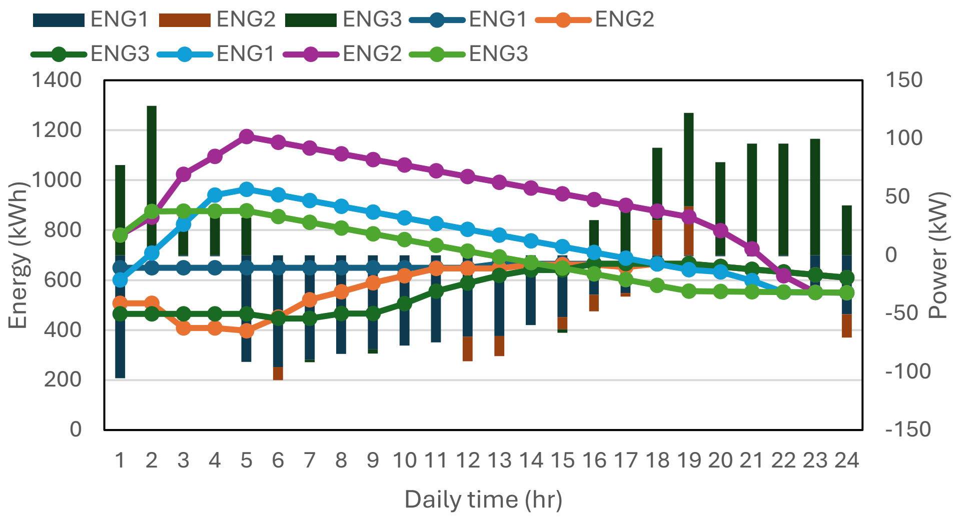

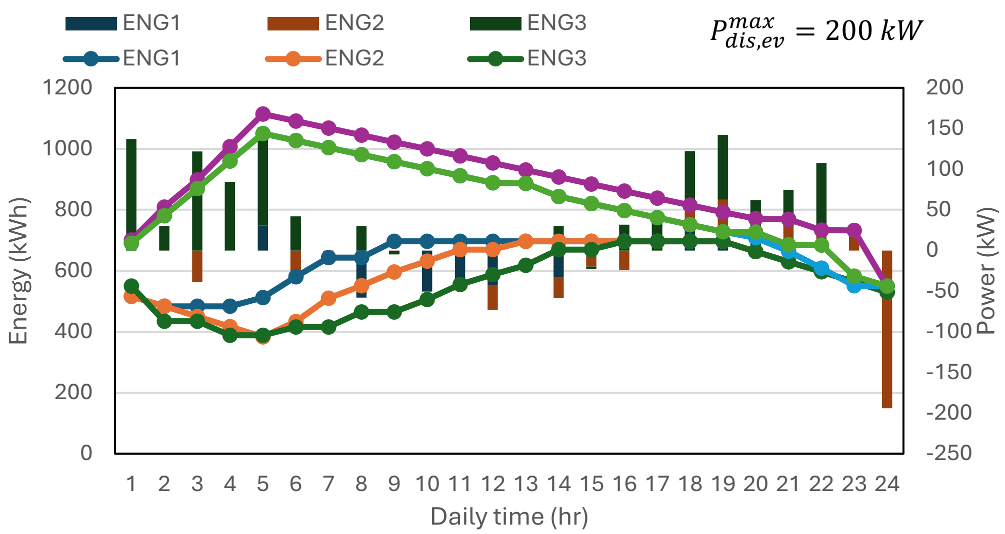

Figure 3-7. Daily energy management in case 3: energy available at BESs and EVs parking, and power trading between ENGs and upstream network.

3.4 Key findings and conclusion

This chapter has presented a planning framework for active buildings as an Energy Nano-Grid with the goals of determining the optimal size and the generation mix of the distributed energy resources and battery energy storage system, the ENG type (AC or DC), as well as the optimal daily load sharing as an energy management (EM) system. To implement a deep assessment, three factors have been considered: ratio of DC load, maximum allowable installation capacity of BES, and upper bound of EVs' discharge power availability, for various case studies and a MILP solver has been adopted. According to the simulation results, the type of ENGs would be DC when the rate of the DC load increases, through reducing investment and operation costs. The stability of demand and capacity constraints meant that this parameter did not have a major influence on the generation mix, the capacity of DERs and BESs and the energy of EVs in the park lots. In contrast to the DC load percentage, the maximum capacity limit for the BES system can directly change the capacity of the DERs and the investment and operating costs, as it plays an important role, sometimes as a supply resource and sometimes as a load. So, it might modify the pattern of generation and consumption. Due to not having a significant role at ENGs during the whole day, different level of EVs' maximum discharge power does not make any meaningful changes in the generation mix and in the investment cost. However, it could only change the power supply at peak hours. So, operation cost and discharge power of EVs parking are the only factors that vary noticeably. Because of increase in various gadgets and dc loads in the user side such as computer, TV, refrigerator and so on, working in different voltage levels and consumption pattern, it would be meaningful to analysis these types of loads individually, and be significant to evaluate how they separately affect the other variables and planning results. These points may be the future study perspective of the author.

Apendix 1

Nomenclature

The symbols used in this chapter are listed and defined in this appendix.

Indices and Sets

n	Index for ENGs
t	Index for time interval
d	Index for days in a year
y	Index for years of planning horizon
i	Index for DERs
T_{in}	Set of hours that EVs are at ENG
T_{out}	Set of hours that EVs are out of ENG

Inputs

NE	Total number of ENGs
NT	Total number of periods [hour]
ND	Total number of days in a year [day]
NY	Total number of years [year]
NI	Total number of DERs at each ENG
CR	Investment cost of DERs [$/kW]
CS	Investment cost of BES [$/kWh]
CRE	Investment cost of rectifiers [$/kW]
CC	Investment cost of converters [$/kW]
CI	Investment cost of inverters [$/kW]
CB	Investment cost of bidirectional converter [$/kW]
CT	Investment cost of transformers [$/kW]
l	Rate of DC load to total load at ENG [%]
L^{max}	Load peak at ENG [kW]
L	Power demand at ENGs [kW]
α	Critical load rate at ENG [%]
P_g^{max}/P_g^{min}	Maximum and minimum power purchased from the grid [kW]
P_s^{max}/P_s^{min}	Maximum and minimum power sold to the grid [kW]
C^p/C^s	Price of power purchased/sold from/to the grid [$]
B	Large positive constant

M^w/M^p	Maintenance cost of wind and photovoltaic generation systems per unit [$/kW]
Q	Efficiency of converters [%]
β	Efficiency of generation for DERs [%]
γ	Coefficient of sunlight intensity for PV systems [%]
$P_{ch}^{max}/P_{dis}^{max}$	Upper limit for charging/discharging power at BES [kW]
$P_{ch}^{min}/P_{dis}^{min}$	Lower limit for charging/discharging power at BES [kW]
$P_{ch,ev}^{max}$	Upper limit for charging power at EV’s park lot [kW]
$P_{dis,ev}^{max}$	Upper limit for discharging power at EV’s park lot [kW]
$P_{ch,ev}^{min}$	Lower limit for charging power at EV’s park lot [kW]
$P_{dis,ev}^{min}$	Lower limit for discharging power at EV’s park lot [kW]
$P_{ev,out}^{dis}$	Discharging power per Km for EVs’ journey [kW]
$U_s(0)$	Initial available energy at BES [kWh]
$U_{ev}(0)$	Initial available energy at EV’s park lot [kWh]
$\Delta U_s/\Delta U_{ev}$	Small off-set energy to avoid end-of-horizon effect at BES and EV park lot [kWh]
P^{max}/P^{min}	Upper and lower limit for the capacity of DERs [kW]
E_s^{max}/E_s^{min}	Upper and lower limit for the capacity of BES [kWh]
$U_{ev}^{max}/U_{ev}^{min}$	Upper and lower limit for energy at EV’s park lot [kWh]
N	Total number of EVs at an ENG
D	Average distance of movement each EV traverses a day [Km]
T_l	Time that EVs leave ENG [hr]
λ	Discharge rate of EVs per Km
r	Discount rate
k	Coefficient of net present value
z/Z	Coefficient of upper and lower energy limit for BES
Outputs	
IC	Total investment cost [$]
OC	Total operation cost [$]
MC	Total maintenance cost [$]
P	DERs’ capacity installed at ENGs [kW]
E	BES capacity installed at ENGs [kWh]

A	Binary variable representing ENG's feeder (0 if ac,1 if dc)
P_g	Power flows from grid to ENGs [kW]
P_c	Power flows from ENGs to the grid [kW]
P_p/P_w	PV and wind power generation at ENG [kW]
P_s^{ch}/P_s^{dis}	Charging/discharging power of BES [kW]
P_{ev}^{ch}/P_{ev}^{dis}	Charging/discharge power of EVs [kW]
I_s^{ch}/I_s^{dis}	Binary variable showing charging/discharging status of BES
I_{ev}^{ch}/I_{ev}^{dis}	Binary variable showing charging/discharging status of EVs
e_s/e_{ev}	Available energy at BES and EVs' park lot [kWh]
e_s^{max}/e_s^{min}	Upper and lower limit for available energy at BES [kWh]
I_g/I_c	Binary variable showing the direction of power exchange between the grid and ENGs
I_R	Binary variable representing the existence of DERs

Chapter 4 Energy management in small scale AC/DC microgrids

Abstract

This chapter provides an energy management system which control a day-ahead economic dispatch in an active small scale grid-connected AC/DC microgrid, so as to minimise the total energy cost due to the purchase of energy from the main grid. Local controllers (LCs) manage charging/discharging rate of controllable BESSs and EVs with smart charging strategy, while household demand and some EVs with dump charging strategy are considered as uncontrollable loads. This model also aims to maximize PV systems usage during nonpeak hours to reduce total energy price and shave load profile by increase in BESS and smart EVs' contribution to load supply at peak hours. Briefly, contributions of this chapter are listed below:

- Smart and dump charge strategies for EVs and evaluate their impact on self-consumption and energy management.
- Peak shaving is realizing for the main grid without considering its restriction in the model.
- Implementation of the model in a real-world case study.

4.1 Methodology

In this chapter, an AC/DC hybrid active small scale microgrid that can exchange power with the upstream network is considered. This network includes a DC bus connecting a PV system, a storage system and a parking lot with bidirectional plugs for charging/discharging smart EVs. "Smart EVs" refers to those vehicles whose owners have contracted with microgrid operators to share vehicle batteries with microgrids to achieve economic and technical goals. In fact, they let the microgrid controller (MC) adjusts their charging/discharging rates and periods. This DC bus is connected to an AC bus (main grid) through a bidirectional AC/DC converter which supply uncontrollable loads and not controllable EVs that can be recharged at a fixed rate and period. A complete structure of such a microgrid is illustrated in Figure 4-1. In this microgrid, each source has a local controller that controls corresponding component to reach the whole energy management. Each LC communicates with the MC that exchanges data with distribution system operator (DSO) to provide overall energy management which means a daily economic flow for all sources and loads.

This methodology implements a maximum power point tracking (MPPT) controller for PV system so that they operate in the highest power point during days, especially at noon which PV can generate maximum power [64]. Since during this time, there is no peak load and almost EVs are out of parking lot, surplus power can be stored at BESS and some EVs that may not leave the lot, in addition to supply uncontrollable demand. This would lead to a dip in energy bills for customers and make flexible sources to share the stored energy at peak hours. Note is that energy price identified by DSO is assumed to be dynamic so that it has the highest value at peak load hours.

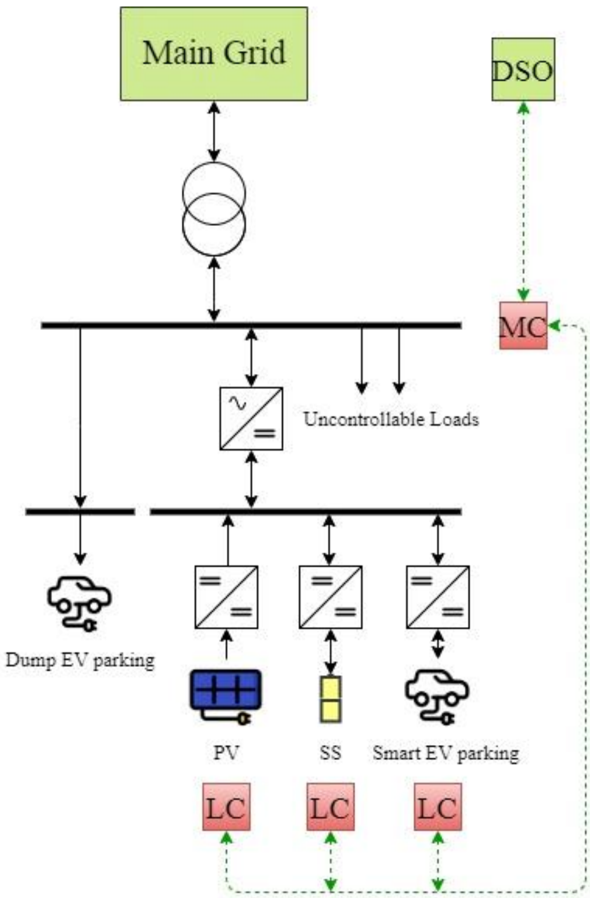

Figure 4-1. AC/DC hybrid microgrid structure.

4.2 problem formulation

To model the proposed strategy, it is vital to identify the mathematical models of each component in the microgrid like controllable/uncontrollable loads, solar system, storage systems and EVs. The following subsections describe the proposed models for the components shown in Figure 4-1.

4.2.1 Controllable/uncontrollable loads

In this chapter, there are two types of uncontrollable load profiles. The first one comprises critical loads, particularly road services, security point, video surveillance, lighting, etc (see Figure 4-1). This type of loads has predictable and largely constant demand profiles. Historical power consumption data is available for this loads. The second type of uncontrollable loads is a parking lot for dumb charging EVs. This station provides EVs with a slow charging rate. Here, customers owning these EVs have no contract with microgrid operators for their management. Therefore, they charge their EVs daily with a definite trend that is accessible from historical data.

On the other hand controllable load comprises a fast charge parking lot for smart EVs and a battery storage system station through a DC bus. These loads are referred to flexible ones because they can share their battery with the main grid to supply uncontrollable loads. So, the time and rate of charging/discharging of these sources is not predefined and is calculated by solving an optimization problem. In fact, the goal of this strategy is that, during the day, when PV may produce its maximum power, the BESS and EVs that are in the parking can store the surplus power and supply load at peak hours to shave the peak load and reduce the total energy cost. Anyway, there are some constraints for these sources that have to be meet when the optimization problem is run. These limits are as follows:

$$I_{ch}(t)P_{ch}^{min} \leq P_{ch}(t) \leq I_{ch}(t)P_{ch}^{max} \quad \forall t, BESS, EV \qquad (4\text{-}1)$$

$$I_{ds}(t)P_{ds}^{min} \leq P_{ds}(t) \leq I_{ds}(t)P_{ds}^{max} \quad \forall t, BESS, EV \qquad (4\text{-}2)$$

$$I_{ch}(t) + I_{ds}(t) \leq 1 \quad \forall t, BESS, EV \qquad (4\text{-}3)$$

$$E(t) = E(t-1) + P_{ch}(t) - P_{ds}(t) \quad \forall t, BESS, EV \qquad (4\text{-}4)$$

$$E^{min} \leq E(t) \leq E^{max} \quad \forall t, BESS, EV \qquad (4\text{-}5)$$

$$E(T_l) \geq E_t \qquad (4\text{-}6)$$

Both flexible loads (BESS and smart EVs) have similar operation modes and restrictions, as appears from the above equations. Inequalities (*4-1*) and (4-2) express that charging and discharging of BESS and EVs, P_{ch} andP_{ds}, must not exceed the lower (P_{ch}^{min}, P_{ds}^{min}) and upper limits (P_{ch}^{max}, P_{ds}^{max}). Binary variables I_{ch} and I_{ds} in (4-3) implies that these units cannot be charged and discharge simultaneously at each time interval t. In equations (*4-4*) and (4-5) $E(t)$

express how much energy is stored at batteries and parking lot at time t. Note that because time interval in this study is one hour, power rate signifies energy rate. Finally, equation (4-6) indicates that, at the time Tl when the intelligent vehicles leave the car park, there must be at least the required energy threshold E_t for electric vehicles in the car park.

4.2.2 Generation units

Upstream network and PV are the main responsible for supplying controllable and uncontrollable loads. Historical PV power generation records have provided possibility of implementing MTTP controller for solar system, so that if PV generation exceeds the power request from uncontrolled loads, the surplus power may be stored in the BESS and in the parking lot and/or sold to the main grid. Therefore, the power balance equation in the optimization problem is:

$$I_g(t)P_g(t) + P_{pv}(t) + P_{ds}(t) = P_l(t) + P_{ch}(t) + +I_m(t)P_m(t) \;\; \forall t \qquad (4\text{-}7)$$

Where $P_g(t)$, $P_{pv}(t)$, $P_l(t)$, $P_m(t)$ are the power purchased from the main grid, the PV power generation, the power requested by the uncontrollable load and the power sold to the main grid, respectively. $I_g(t)$ and $I_m(t)$ are binary variables that are restricted like in equation (4-3) showing that purchasing and selling power from/to the main grid can't occur at the same time. Equation (4-8) below represents the MTTP control and makes the PV system deliver its maximum power rate P_{pv}^{max} at each hour.

$$P_{pv}(t) = P_{pv}^{max}(t) \;\; \forall t \qquad (4\text{-}8)$$

4.2.3 Objective function

As it is said before, the total energy cost is the objective function to minimize. It includes the cost of purchasing energy from the upstream network mines the revenue from delivering surplus energy to the main grid. This function is formulated as follows:

$$C_{total} = \sum_t \Phi(t)[P_g(t) - P_m(t)] \qquad (4\text{-}9)$$

Where $\Phi(t)$ is energy price at time t that has a dynamic pattern during a day, so that has higher value at peak hours. The day-ahead energy price profile is assigned by the DSO and transferred every day to the microgrid users through the microgrid controller (MC). Then, optimization proposed model is performed and generation, charging/discharging patterns of renewable sources and flexible loads are commanded to local controllers (LC).

4.3 Numerical Analysis

In this section, we consider a small scale AC/DC microgrid like that is illustrated in Figure 4-1 as a case study. This grid is a park lot covered by solar panels over shelters. Here, we have two types of uncontrollable loads connected to a AC bus comprising road services like security point, video surveillance, lighting, etc, and EVs with dumb charging/discharging strategy that name V1G in this chapter. There is also a DC bus which connects PV, BESS, and parking lot for EVs with smart charging/discharging strategy, titled here V2G, to AC bus through a proper bidirectional converter.

We consider one day per season where there are different load profiles and photovoltaic generation. Furthermore, we want to assess how different energy scenarios, characterized by different values of the maximum installed PV power and the number of smart EVs, can influence the proposed model. Historical data for uncontrollable loads in a scenario and PV generation for these days are available and are shown in Figure 4-2 and Figure 4-3 respectively. EVs are supposed to have battery size 40 kWh, average 5 kWh charging/discharging, average daily movement 40 km/day, consumption 0.2 kWh/km. It assumed that smart EVs leave the lot at 7 a.m. and back there at 7 p.m. Note that smart electrical vehicles must have at least 70% of their energy capacity at their battery when they left the park lot, which is 28 kWh.

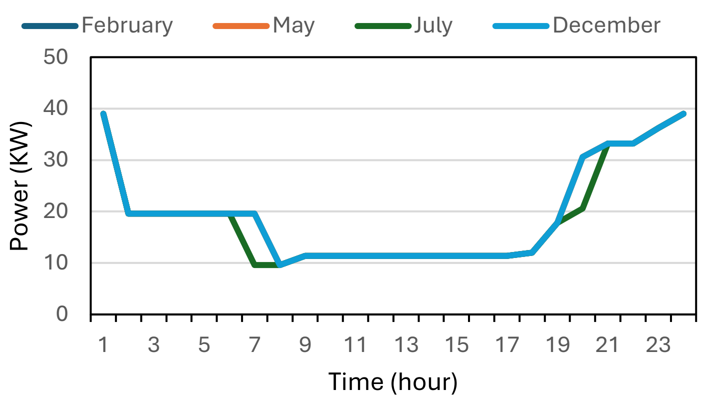

Figure 4-2. Demand profile for uncontrollable loads for 1st scenario in four seasons.

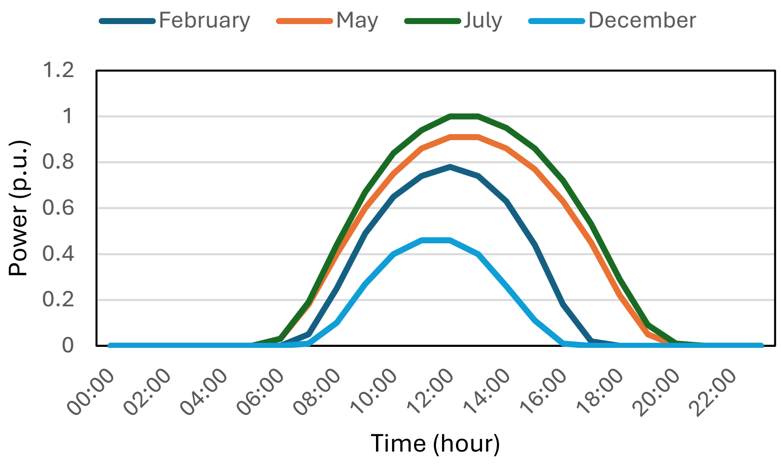

Figure 4-3. PV's power output for different seasons in [p.u.].

The energy scenarios have been defined by analyzing the most recent technical report on the European and Italian energy transition [105-110] and are represented in Table 4-1. In addition, daily purchase price varies according to the time and seasons so that at peak hours it has higher and at night-time it has lower amount. For non-domestic users it has been inferred from what is reported by ARERA [127] and presented in Table 4-2.

Table 4-1. Microgrid energy scenarios.

scenarios	2020	2030 DEC	2040 DEC
PV rated power [kW]	20	45	120
BESS capacity [kWh]	50	50	50
V1G/V2G number	5	10	25

Table 4-2. Energy cost for non-domestic users.

	8 a.m.-7 p.m.	7 a.m.-8 a.m./ 7 p.m.-11 p.m.	11 p.m.-7 a.m.
February	0.078	0.076	0.062
May	0.04	0.042	0.031
July	0.048	0.05	0.038
December	0.08	0.074	0.057

Figure 4-4 to Figure 4-6 show the power purchased from the main grid, energy available at EVs parking and BESS respectively, relating corespponding values and daily hours in four seasons and three scenarious. It is note that althogh this system is a non-domestic one, so the energy taarif is like for a industry users, demand trend follows a residential supply since some fixed loads like road lighting during the day is removed and some other like V2G electrical vehicles are out of the parking.

Figure 4-4 illustrates, during day hours (8 a.m. to 18 p.m) at which critical load is decreased and all EVs are out, the power coming from the upstream network is dropped in all seasons and scenarios that means peak shaving is reached in this period, peak load is at night time though. This is reasonable because during this period PV system that follows maximum powr point tracking generates its maximum power freely. In addition, at these hours, according to Table 4-2, energy price has its maximum value; therefore, it is expected that optimization problem would decide to improve self-consumption, in another work supplying load more by PVsystem and BESS. Note that EVs leave the park lot in this time period.

Speaking in details, it is abvoius that in the third scenario self-consumption and peak shaving is more considerable than first two ones (see Figure 4-4 to Figure 4-6); so this scenario could be the best one for the future energy planning. In this scenario, in December and February that the sun sets earlier than May and July and PV generates lower energy, in the afternoon, we can see purchasing energy from the grid and BESS discharging (see Figure 4-4 (c) and Figure 4-6 (c)). While BESS would be charged in May and July. Another reason is that, according to Table 4-2, energy price in these two months are meaningfully cheapper that December and February. In general, in all scenarios, when there is no sunlight, microgrid demand is provided by the main grid. Specially, at the day early hours that energy price is lower than other periods, smart EVs srart to be charged, and help to provide energy for demand at the peak load hours means from 7 p.m. to midnight (see Figure 4-5).

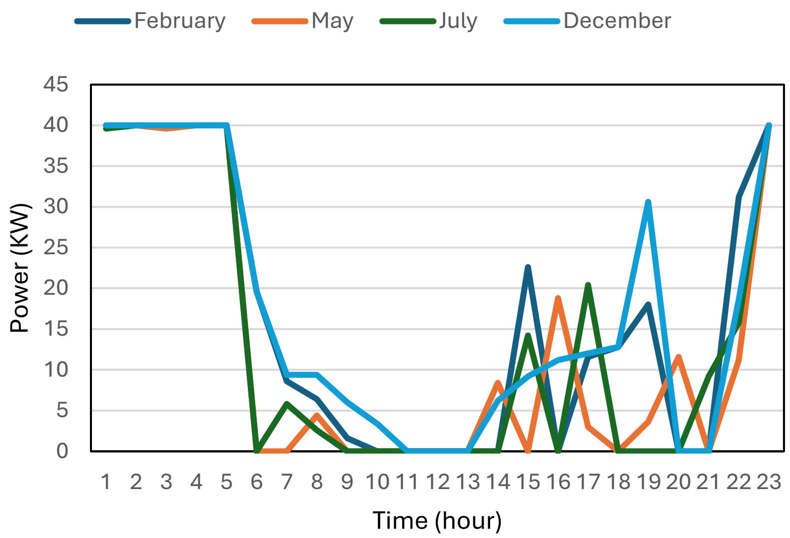

(a)

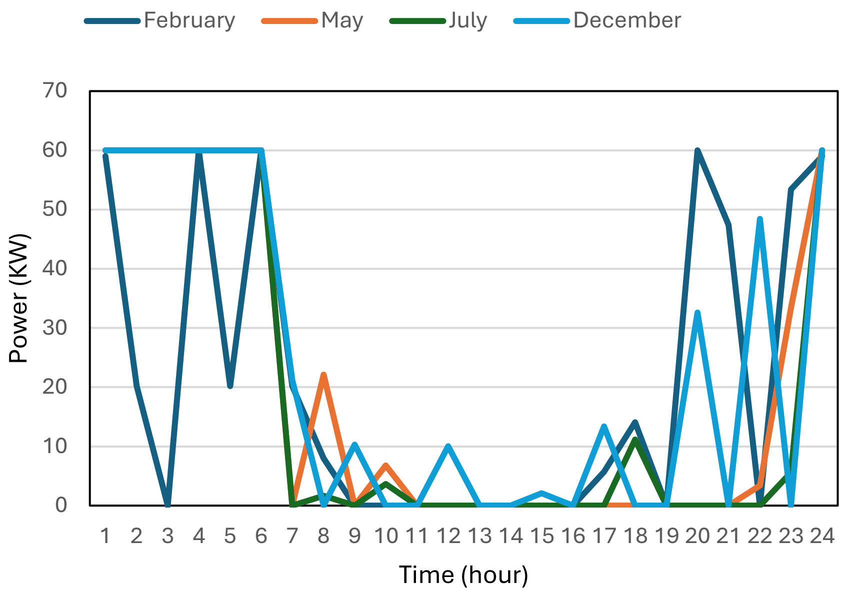

(b)

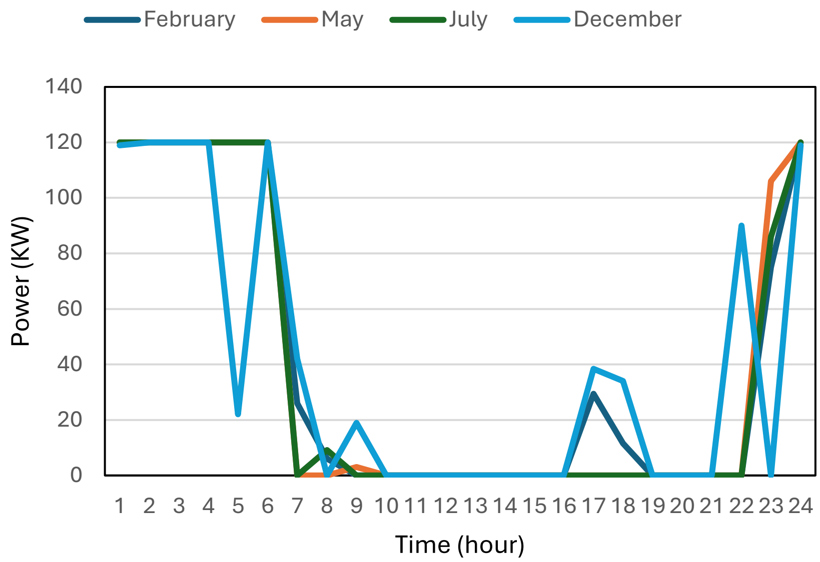

(c)

Figure 4-4. Power imported from the main grid. (a) first scenario; (b) second scenario; (c) third scenario.

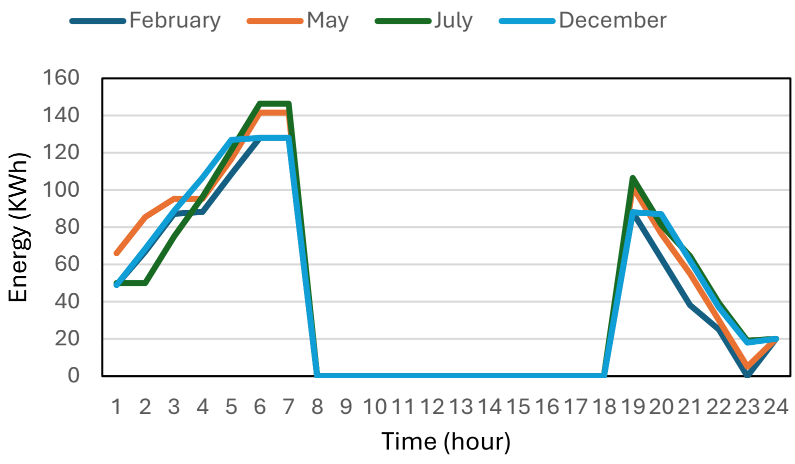

(a)

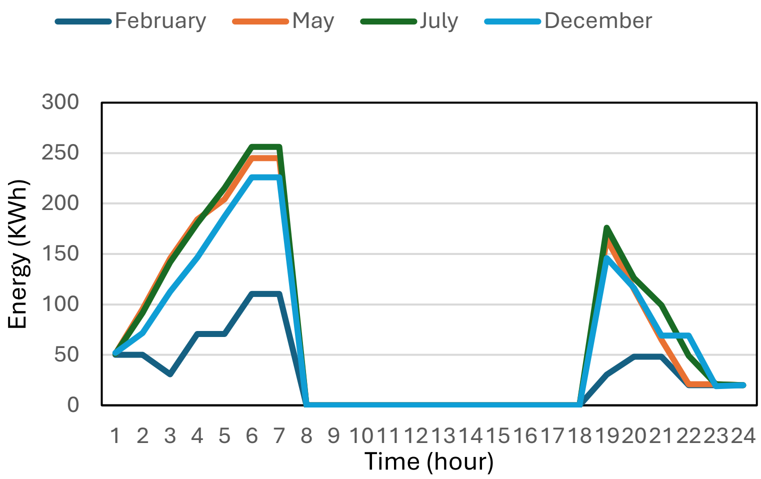

(b)

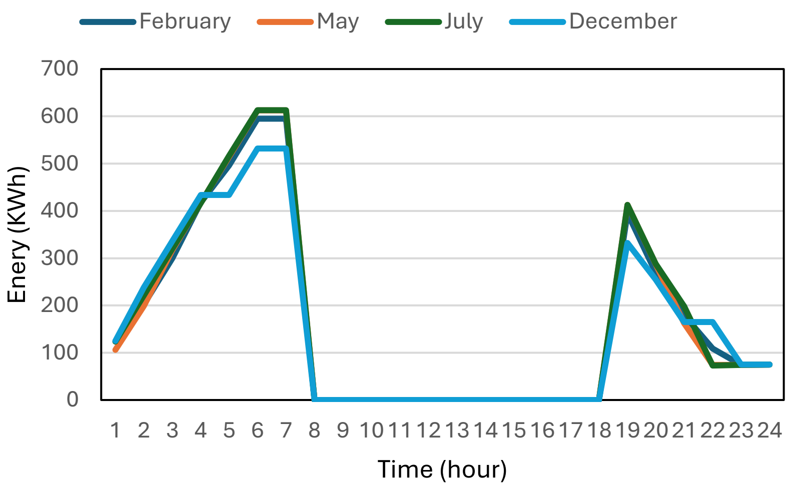

(C)

Figure 4-5. Energy available at EVs' park lot. (a) first scenario; (b) second scenario; (c) third scenario.

Furthermore, at the peak load hours, energy at BESS decreases largely (see Figure 4-6). Therefore, flexible sources play a vital role in self-consumption concept at peak load hours.

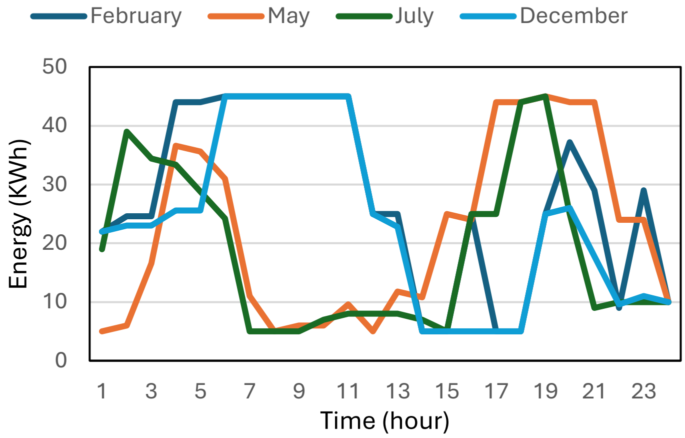

(a)

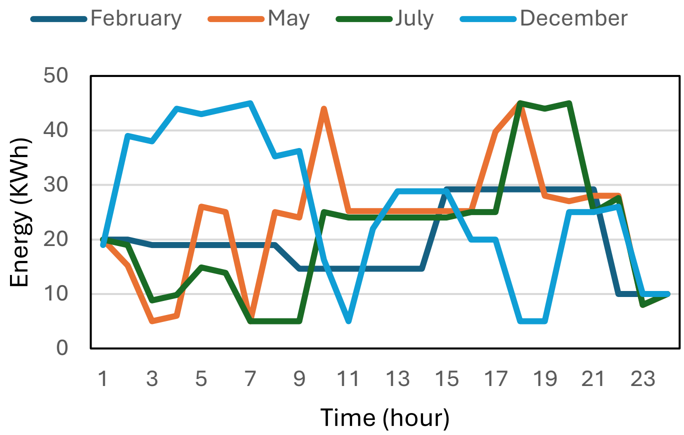

(b)

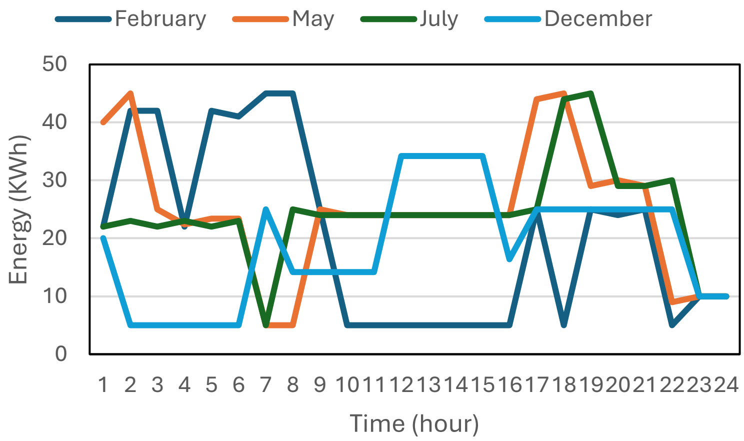

(c)

Figure 4-6. Energy available at BESS. (a) first scenario; (b) second scenario; (c) third scenario.

To charge/discharge at BESS at first hours of day is unlike to EVs' station. Loocking at Figure 4-6 we can perceive that operator would usually prefer BESS to be charged in February and December since it is expensive for the operator to charge them in the middle of day. Wherase, in May and July it suggests discharging to BESS due to economic charging price during the day.

Regarding economic issues, Figure 4-7 represents tha average power sold to the main grid for three scenarious. It is reasonable that during the middle-day hours that energy price is more than other hours, and PV systems can generate satisfactory power to supply demand, we have the most economic period, meaning microgrid sells its surplus energy to the grid. Another point is that there is another sale peak where EVs return to the park lot and their batteries have a lot of energy; so, curtail energy is sold to the main grid.

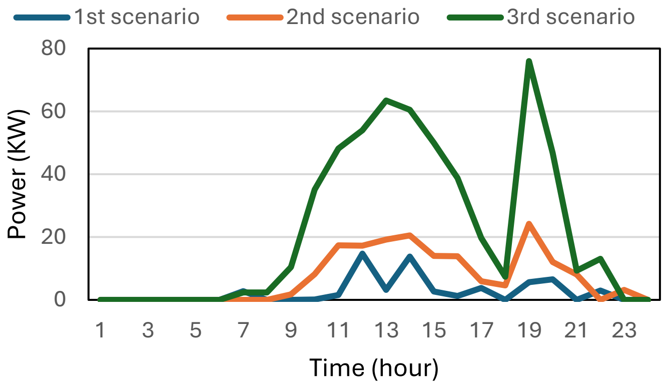

Figure 4-7. Average power sold to the main grid.

4.4 Key findings and conclusion

The fourth chapter has presented an optimization model to reach an optimal energy management focusing on self-consumption through renewable system and flexible loads like electrical vehicles and battery energy storage system. Different energy scenarios have been considered with different data from different seasons of the year. Results show that depending on the energy prices in seasons and different scenarios, self-consumption and purchasing energy vary. EV station's charge/discharge rates for smart vehicles mostly follow a constant and smooth trend, unlike storage system that change depending on the months and scenarios. Economic analysis is also done in this chapter which show PV and flexible loads have a significant role for microgrid operator to earn a good income.

Chapter 5 Short-circuit Calculations in Hybrid AC/DC Microgrids

Abstract

This chapter proposes a generalized approach that can be used for calculating AC/DC short-circuit currents in hybrid AC/DC microgrids, independently of the characteristics of the hybrid system. The methodology is based on the main equations of the IEC 61660 standard, employed for the calculation of equivalent resistances for a matrix formulation of the problem. This methodology can be applied to both radial and meshed structures since, as it is further clarified in this chapter, meshed structures can also be reduced to simpler radial configurations. To demonstrate the robustness of this proposed method, two test microgrids are examined and the results are compared with those obtained with the modelling software Neplan 360.

5.1 Methodology

Figure 5-1 shows a generic topology of a DC microgrid with N buses, loads, and sources. Each DC source can be a rectifier, a battery energy storage system (BESS), a capacitor, or a DC motor (Figure 5-2). Other types of DC sources, such as fuel cells or photovoltaic systems, are not considered because the IEC 61660 standard does not provide any guidance for calculating the short-circuit current in the presence of such elements.

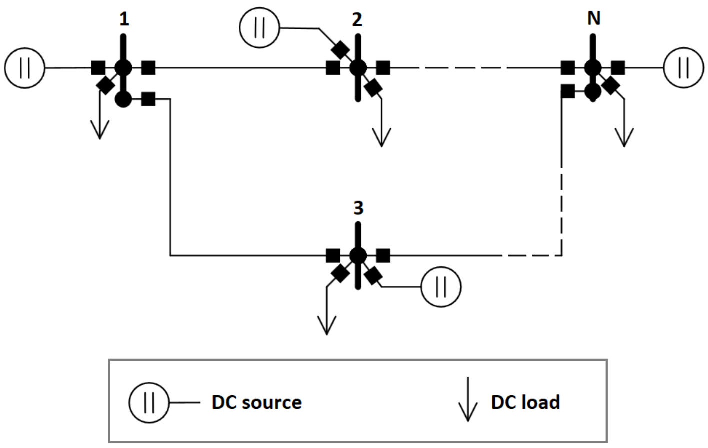

Figure 5-1. Generic representation of a DC microgrid with N buses.

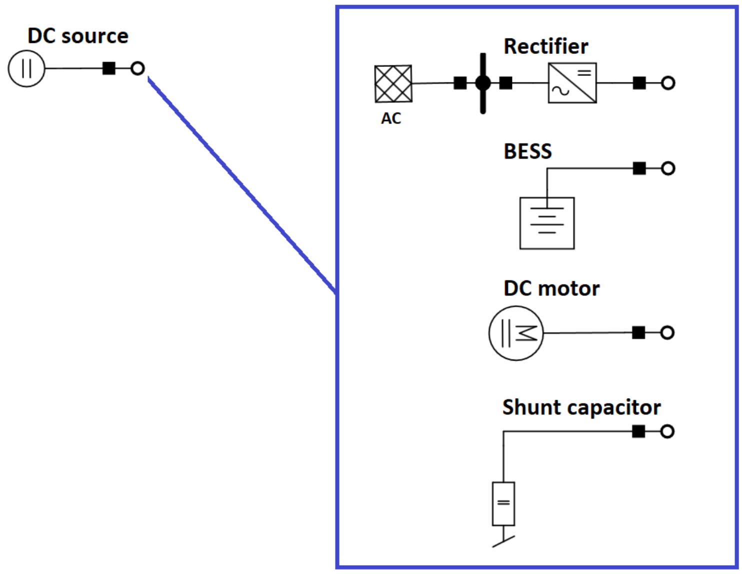

Figure 5-2. DC sources considered in the study according to IEC 61660.

Rectifiers are located at the connection points between DC microgrids and AC grids, and their presence will be used to include the fault current contribution of the main AC system into the calculation.

The steady-state short-circuit current calculation at a generic ith bus of the DC microgrid in Figure 5-1 is performed by calculating the short-circuit conductance matrix $[G_{SC}]$ [75, 76]. According to this method, the short-circuit current is found to solve the matrix equation:

$$[I_F] = [G_{SC}][U_0] - [G_{SC}][U_F] \tag{5-1}$$

Where $[I_F]$ is a vector that has all null elements except the i^{th} element, which is the fault current $I_{F,i}$ at the i^{th} node, $[U_0]$ is a vector whose elements are the voltages at the nodes of the DC microgrid, which are assumed to be equal to the rated voltage of the system, or to the pre-fault voltages obtained by means of the load flow analysis of the microgrid. Finally, $[U_F]$ is a vector whose elements are the voltages at the nodes of the DC microgrid during the fault. The i^{th} element of $[U_F]$ is set to zero in the case of a bolted short-circuit fault (i.e., zero impedance), all other elements, including the fault current, are the unknowns of the system. Equation (5-1) represents, therefore, a system with N equations and N unknowns (1 current and N-1 bus voltages). The diagonal element G_{kk} of the conductance matrix $[G_{SC}]$ is obtained as the sum of all conductances of all elements connected to the kth bus. The extra-diagonal element G_{kh} of the matrix is the opposite of the sum of all conductances of all elements connecting buses k and h. For calculating the contribution of a DC source to a generic G_{kk} element, the expressions reported in the standard IEC 61660 are used. A more detailed description of the IEC 61660 approach is not in the scope of this thesis and can be found both in [66] and in [71].

In the case of a BESS, the equivalent resistance of the source is given by:

$$R_{BB} = \frac{0.9 \cdot R_B + R_{BL}}{0.95 \cdot k_B} \tag{5-2}$$

where R_B is the short-circuit resistance of the battery provided by the manufacturer, R_{BL} is the resistance of the connection cable from the battery to the DC bus, k_B is a coefficient set to 1.05 for charged batteries and to 0.9 for low-charged batteries. The battery voltage before and during the fault is set to the rated voltage of the DC microgrid.

DC motor resistance is simply the resistance of the DC circuit from the output terminal of the motor and the DC bus. In the case of a shunt capacitor with rated capacity C, the equivalent resistance of the source is given by:

$$R_{CB} = \frac{R_{CL}}{k_C} \tag{5-3}$$

where R_{CL} is the resistance of the connection cable from the capacitor to the DC bus and k_C is a coefficient given by IEC 61660 and dependent on the inductance L_{CL} of the same connection cable and on the frequency $\omega_o = 1/\sqrt{L_{CL}C}$. This resistance can be used for calculating the peak value of the short-circuit current, but for steady-state contribution the resistance must be set to infinity.

Finally, in the case of rectifier, the equivalent resistance of the source must consider the contribution of the AC grid upstream of the converter. Using the expressions in IEC 61660, the following resistance can be obtained:

$$R_{CONV} = \frac{1}{c}\left(\sqrt{\frac{2}{3}} \cdot \pi \cdot \frac{Z_Q}{\lambda_d} + R_{loss} + R_{RL}\right) \tag{5-4}$$

where Z_Q is the module of the short-circuit impedance of the AC grid at the input terminals of the rectifier referred to the DC-side voltage, calculated, according to IEC 60909 by neglecting the presence of the rectifier as a possible element for creating a reclosing loop during the fault on the AC side; λ_d is a coefficient provided by IEC 61660, whose value depends on the rate between the real and imaginary part of Z_Q and the rate between the resistance of the DC circuit downstream of the converter and the resistance of the AC circuit upstream of the converter; R_{loss} is an additional resistance that takes into account the internal power losses of the converter; and R_{RL} is the resistance of the connecting cable from the rectifier to the DC bus. Finally, in equation (*5-4*) the coefficient c is the voltage factor defined by IEC 60909, which is herein introduced to simplify the calculations.

Based on the same principle, it is possible to propose a similar approach for taking into account the presence of PV generators in the calculations. In DC microgrids, PV plants are connected directly to the DC bus or by a DC/DC converter and in both cases their contribution to the short-circuit current is always known and provided by the PV module manufacturer.
Since a photovoltaic field is composed of strings of modules connected in parallel, the short-circuit contribution ISC of a PV plant with NS strings during a fault in the DC microgrid can be expressed as:

$$I_{SC} = N_S \cdot I_{SC,mod} \tag{5-5}$$

where $I_{SC,mod}$ is the short-circuit current of a single PV module provided by the manufacturer. With the goal of calculating the maximum short-circuit current in the DC network, it is possible to define an equivalent short-circuit resistance of the PV field so that to also integrate this source in the proposed methodology:

$$R_{FV} = \frac{U_{out}}{I_{SC}} + R_{FL} \tag{5-6}$$

where U_{out} is the voltage at the output voltage of the PV plant, assumed equal to the rated voltage of the DC system and R_{FL} is the resistance of the connection cable from the PV field to the DC bus.

Using the above defined resistances and the resistances of the DC cables connecting the buses of the DC microgrids, all elements of the matrix $[G_{SC}]$ are known for the specific microgrid and the short-circuit current and the voltages in all buses during the fault are obtained by solving equation (5-1) written in explicit form:

$$\begin{aligned} 0 &= \sum_{k=1}^{N} G_{hk}(U_{0k} - U_{Fk}) \quad \forall h \neq i \\ I_{F,i} &= \sum_{\substack{k=1 \\ k\neq i}}^{N} G_{ik}(U_{0k} - U_{Fk}) + G_{ii}U_{0i} \end{aligned} \tag{5-7}$$

5.2 Case Study

The proposed approach is applied to four test microgrids [10, 11], three of which are parts of the hybrid MV/LV grid of Figure 2-2 in chapter 2 (Figure 5-3 in this chapter) including an underground station, a smart car parking, and a residential area, and one called a port area that is the more complex grid represented in Figure 5-4. For each microgrid, a DC-side fault is assumed to occur at the main DC bus. The faulted nodes are indicated in Figure 5-3 and Figure 5-4 and named:

- N1 for the underground station microgrid;

- N2 for the smart car parking microgrid;
- N3 for the residential area microgrid;
- N4 for the port area microgrid.

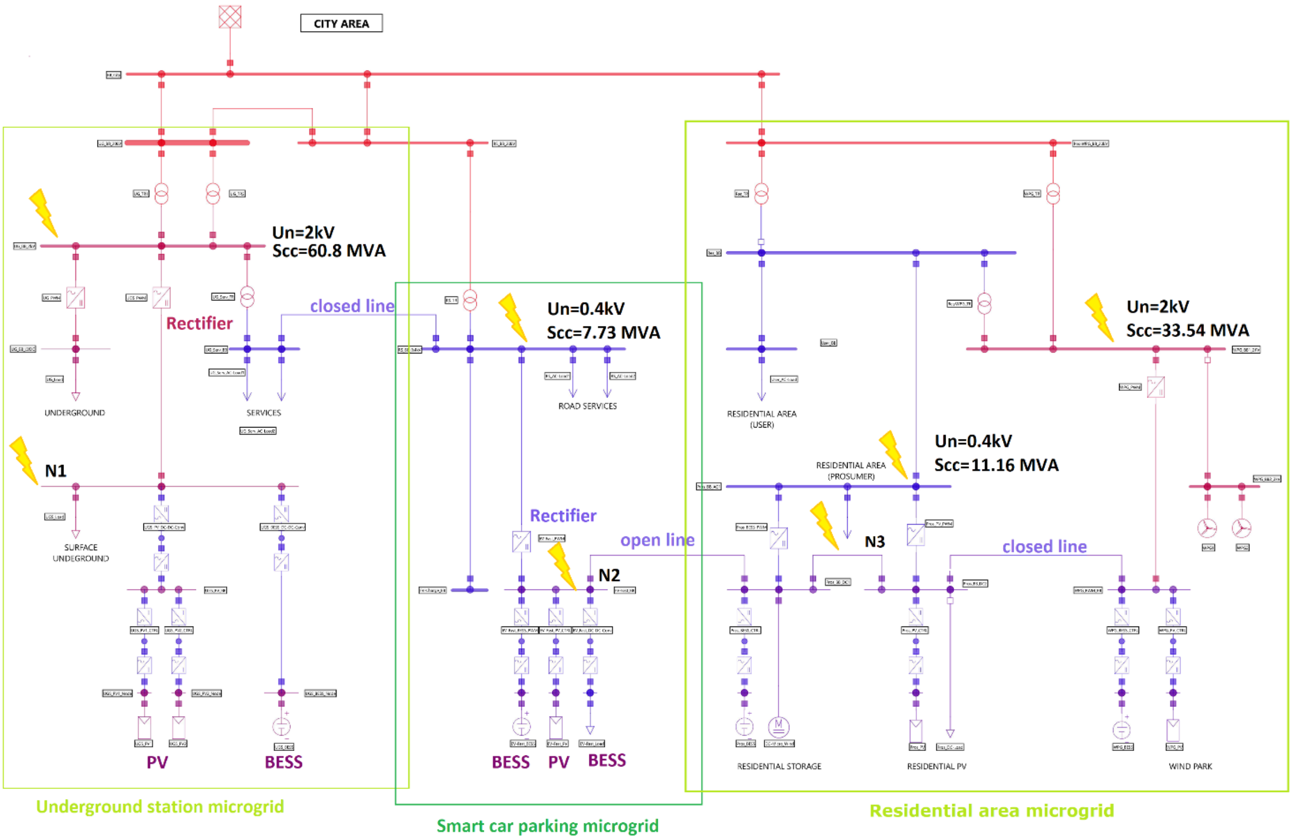

Figure 5-3. City area MV/LV AC/DC microgrid.

The figures show the state (i.e., open/close) of the AC lines since their state impacts the value of the impedance Z_Q in equation (5-4). According to the proposed methodology, the initial symmetrical short-circuit powers defined by IEC 60909 at the rectifiers input terminals, necessary for the Z_Q evaluation, are reported in Figure 5-3 and Figure 5-4. The four short-circuit currents are calculated considering the contribution of the PV plants and, where present, the contribution of the batteries of electric vehicles connected to the grid. Capacitors and DC motors are not present on any bus of hybrid grids.

The parameters for the calculation are reported in Table 5-1 to Table 5-4. The four tables report all the data necessary to calculate the expressions (5-2) to (5-7). For the AC grid upstream the fault location the rated voltage and the initial symmetrical short-circuit power at the rectifier input terminals are given to calculate the maximum short-circuit current on the AC side and the related equivalent short-circuit impedance. For rectifiers and BESSs, the output voltage, the rated power and the internal resistances are given. BESSs are considered charged for the calculation of the maximum short-circuit impedances (i.e., k_b=1.05).

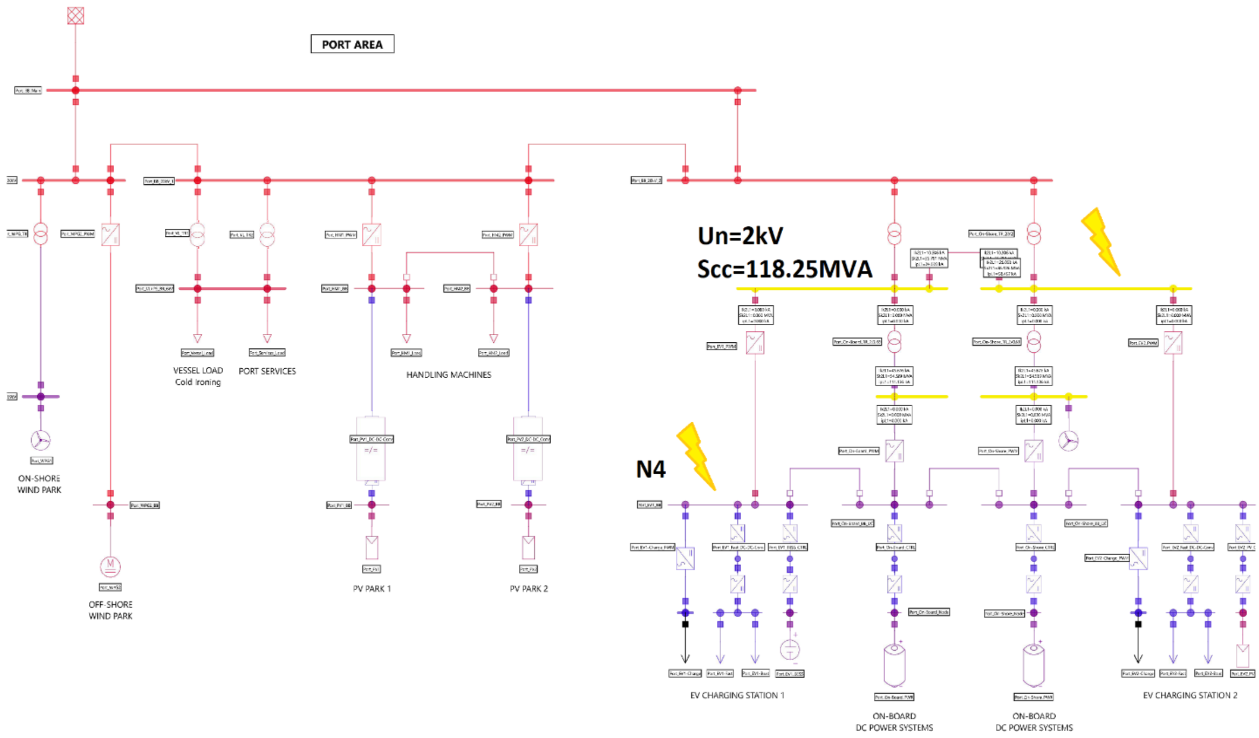

Figure 5-4. Port area MV/LV AC/DC microgrid.

For PV systems also the number of strings N_s and of modules N_m are provided, since the output voltage U_{out} depends on the number of modules connected in series (it is the sum of the output voltage of each series-connected module) and the short-circuit current I_{sc} depends on the number of strings, as expressed by equation (5-5). For all sources, the length of the connection cables and the related resistances are given; these data are necessary to calculate some of the coefficients appearing in the resistances in the IEC 61660 standard.

Table 5-1. Underground station microgrid: parameters for the calculations of the short-circuit current.

AC grid	Rated Voltage U_n=2 kV; Initial symmetrical short-circuit power at the input terminals of the rectifier S_{cc}=60.8 MVA
Rectifier	Output Voltage U_{out}=1.5 kV; Rated power S_r=800 kVA; Coefficient λ_d=0.97 (from IEC 61660); Internal resistance R_{loss}=0.001 Ω DC connection cable length d=5 m; DC connection cable series resistance R_{RL}=0.0025 Ω
BESS	Output Voltage U_{out}=1.5 kV; Charged battery k_B=1.05; Rated power S_r=250 kVA; Short-circuit resistance of the battery R_B=0.2 Ω; DC connection cable length d=50 m; DC connection cable series resistance: R_{BL}=0.025 Ω
PV	Output Voltage U_{out}=1.5 kV;

	Number of modules N_m=44; Number of strings Ns=3; Rated power S_r=50 kW; Module's short-circuit current $I_{SC,mod}$=12.1 A; DC connection cable length d=20 m; DC connection cable series resistance R_{FL}=0.011 Ω

Table 5-2. Smart car parking microgrid: parameters for the calculations of the short-circuit current.

AC grid	Rated Voltage U_n=0.4 kV; Initial symmetrical short-circuit power at the input terminals of the rectifier S_{cc}=7.73 MVA
Rectifier	Output Voltage U_{out}=0.6 kV; Rated power S_r=400 kVA; Coefficient λ_d=0.97 (from IEC 61660); Internal resistance R_{loss}=0.01 Ω DC connection cable length d=5 m; DC connection cable series resistance R_{RL}=0.0025 Ω
BESS	Output Voltage U_{out}=0.6 kV; Charged battery k_B=1.05; Rated power S_r=40 kVA; Short-circuit resistance of the battery R_B=0.2 Ω; DC connection cable length d=20 m; DC connection cable series resistance R_{BL}=0.011 Ω
EV BESS	Output Voltage U_{out}=0.4 kV; Charged battery k_B=1.05; Rated power S_r=400 kVA; Short-circuit resistance of the battery $R_{B,ev}$=0.2 Ω; DC connection cable length d=20 m; DC connection cable series resistance $R_{BL,ev}$=0.0007 Ω
PV	Output Voltage U_{out}=1.5 kV; Number of modules N_m=44; Number of strings Ns=3; Rated power S_r=50 kW; Module's short-circuit current $I_{SC,mod}$=12.1 A; DC connection cable length d=20 m; DC connection cable series resistance: R_{FL} =0.011 Ω

Table 5-3. Residential area microgrid: parameters for the calculations of the short-circuit current.

AC grid	Rated Voltage U_{n1} =2 kV Rated Voltage U_{n2}=0.4 kV Initial symmetrical short-circuit power at the input terminals of the rectifier S_{cc1}=33.54 MVA Initial symmetrical short-circuit power at the input terminals of the rectifier S_{cc1}=11.16 MVA
Rectifier (2 kV)	Output Voltage U_{out}=0.6 kV; Rated power S_r=2000 kVA; Coefficient λ_d=0.97 (from IEC 61660); Internal resistance R_{loss}=0.01 Ω DC connection cable length d=5 m; DC connection cable series resistance R_{RL}=0.0025 Ω
Rectifier (0.4 kV)	Output Voltage U_{out}=0.6 kV; Rated power S_r=2x400 kVA; Coefficient λ_d=0.97 (from IEC 61660); Internal resistance R_{loss}=0.01 Ω DC connection cable length d=5 m;

	DC connection cable series resistance R_{RL}=0.0025 Ω
BESS	Output Voltage U_{out}=0.6 kV; Charged battery k_B=1.05; Rated power S_r=200 kVA; Short-circuit resistance of the battery $R_{B,ev}$=0.2 Ω; DC connection cable length d=20 m; DC connection cable series resistance R_{BL}=0.011 Ω
PV	Output Voltage U_{out}=0.6 kV; Number of modules N_m=1111; Number of strings Ns=52; Rated power S_r=500 kW; Module's short-circuit current $I_{SC,mod}$=189 A; DC connection cable length d=20 m; DC connection cable series resistance: R_{FL} =0.011 Ω

Table 5-4. Port area microgrid: parameters for the calculations of the short-circuit current.

AC grid	Rated Voltage U_n=2 kV; Initial symmetrical short-circuit power at the input terminals of the rectifier S_{cc}=118.25 MVA
Rectifier (2 kV)	Output Voltage U_{out}=0.69 kV; Rated power S_r=3000 kVA; Coefficient λ_d=0.97 (from IEC 61660); Internal resistance R_{loss}=0.01 Ω DC connection cable length d=5 m; DC connection cable series resistance R_{RL}=0.0025 Ω
On-board BESS	Output Voltage U_{out}=0.69 kV; Charged battery k_B=1.05; Rated power S_r=2x10 MVA; Short-circuit resistance of the battery R_B=0.1 Ω; DC connection cable length d=20 m; DC connection cable series resistance R_{BL}=0.011 Ω
PV	Output Voltage U_{out}=0.69 kV; Number of modules N_m=888; Numero di stringhe Ns=42 Potenza nominale S_r=400 kW Lunghezza del cavo di collegamento in DC d=20 m Resistenza del cavo di collegamento in DC RFL= 0.011 Ω
EV BES	Output Voltage U_{out}=0.69 kV; Charged battery k_B=1.05; Rated power S_r=2000 kVA; Short-circuit resistance of the battery $R_{B,ev}$=0.2 Ω; DC connection cable length d=20 m; DC connection cable series resistance $R_{BL,ev}$=0.0007 Ω

5.2.1 Underground station microgrid

The microgrid belongs to an underground station with a floor area of 3000 m^2 and an annual passenger inflow of around 5.3 million, as in the case study described in [77]. From the data in Table 5-1, using the formulas in 5.1, the following quantities are calculated:

$$Z_Q = \frac{c \cdot {U_n}^2}{S_{cc}} \cdot \left(\frac{U_{DC}}{U_n}\right)^2 = \frac{1.1 \cdot 2^2}{60.8} \cdot \left(\frac{1.5}{2}\right)^2 = 0.0407\ \Omega$$

$$R_{CONV} = \frac{1}{c}\left(\sqrt{\frac{2}{3}}\cdot\pi\cdot\frac{Z_Q}{\lambda_d} + R_{loss} + R_{RL}\right) = \frac{1}{1.05}\left(\sqrt{\frac{2}{3}}\cdot\pi\cdot\frac{0.0407}{0.97} + 0.001 + 0.0025\right) = 0.101\ \Omega$$

$$R_{BB} = \frac{0.9\cdot R_B + R_{BL}}{0.95\cdot k_B} = \frac{0.9\cdot 0.2 + 0.025}{0.95\cdot 1.05} = 0.206\ \Omega$$

$$R_{FV} = \frac{U_{out}}{I_{SC}} + R_{FL} = \frac{1500}{36.3} + 0.011 = 41.32\ \Omega$$

For the short-circuit current calculation in *N1*, the microgrid can be represented by a simple 4-bus network where *N1* is indicated as bus 2 (Figure 5-5). The matrix $[G_{SC}]$, obtained using the coefficient of the system of linear equation (5-7), is:

$$[G_{SC}] = \begin{bmatrix} 9.88 & -9.88 & 0.00 & 0.00 \\ -9.88 & 14.75 & -4.85 & -0.02 \\ 0.00 & -4.85 & 4.85 & 0.00 \\ 0.00 & -0.02 & 0.00 & 0.02 \end{bmatrix}$$

$[G_{SC}]$ is a 4x4 square matrix being four the nodes involved in the calculation. Imposing that the voltage at buses 1, 3 and 4 during the fault are equal to the rated voltage of the microgrid (such hypothesis is realistic, since these voltages are those internal to the DC sources), the fault current obtained by (5-7) is 22.13 kA. The same current evaluated by Neplan 360® is 21.77 kA. The difference between the two values is, therefore, 1.6%.

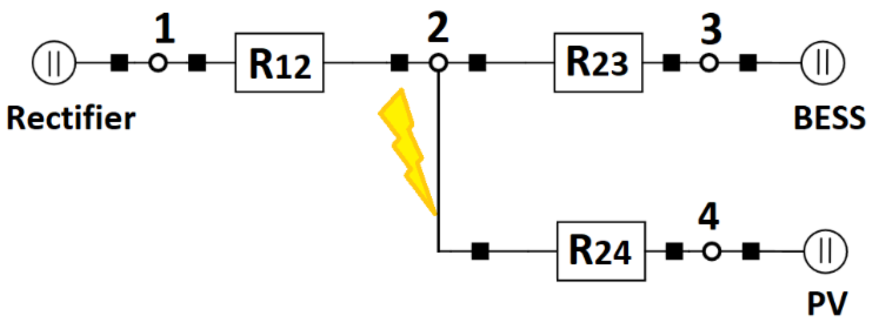

Figure 5-5. Schematic representation of the Underground station microgrid.

5.2.2 Smart car parking microgrid

The network under consideration, schematically represented in Figure 5-6, includes the supply of roadside services, charging stations for electric vehicles with slow charging and fast charging, and photovoltaic generation with a dedicated storage system. From the data in Table 5-2, similarly to sub-section A, the following quantities are calculated:

$$Z_Q = 0.0489\ \Omega$$

$$R_{CONV} = 0.135\ \Omega$$

$$R_{BB} = 0.206\ \Omega$$

$$R_{BB,ev} = 0.181\ \Omega$$

$$R_{FV} = 41.32\ \Omega$$

For the short-circuit current calculation in *N2*, the microgrid can be represented as a 5-bus network where *N2* is indicated as bus 2. The matrix $[G_{SC}]$, in this case, is a 5x5 matrix:

$$[G_{SC}] = \begin{bmatrix} 7.40 & -7.40 & 0 & 0 & 0 \\ -7.40 & 17.80 & -4.85 & -5.52 & -0.02 \\ 0 & -4.85 & 4.85 & 0 & 0 \\ 0 & -5.52 & 0 & 5.52 & 0 \\ 0 & -0.02 & 0 & 0 & 0.02 \end{bmatrix}$$

and the fault current is 10.68 kA. The same current evaluated by Neplan 360® is 10.90 kA with a difference between the two values of 2%.

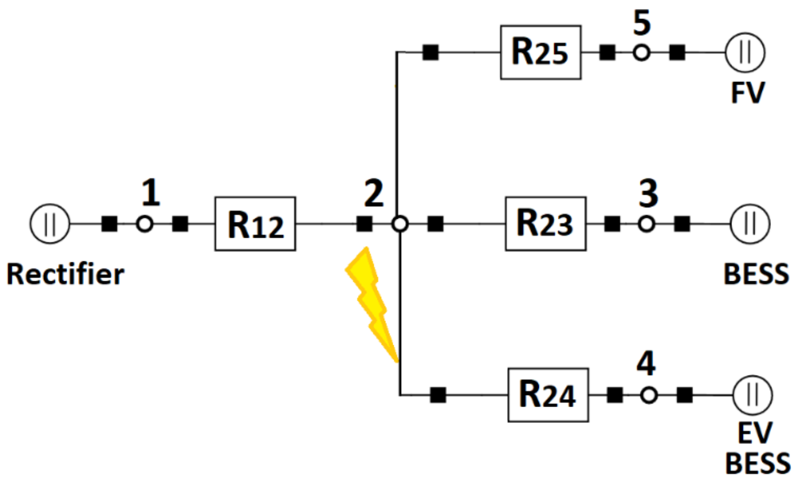

Figure 5-6. Schematic representation of the Smart car parking microgrid.

5.2.3 Residential area microgrid

For the purpose of calculating the short-circuit current at fault point N2, the Residential area microgrid is shown in Figure 5-7, where the collecting bus 2 represents the faulted node N3. From the data in Table 5-3, the following parameters for the solution of the system of linear equation in matrix form in equation (5-7) are calculated:

$$Z_{Q1} = 0.0113\ \Omega$$

$$Z_{Q2} = 0.0339\ \Omega$$

$$R_{CONV1} = 0.097\ \Omega$$

$$R_{CONV2} = 0.042\ \Omega$$

$$R_{BB} = 0.181\ \Omega$$

$$R_{FV} = 0.79\ \Omega$$

The matrix $[G_{SC}]$ in this case is:

$$[G_{SC}] = \begin{bmatrix} 10.28 & -10.28 & -5.52 & -5.52 & -1.27 & -24.23 \\ -10.28 & 47.41 & 0 & 0 & 0 & 0 \\ -5.52 & 0 & 5.52 & 0 & 0 & 0 \\ -5.52 & 0 & 0 & 5.52 & 0 & 0 \\ -1.27 & 0 & 0 & 0 & 1.27 & 0 \\ -24.23 & 0 & 0 & 0 & 0 & 24.23 \end{bmatrix}$$

and the fault current obtained from the resolution of equation (5-7) is 29.50 kA versus 29.13 kA evaluated by Neplan 360®. The difference between the two values is 1.3%.

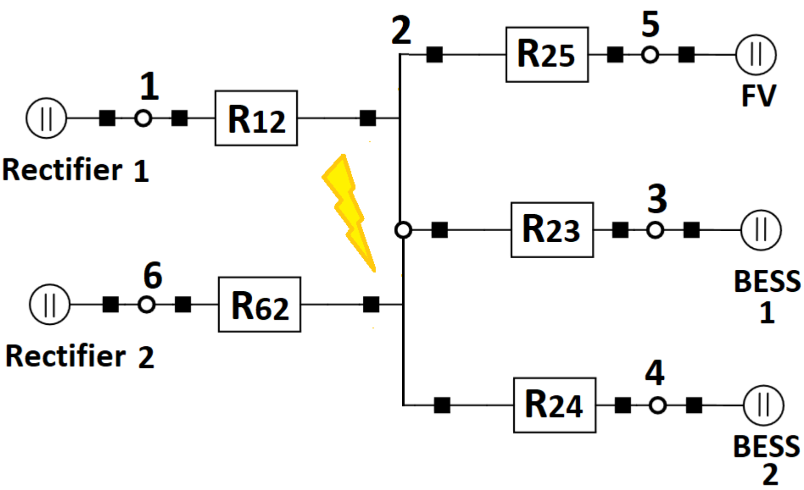

Figure 5-7. Schematic representation of the Residential area microgrid.

5.2.4 Port area microgrid

Figure 5-4 shows a Port Area microgrid. The DC fault point is indicated as N4. The network configuration has two rectifiers in parallel fed from the 2 kV busbars and another two rectifiers fed from the 0.69 kV busbars. When the fault occurs, it is possible to assume that the two rectifiers connected to the 2 kV busbars operate as a single element connecting the DC busbars with the AC busbars. In fact, the formulae proposed by IEC 61660 do not consider the rated power of the rectifier but only its presence. Therefore, since the two elements connect the fault node to the same source, they can be treated as a single element. The presence of the two rectifiers on the 0.69 kV busbars can be instead neglected. In fact, when the fault occurs, the rectifiers fed from the 2 kV busbars create a preferential path for the fault current compared to that formed by the 0.69 kV rectifiers and the 2/0.69 kV/kV transformers in the figure.

Consequently, the network can be represented as in Figure 5-8 where node 2 represents fault node N4.

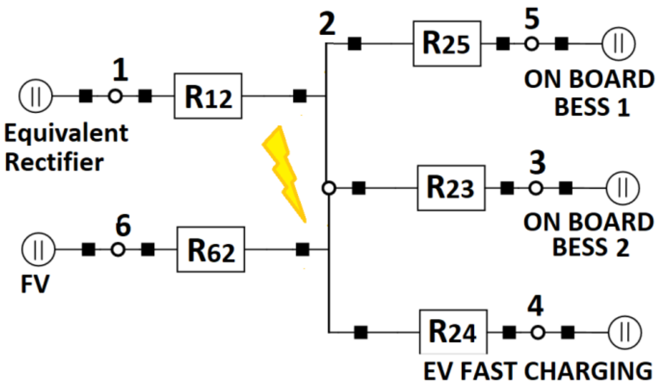

Figure 5-8. Schematic representation of the Port area microgrid.

From Data in Table 5-4 the following parameters are calculated:

$$Z_Q = 0.0042\ \Omega$$

$$R_{CONV} = 0.024\ \Omega$$

$$R_{BB,onboard12} = 0.091\ \Omega$$

$$R_{BB,EV} = 0.181\ \Omega$$

$$R_{FV} = 1.12\ \Omega$$

and, as a consequence:

$$[G_{SC}] = \begin{bmatrix} 42.23 & -42.23 & -10.99 & -10.99 & -5.52 & -0.89 \\ -42.23 & 70.63 & 0 & 0 & 0 & 0 \\ -10.99 & 0 & 10.99 & 0 & 0 & 0 \\ -10.99 & 0 & 0 & 10.99 & 0 & 0 \\ -5.52 & 0 & 0 & 0 & 5.52 & 0 \\ -0.89 & 0 & 0 & 0 & 0 & 0.89 \end{bmatrix}$$

Even in this case, bus voltages at nodes 1, 3, 4, 5 and 6 are assumed equal to the rated one at the DC side, therefore, from equation (5-7) a short-circuit current equal to 51.72 kA is obtained. The same current assessed by Neplan 360® is 49.79 kA, with a difference of 3.9% between the two values.

5.3 Key findings and conclusion

The research work in the chapter 5 is an extended version of [138], presenting a general methodology for short-circuit calculations in hybrid AC/DC microgrids. The proposed approach shows great accuracy and proves to be easy to apply in all cases where there is no specialized software for the calculation of short-circuit currents in hybrid DC microgrid. The matrix approach lends itself to an iterative implementation that is fairly simple to implement and easily automated. In addition, it allows to consider in a simple way also the presence of PV generators connected to DC buses crossing the limits of IEC 61660 standard.

The computational burden required by this methodology is that necessary for solving a *nxn* linear system and, as shown by the four different case studies, the accuracy of the solution does not change with the increase in the number of nodes of the networks. As to this aspect, the chosen case studies have from 4 to 6 nodes; in real-life microgrids a higher number of sources which can feed the fault are hardly expected, since the control of numerous distributed resources would be rather complex and impractical.

The method can be still improved and simplified by considering the additional indications of IEEE Standard 946-2020 [139]. As an example, according to [78], the contribution of DC motors and inductive loads to the short-circuit current can be conservatively estimated as ten times the motor's rated full-load current. This allows to eliminate from the microgrid graphs those nodes containing DC motors and inductive loads. In this way their fault contribution can be taken into account by adding it to the fault current calculated in the network without these elements, as similarly suggested for AC networks by IEC 60909. In a future work, this methodology will be applied considering the above-mentioned sources and new sources such as fuel cells and Li-ion (or other type of) batteries. In particular, in this case, it will be important to model the contribution of the static converter that interfaces the element to the DC grid.

Finally, a short note to promote a discussion on the topic of short-circuit calculation in DC grids: does the method provided by the IEC 61660 lead to the calculation of significant values of the short-circuit currents in modern smart grids with static converters with current limiters? This is a very important topic if the age of the standard is considered. Indeed, while smart grids are becoming more and more common in modern distribution systems, the number of static converter-interfaced distributed resources is increasing. It appears rather unrealistic to base the sizing of circuit-breakers and other components on short-circuit current values calculated according to the assumption of the IEC 61660: the effect of current limiters is neglected. This issue may lead to oversizing the ratings of protective devices and it should be discussed by the experts.

Chapter 6 Hierarchical-Power-Flow-Based Energy Management for Alternative/Direct Current Hybrid Microgrids

Abstract

Microgrids have become an efficient and reliable solution integrated into power grids, especially in low voltage ones, due to encompassing widely range of AC and DC systems such as Distributed Generations (DGs), Renewable Energy Sources (RESs), Battery Energy Storage System (BESS), AC/DC cables and loads, among others, that could operate in both grid-connected and islanded modes. Due to an increase in DC loads and penetration of RESs with DC power generation in the last decades, implementing hybrid AC/DC microgrids leads to have the advantages of both AC and DC subgrids simultaneously including a drop in power conversion and more reliable load supply while operating in islanded mode [128]. However, some challenges have emerged for this configuration, particularly related to control context, because of the presence of the coupling of AC and DC subgrids through converters [94, 129, 130].

This chapter aims to present a comprehensive hierarchically controlled power flow analysis for AC/DC hybrid microgrids in both grid-connected and islanded operating modes, considering the challenges above. For each operation mode, a centralized tertiary controller, as an energy management system, runs an optimization problem to calculate power generation, charging/discharging references for PVs, BESSs, and EVs. This could be mentioned as a drawback of the proposed control scheme, as a single point centralized unit leads to a decrease in reliability, and its failure results in a loss of power-sharing control for the entire system. Furthermore, this chapter studies the case of a real grid, as a part of a project named HYPERRIDE, that is going to be installed as a part of the Italian distribution power system with fully embedded RESs and flexible sources like BESS and Electrical Vehicles (EVs) stations in both AC and DC subgrids, whereas works discussed in the literature study in subsection 1.5.2 experimental test systems, and such a configuration with EV contribution has not been studied. The proposed model in this chapter incorporates a flexible primary controller for the converter integrated with BESS installed on the AC side, depending on the operating mode. In grid-connected mode, current reference control mode is adopted for DGs in both AC and DC grids, since the main grid is responsible to keep voltage and frequency at PCC bus.

Interlinking converter uses a frequency-voltage droop to calculate power reference for its corresponding AC/DC buses, and to exchange power between both subgrids, keeping DC link voltage close to its nominal value. In islanded mode, all converters remain with the same control mode, but the one connected to BESS in AC subgrid. Note that in previous studies, authors almost propose at least one voltage source converter (VSC) in AC and DC grids, making control schemes more complicated; however, in this study, the VSC connected to BESS in AC side generates voltage and frequency references at PCC bus using V-f droop control. This platform leads to have a simple and fast control scheme, while no need to change other converters' control mode. In addition, it is not necessary to adopt voltage and frequency restoration controllers as secondary one.

To have power reference for buses as schedule set points, power flow equations for both AC and DC subgrids are solved in a unified system using NR algorithm, which results in sufficiently fast convergence, as shown in the case study section. Finally, the results for mathematical model are validated by comparing against the professional simulation software MATLAB/ Simulink, approving the effectiveness and precision of the proposed model and control schemes.

This chapter focuses on studying power flow in hybrid microgrids, exclusively addressing steady-state operation for both grid-connected and islanded modes. Consequently, the transient period is not considered in this chapter. It is important to note that in transient studies, secondary voltage/frequency regulation becomes essential for rapid voltage restoration. As a result, the proposed model may not be deemed feasible or practical in transient states. Based on the identified research gaps in the literature and the novelty of this study, Table 6-1 represents comparison between existing literature and the proposed model.

Table 6-1. A comparison between the existing literature and the proposed model.

Ref.	Network type	Control scheme			Source/Load contribution			PF calculation	Daily load flow
		primary	secondary	tertiary	RES	BESS	EV		
[83]	AC	✓	✓	✓	✓	✓			✓
[85]	AC/DC	✓	✓					unified	
[86]	AC/DC	✓						unified	
[87]	AC/DC	✓						unified	
[88]	AC/DC	✓						sequential	
[131]	AC	✓							
[90]	AC/DC	✓			✓	✓	✓	sequential	
[91]	AC/DC	✓			✓	✓		unified	
[92]	AC	✓		✓					
[96]	AC/DC	✓		✓	✓	✓			
[97]	AC			✓	✓	✓			✓

[98]	AC/DC			✓	✓	✓			✓
[99]	AC/DC	✓		✓	✓	✓			✓
[100]	AC/DC	✓	✓		✓				
[102]	AC/DC							sequential	
[103]	AC/DC							unified	
[101]	AC/DC	✓						unified	
[104]	AC/DC	✓							
This chapter	AC/DC	✓		✓	✓	✓	✓	unified	✓

6.1 Hierarchically Controlled Optimal Power Flow in AC/DC Hybrid microgrids

In this section the proposed model and hierarchical control scheme is presented in detail. First, it is vital to recognize the proposed AC/DC hybrid microgrid and its elements. Therefore, Figure 6-1 shows an outlook of the system under study including electrical component, and controllers. In this hybrid structure, AC subgrid is connected to the main grid at PCC bus. AC and DC subgrids are connected through a bidirectional AC/DC IC. In each subsystem, there is a PV-Storage system and an EV charging/discharging station which are connected to the corresponding AC/DC buses by proper converters. Local AC and DC loads are located at PCC and DC link respectively, another AC load is supplied from DC subgrid through a DC/AC inverter, as well. In addition, Figure 6-1 depicts the proposed hierarchically controlled optimal power flow, which is explained in the following subsections.

6.1.1 Tertiary control

In the present work, tertiary control plays the role of the energy management system and is responsible for determining the hourly optimal power shares for the main grid (in grid-connected mode), PV systems, BESSs, and EV stations. The system also determines charging/discharging of storage systems and from EV stations, as well as the power exchange between AC and DC subgrids through IC, unlike the literature where changes in loads and RESs' output power over time are not addressed [83], or where only power exchange between microgrid and the main grid, along with charging/discharging for storage systems are considered [97-99]. Tertiary controller collects day-ahead data for AC and DC loads, output power for PV systems, and energy price, and characterizes an optimization problem, where the objective function is to minimize total cost for purchasing energy from the main grid in grid-connected mode, and load shedding in islanded mod. The references set given by the tertiary control are delivered to the converters local controllers using communication network, considered as scheduled power, as well, for power flow mismatch equations. Tertiary control's mathematical model and power flow equations are described in detail in section 6.3.

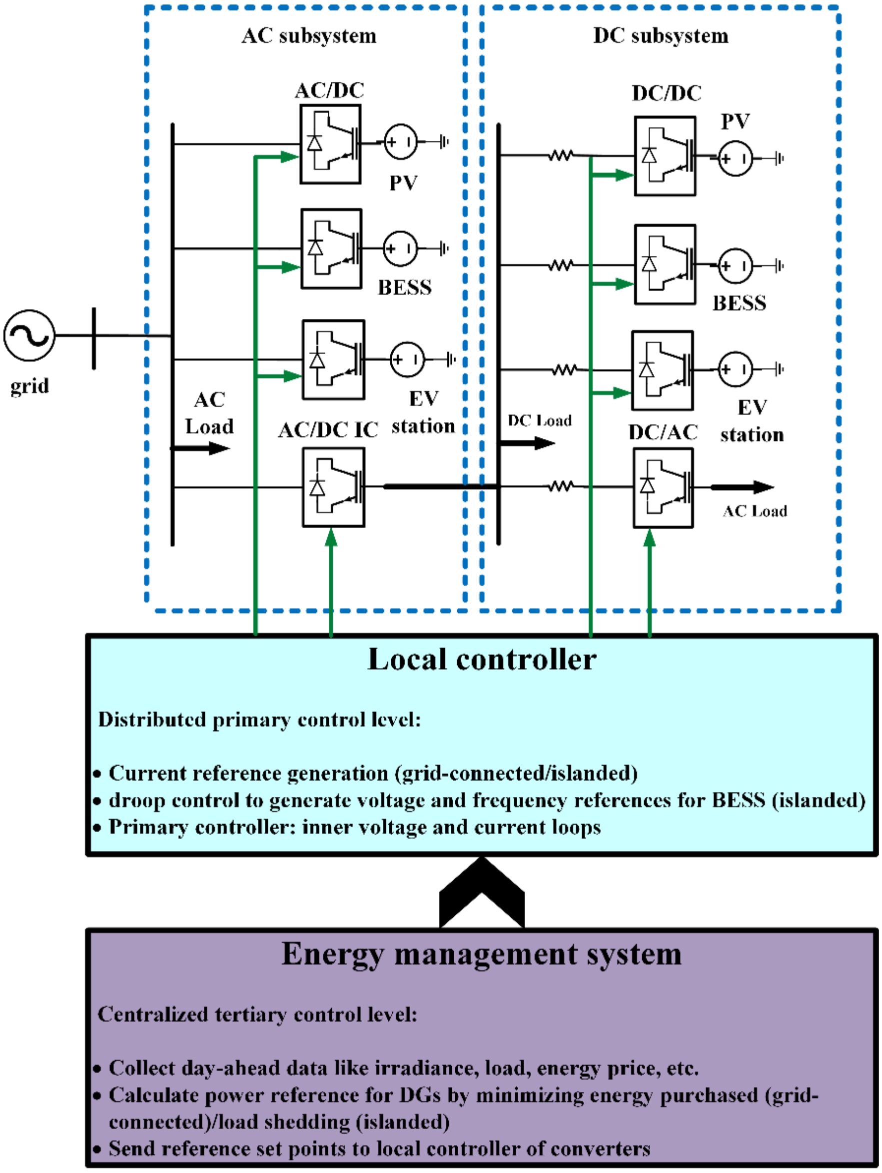

Figure 6-1. General Framework of the proposed hierarchically controlled optimal power flow.

6.1.2 Primary control

Power set points calculated in tertiary control level are delivered to the converter's local controller, including primary control level. As it is mentioned in the abstract of this chapter, in the proposed control scheme, there is no need to have voltage and frequency restoration at the PCC bus in the AC subgrid in both grid-connected and islanded modes as a secondary control level. In addition, since the interlinking converter controller uses a frequency/DC-voltage droop to supply the missing power to both subgrids, the DC link voltage is regulated autonomously and there is no need to control the DC bus voltage.

In grid-connected mode, voltage and frequency at PCC bus are regulated by the main grid. In this case, all RESs' converters, in both AC and DC subgrids, follow current control mode to generate reference powers [132]. Therefore, current reference generation, and inner voltage and current loops act as the primary controller. Note that, RESs generate power references, while the main grid supplies active and reactive powers close to its references (from the tertiary controller) to compensate power losses of the converters' filter and dc line resistances.

In islanded mode, all converters remain on the current control mode but that one is connected to the battery storage system in the AC subgrid being responsible to restore voltage and frequency at PCC through frequency/active power and voltage/reactive power droops as the primary controller [132]. BESS in AC subgrid projects like the main grid in grid-connected mode, keeping voltage and frequency respect to charging/discharging power reference values. For example, assuming a discharge operating mode, BESS tries to supply powers a little bit more than references to offset power losses, regulating voltage and frequency.

6.2 Hybrid Microgrid Control Scheme

This section presents control schemes for RESs converters and IC converters for AC and DC subgrids in both grid-connected and islanded operation modes. The following subsections depict these control specifications for AC and DC grids.

6.2.1 Grid-connected mode

In grid-connected operating mode, since the main grid keeps the AC subgrid voltage and frequency at their reference values and compensates the power losses of the lines and filters, all converters in both AC and DC subgrids conduct current reference control mode to generate a fixed power calculated in the tertiary control level as optimal power sharing. Hierarchical-based current control schemes for RESs in both AC and DC subgrids are illustrated in Figure 6-2 and Figure 6-3, respectively. For RESs' converters in AC subgrid (Figure 6-2), the three-phase inductor currents and voltages at the PCC are measured to be transformed into synchronous d-q frame using Park's transformation, and its angular position is generated and controlled through Phase Locked Loop (PLL) so that v_q component matches to zero [99], [132, 133]. Dynamic equations to calculate current references in d-q frame are as follows:

$$i_d^* = \frac{2P^*}{3v_d} \tag{6-1}$$

$$i_q^* = \frac{2Q^*}{3v_d} \tag{6-2}$$

where, P^* and Q^* are active and reactive power references, coming from the EMS and delivered to the primary local controller of the converters. Using these power references, equations (6-1) and (6-2) calculate current references in d-q frame. Finally, the inner current loop generates the voltage reference required for Pulse Width Modulation (PWM).

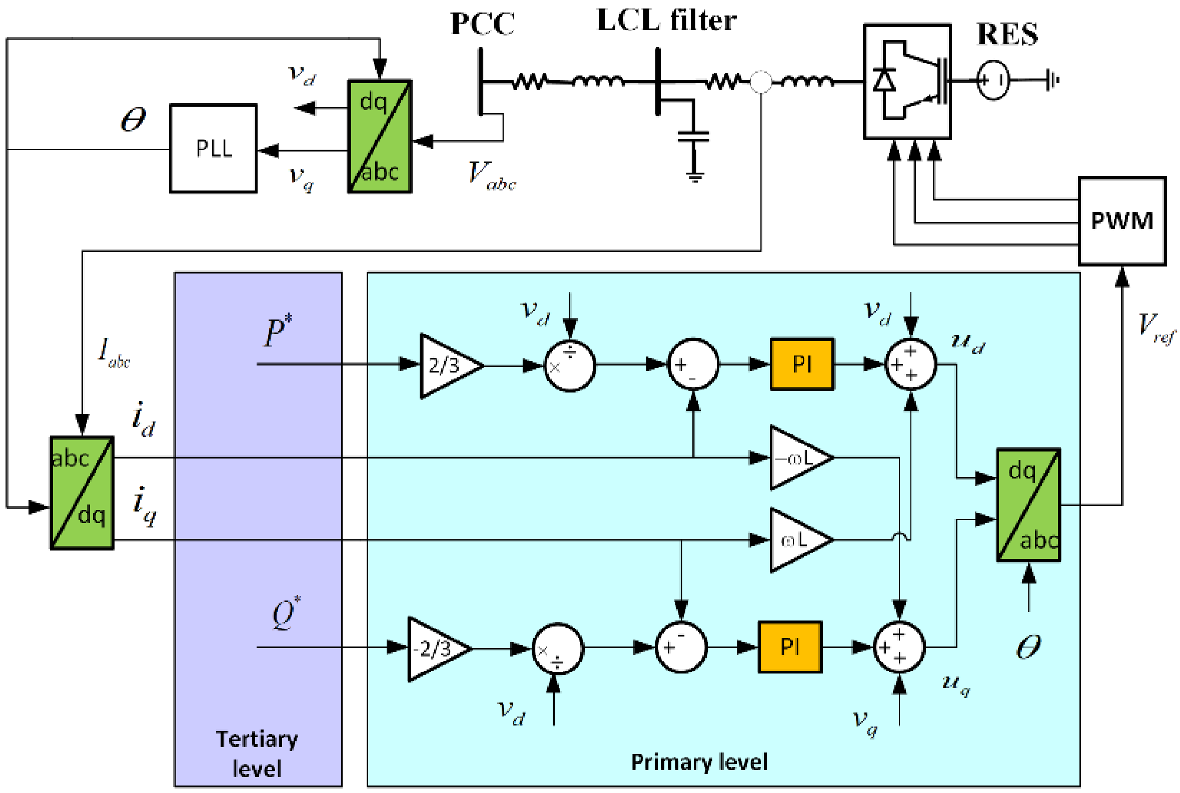

Figure 6-2. Hierarchical control scheme for RESs in AC subgrid.

In DC subgrid, however, battery storage system and electrical vehicles station are connected to the DC link through a bidirectional buck-boost converter and a line (represented as a resistance in Figure 6-3). Current control principle for DC/DC converters follows the same as that for AC/DC converters in the AC subgrid. P^* from the tertiary controller is transferred to the local controller. Then, using measured dc voltage of the battery, current reference is produced, followed by inner current loop as the primary control level to generate voltage reference. This voltage generates PWM signals, applying to buck-boost converters.

For a DC/DC boost converter connected to PV system, Figure 6-4 depicts the control block diagram for both grid-connected and islanded operation modes since they follow almost similar structure. In islanded mode, microgrid needs to use maximum output power of PV system to implement minimum load shedding. Therefore, in optimization process (tertiary level), a fixed PV output power (P_i^*) is taken into account for each hour depending on irradiance and goes to perturb and observe maximum power point tracking (P&O-MPPT) algorithm. However, in grid-connected mode, optimization program might choose PV output power lower than maximum available power. By this case, boost converter is going to generate P_g^* using P&O constant power generation (P&O-CPG), see Figure 6-4. In this algorithm, the PV output voltage is continuously perturbed away from the maximum power point in the CPG operation mode in order to match the PV output power according to the set point. Readers may refer to [117, 118] to have a deeper understanding of CPG control mode in PV system. In both cases, finally, an inner voltage loop is conducted to generate PWM signals.

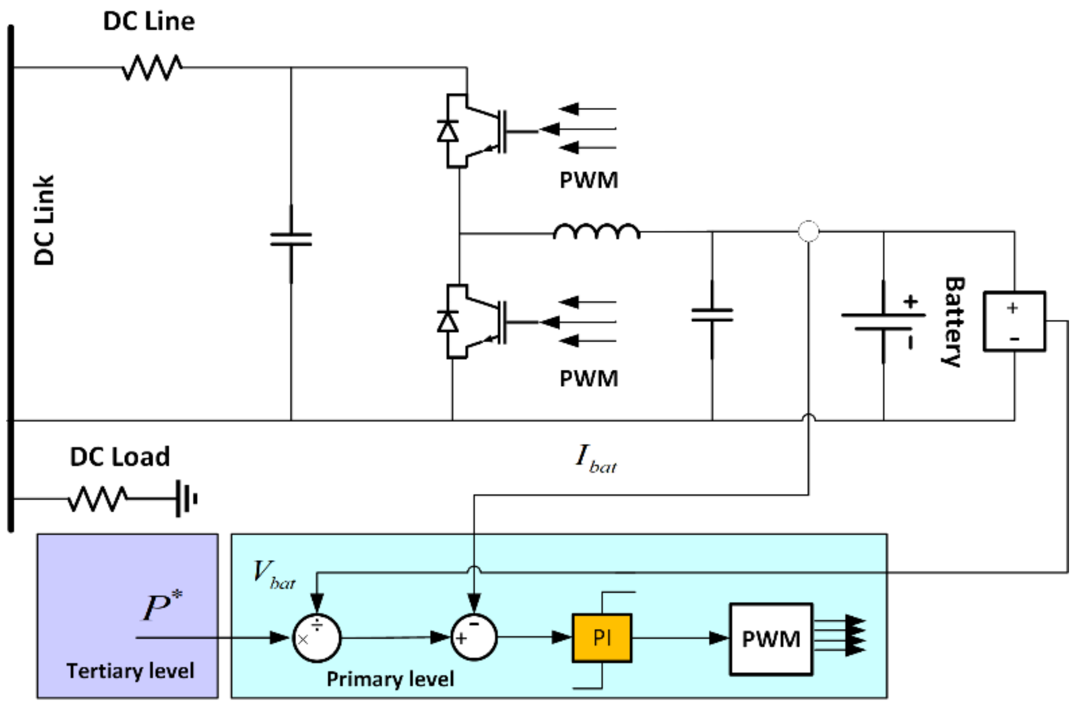

Figure 6-3. Hierarchical control scheme for BESS ad EV station in DC subgrid.

The Interlinking Converter (IC) is the most important component in hybrid grids to share power between both AC and DC subgrids. A properly controlled IC leads to a stable and robust power exchange between AC and DC subgrids. According to the power references characterized by the tertiary controller, if total output power of the RESs in DC grid is not sufficient to supply DC local load, IC transfer power shortage from AC to DC grid to keep DC link voltage close to the nominal value, and vice versa delivers surplus DC active power to AC grid to keep frequency at PCC. Therefore, in this chapter a well-known $P/\omega_{pu} - V_{pu}^{dc}$ droop control is conducted and shown in Figure 6-5 (a), meaning IC shares active power based on the difference between frequency at PCC and DC link voltage [85, 94, 132]. This active power is purposed as scheduled active power in mismatch equations in NR algorithm, and calculated as follows:

$$P^* = \frac{\omega_{pu} - V_{pu}^{dc}}{K_{ic}^{p}} \qquad (6\text{-}3)$$

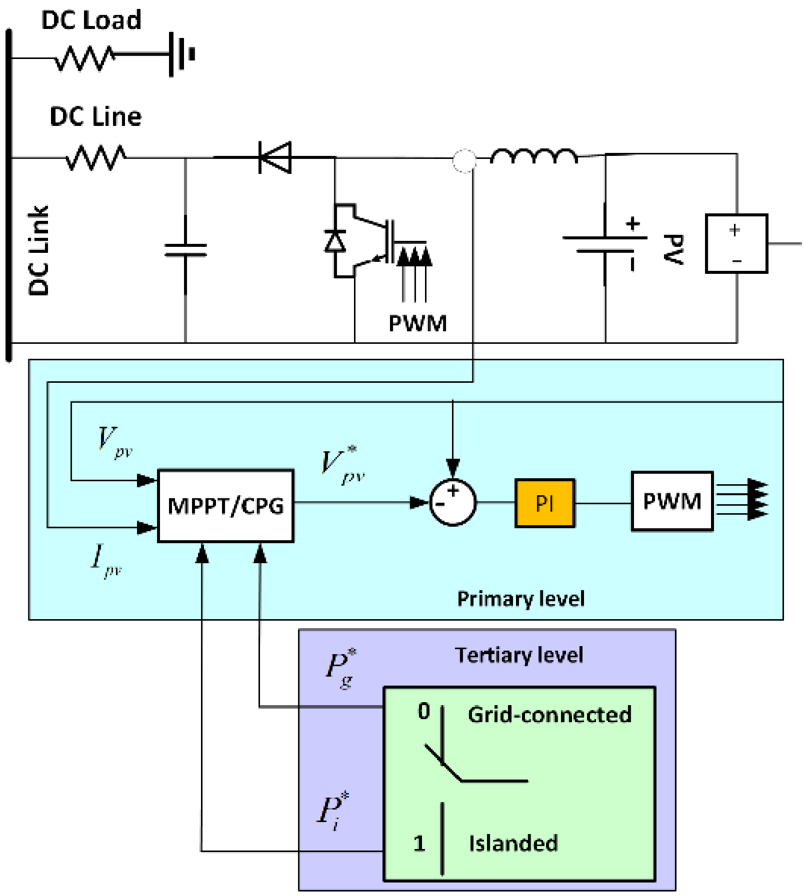

Figure 6-4. Hierarchical control scheme for DC-side PV system in grid-connected and islanded modes.

where, ω_{pu} and V_{pu}^{dc} are normalized (per unit) measured frequency at PCC and dc link voltage, respectively, to be comparable, and calculated as:

$$\omega_{pu} = \frac{\omega - \omega^*}{0.5(\omega^{max} - \omega^{min})} \quad (6\text{-}4)$$

$$V_{pu}^{dc} = \frac{V_{dc} - V_{dc}^*}{0.5(V_{dc}^{max} - V_{dc}^{min})} \quad (6\text{-}5)$$

According to Figure 6-5 (a) and equation (6-3), whenever per unit frequency is greater than the per unit DC link voltage, active power is delivered to the DC grid to compensate deficient available power there, and inversely, lower frequency at PCC due to power shortage makes IC to transfer surplus DC active power from DC side to AC one. Note that the reference set-point for the reactive power is calculated in the optimization process, done by the tertiary level controller. It is worth to mention that, only if there is power sharing from DC to AC side, IC may deliver reactive power to AC grid [132]. Figure 6-5 (b) illustrates the hierarchical control block diagram that is the same as that for RESs' controllers in AC side (Figure 6-2), but active power reference is coming from equation (6-3).

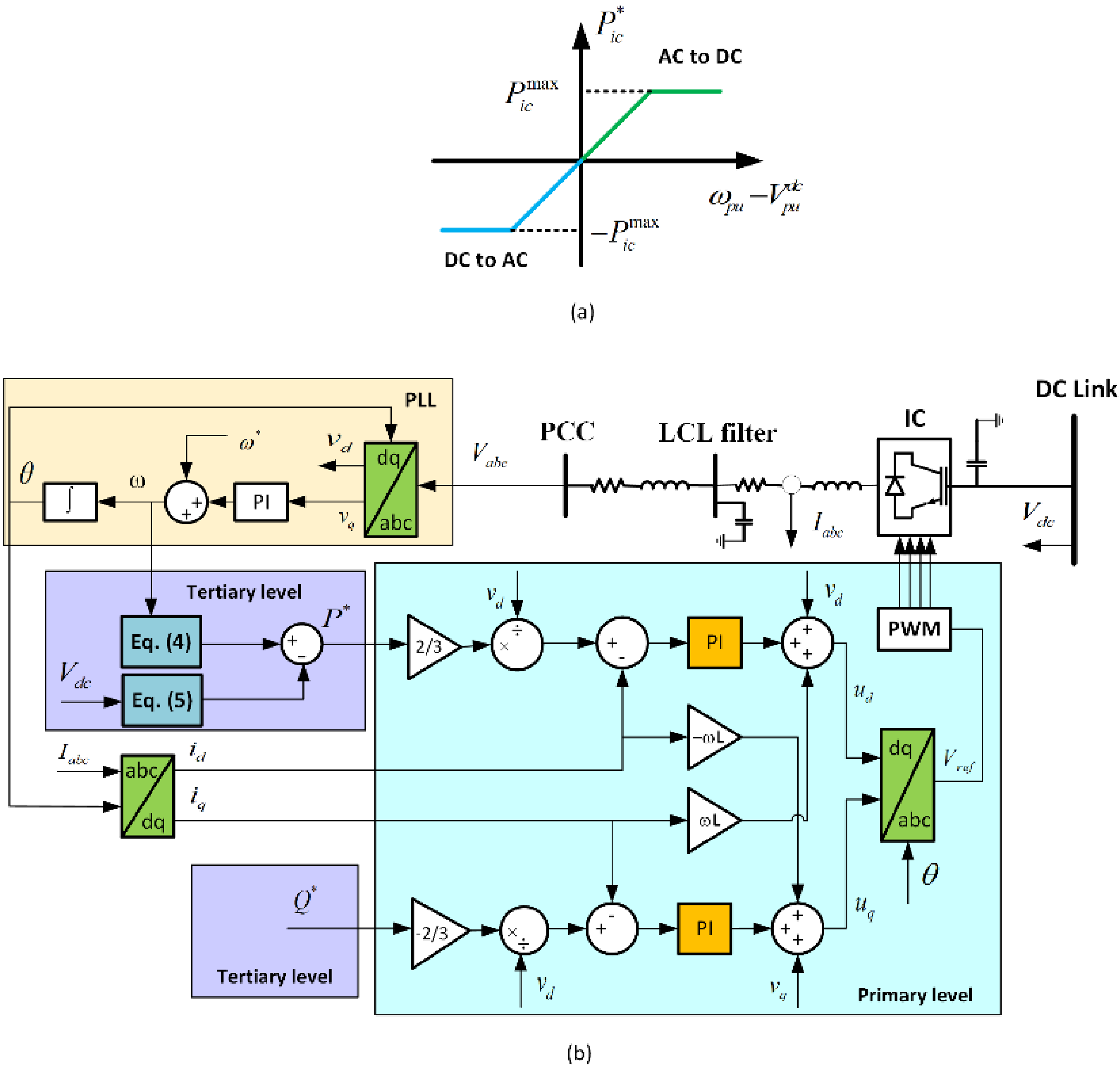

Figure 6-5. (a): IC droop control for active power sharing, (b): Hierarchical control scheme for IC.

6.2.2 Islanded mode

As it is discussed in the abstract of this chapter, this study proposes that, in the islanded mode, the control scheme of all converters remain the same as in grid-connected mode with the exception of that connected to BESS in AC subgrid. Since PV system and EVs are not able to generate energy for a 24-hours day, BESS need to change its control mode to voltage control mode [134] as depicted in Figure 6-6. Active and reactive power are calculated and compared to references values coming from the upper level, which could be positive or negative dependent on charging/discharging operation modes. Then, a droop-based primary controller is applied to generate reference voltage and angular frequency. Then, using these values, inner voltage and current loops generate PWM pulses for the converter. In fact, this control scheme aims to keep voltage and frequency at PCC, while trying to follow power references. In other word, when storage system operates in discharging state, it may generate active and reactive power a little more than reference values and consumes a little lower than reference active power in charging mode. In fact, this difference is due to power losses compensation by storage system to hold nominal voltage and frequency at PCC.

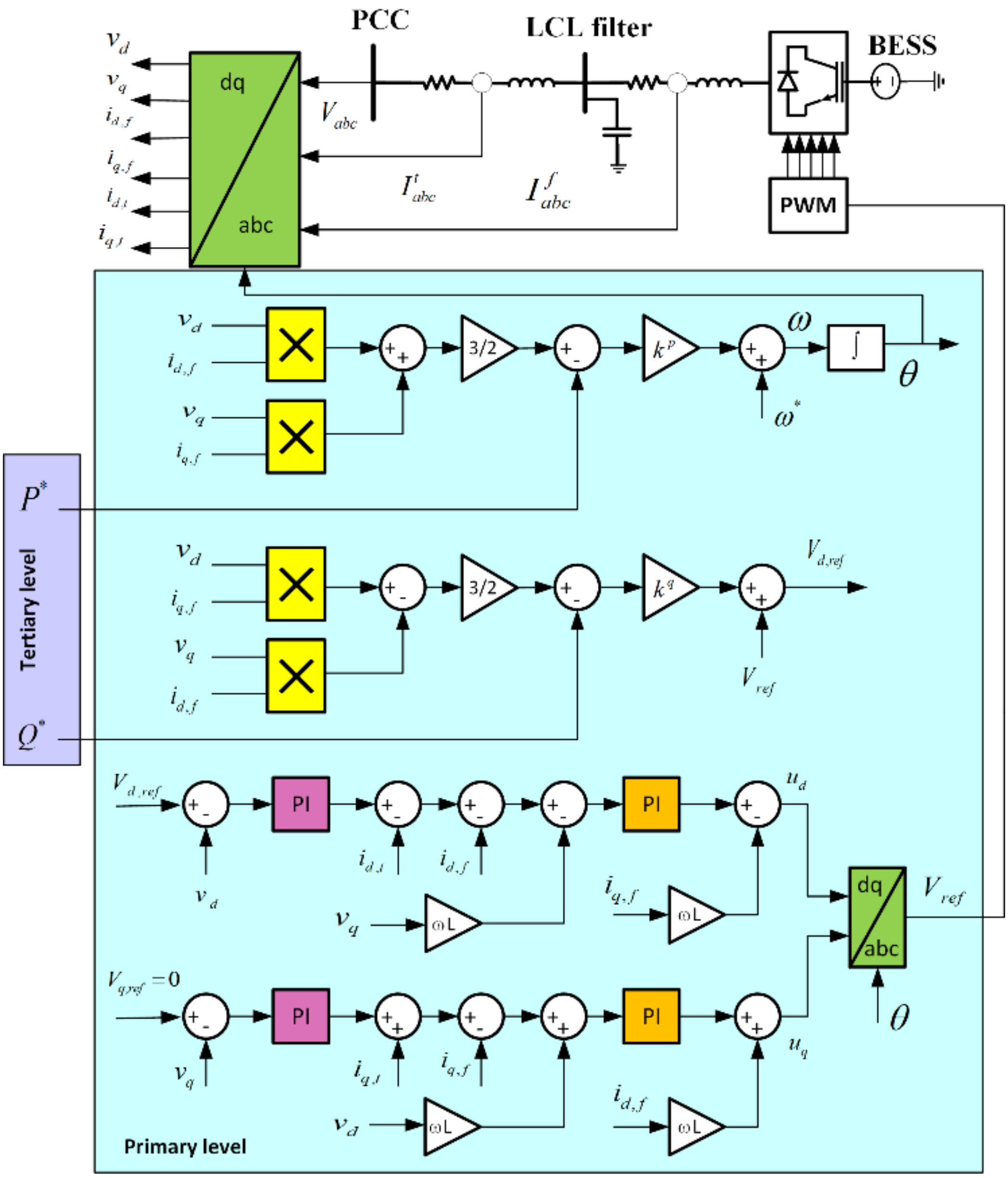

Figure 6-6. Hierarchical control scheme for AC-side BESS in islanded mode.

6.3 Tertiary Level and Power Flow Formulation

In this section, the tertiary control level, that is an optimization program, and the Newton-Raphson power flow equations are mathematically modeled for both AC and DC subgrids in grid-connected and islanded operating modes. Although the proposed model is formulated in general for any AC/DC power grid outline, readers may refer to Figure 6-1, as it presents the same system used in the case study (single-line diagram is shown in section 6.4), to better understand the concept of the mathematic model. The two first following subsections describe and formulate the daily optimal load sharing for both operation modes, then unified AC/DC NR power flow equations are solved integrating scheduled powers from the optimization, and the control scheme for the interlinking converter.

6.3.1 Grid-connected mode

In grid-tied operation mode, the aim of tertiary control level, which plays an EMS, is to determine power generation references for RESs along with charging/discharging states for batteries of BESSs and EVs each hour, meanwhile minimizing the total cost of the power purchasing from the main grid. In this scenario, all RESs follow current control mode to generate the reference powers, and PV system switches to constant power generation mode (position "0" for the switch in Figure 6-4) that implies it might generate power lower than maximum power each hour. So, if all RESs in both subgrids follow their power set-points, the main grid also deliver power to the microgrid as much as calculated from the optimization program. Therefore, the objective function is:

$$C_T = \sum_{t=1}^{24} c_g(t).(P_g(t) + Q_g(t)) \qquad (6\text{-}6)$$

From equation (6-6), it is worth noting that, although energy price is often based on active power, utilities sometimes charge customers for a poor power factor. In addition, PV and storage system on the AC subsystem may inject reactive power into the microgrid. Therefore, importing reactive power from the main grid is considered as a penalty in this article.

Constraints are categorized into two types including load sharing-related and battery-oriented ones. Equations and inequalities (6-7) to (6-17) represent the first category. Equations (6-7) to (6-9) represent active and reactive power balance. For active power, there are two sets of power balance equations meaning equation (6-7) and equation (6-8) depending on the direction IC transmit active power. In the first set, it is from AC to DC implying IC is a load for AC subgrid, meanwhile playing a role as a source for DC subgrid. Unlike the first equations set, in the second set, characterized in (6-8), IC is a load for DC side, while a source for AC one. To mathematically model this aspect in optimization process, a very large number M and an integer variable I_{ic} for the direction of active power sharing for IC are defined. If program makes IC to send active power from AC to DC, I_{ic} would be 1, equations in (6-7) must be zero and those in (6-8) are free. Inversely, when optimization prefers to transmit active power from DC to AC side, I_{ic} would be 0, equations in (6-8) are chosen, and those in (6-7) are relax.

$$\begin{cases} P_{ac}^{pv}(t)+P_g(t)+P_{dis}^{s,ac}(t)+P_{dis}^{e,ac}(t)-P_{ch}^{s,ac}(t)-P_{ch}^{e,ac}(t)-P_l^{ac}(t)-P_{ic}(t)\geq -M(1-I_{ic}(t)) \\ P_{ac}^{pv}(t)+P_g(t)+P_{dis}^{s,ac}(t)+P_{dis}^{e,ac}(t)-P_{ch}^{s,ac}(t)-P_{ch}^{e,ac}(t)-P_l^{ac}(t)-P_{ic}(t)\leq M\big(1-I_{ic}(t)\big) \\ P_{dc}^{pv}(t)+P_{dis}^{s,dc}(t)+P_{dis}^{e,dc}(t)+P_{ic}(t)-P_{ch}^{s,dc}(t)-P_{ch}^{e,dc}(t)-P_l^{dc}(t)\geq -M\big(1-I_{ic}(t)\big) \\ P_{dc}^{pv}(t)+P_{dis}^{s,dc}(t)+P_{dis}^{e,dc}(t)+P_{ic}(t)-P_{ch}^{s,dc}(t)-P_{ch}^{e,dc}(t)-P_l^{dc}(t)M\big(1-I_{ic}(t)\big) \qquad \forall t \end{cases} \tag{6-7}$$

$$\begin{cases} P_{ac}^{pv}(t)+P_g(t)+P_{dis}^{s,ac}(t)+P_{dis}^{e,ac}(t)+P_{ic}(t)-P_{ch}^{s,ac}(t)-P_{ch}^{e,ac}(t)-P_l^{ac}(t)\geq -M.I_{ic}(t) \\ P_{ac}^{pv}(t)+P_g(t)+P_{dis}^{s,ac}(t)+P_{dis}^{e,ac}(t)+P_{ic}(t)-P_{ch}^{s,ac}(t)-P_{ch}^{e,ac}(t)-P_l^{ac}(t)\leq M.I_{ic}(t) \\ P_{dc}^{pv}(t)+P_{dis}^{s,dc}(t)+P_{dis}^{e,dc}(t)-P_{ic}(t)-P_{ch}^{s,dc}(t)-P_{ch}^{e,dc}(t)-P_l^{dc}(t)\geq -M.I_{ic}(t) \\ P_{dc}^{pv}(t)+P_{dis}^{s,dc}(t)+P_{dis}^{e,dc}(t)-P_{ic}(t)-P_{ch}^{s,dc}(t)-P_{ch}^{e,dc}(t)-P_l^{dc}(t)\geq -M.I_{ic}(t) \qquad \forall t \end{cases} \tag{6-8}$$

$$Q_{ac}^{pv}(t)+Q_g(t)+Q_{ac}^{s}(t)+Q_{ac}^{ev}(t)+Q_{ic}(t)=Q_l^{ac}(t) \qquad \forall t \tag{6-9}$$

$$P_g(t)\leq P_g^{max} \qquad \forall t \tag{6-10}$$

$$P_{ac/dc}^{pv}(t)\leq P_{max}^{pv} \qquad \forall t \tag{6-11}$$

$$P_{ic}(t)\leq P_{ic}^{max} \qquad \forall t \tag{6-12}$$

$$Q_g(t)\leq Q_g^{max} \qquad \forall t \tag{6-13}$$

$$Q_{ac}^{pv}(t)\leq \sqrt{S_{pv}^2-P_{ac}^{pv}(t)^2} \qquad \forall t \tag{6-14}$$

$$Q_{ac}^{s}(t)\leq I_{dis}^{s,ac}(t).\sqrt{S_s^2-P_{dis}^{s,ac}(t)^2} \qquad \forall t \tag{6-15}$$

$$Q_{ac}^{ev}(t)\leq I_{dis}^{e,ac}(t).\sqrt{S_e^2-P_{dis}^{e,ac}(t)^2} \qquad \forall t \tag{6-16}$$

$$Q_{ic}(t)\leq (1-I_{ic}(t)).\sqrt{S_{ic}^2-P_{ic}(t)^2} \qquad \forall t \tag{6-17}$$

Inequality constraints (6-10) to (6-12) restrict active power for the main grid, PV system, and IC to their capacities. Equations (6-13) to (6-17) are reactive power constraints for the utility, PV system, battery-based sources, and IC that explain injected reactive power by converters can follow their reference values as long as they do not exceed corresponding capacity [87, 88, 128]. Note here, for BESS and EV parking lot, reactive power could be injected to the microgrid only if it is in the discharging mode; and for IC, only if power is transmitted from DC to AC subgrid. Since this chapter projects to solve a linear optimization problem, equations (6-14) to (6-17) need to be removed from the optimization process. To handle this problem, MATLAB and GAMS applications are linked so that data are transported from the former to the latter. Then GAMS is run, and optimal results are sent back to MATLAB to check converters reactive power constraint for the converters. There, if reactive power value exceeds its limit, converter switches to PQ mode and keep its reactive power upper limit as a new reference. At the end of this section, the interlinking process between MATLAB and GAMS is outlined. The same optimization algorithm constraints are already used in Chapter 2 and Chapter 3 [135, 136].

Following equations characterize constraints for batteries in BESS and EV station. Inequalities (6-18) to (6-25) imply charging/discharging power for the batteries of BESS and EV station in both AC and DC subgrids could not be exceed the corresponding upper and lower limits. Subsequently, (6-26) to (6-29) represent that charging and discharging of these batteries might not be done simultaneously through integer variables. Energy available of these sources at each hour are calculated and restricted by (6-30) to (6-35). It is vital to consider EVs' batteries are not able to charge or discharge as long as they are out of the lot which are represented in (6-36) and (6-37). Finally, constraint (6-38) makes the optimization program to keep a threshold energy at EVs' batteries at the time they leave the lot.

$$I_{dis}^{s,ac}(t).P_{dis}^{s,min} \le P_{dis}^{s,ac}(t) \le I_{dis}^{s,ac}(t).P_{dis}^{s,max} \qquad \forall t \tag{6-18}$$

$$I_{ch}^{s,ac}(t).P_{ch}^{s,min} \le P_{ch}^{s,ac}(t) \le I_{ch}^{s,ac}(t).P_{ch}^{s,max} \qquad \forall t \tag{6-19}$$

$$I_{dis}^{s,dc}(t).P_{dis}^{s,min} \le P_{dis}^{s,dc}(t) \le I_{dis}^{s,dc}(t).P_{dis}^{s,max} \qquad \forall t \tag{6-20}$$

$$I_{ch}^{s,dc}(t).P_{ch}^{s,min} \le P_{ch}^{s,dc}(t) \le I_{ch}^{s,dc}(t).P_{ch}^{s,max} \qquad \forall t \tag{6-21}$$

$$I_{dis}^{e,ac}(t).P_{dis}^{e,min} \le P_{dis}^{e,ac}(t) \le I_{dis}^{e,ac}(t).P_{dis}^{e,max} \qquad \forall t \tag{6-22}$$

$$I_{ch}^{e,ac}(t).P_{ch}^{e,min} \le P_{ch}^{e,ac}(t) \le I_{ch}^{e,ac}(t).P_{ch}^{e,max} \qquad \forall t \tag{6-23}$$

$$I_{dis}^{e,dc}(t).P_{dis}^{e,min} \le P_{dis}^{e,dc}(t) \le I_{dis}^{e,dc}(t).P_{dis}^{e,max} \qquad \forall t \tag{6-24}$$

$$I_{ch}^{e,dc}(t).P_{ch}^{e,min} \le P_{ch}^{e,dc}(t) \le I_{ch}^{e,dc}(t).P_{ch}^{e,max} \qquad \forall t \tag{6-25}$$

$$I_{dis}^{s,ac}(t) + I_{ch}^{s,ac}(t) \le 1 \qquad \forall t \tag{6-26}$$

$$I_{dis}^{s,dc}(t) + I_{ch}^{s,dc}(t) \leq 1 \qquad \forall t \tag{6-27}$$

$$I_{dis}^{e,ac}(t) + I_{ch}^{e,ac}(t) \leq 1 \qquad \forall t \tag{6-28}$$

$$I_{dis}^{e,dc}(t) + I_{ch}^{e,dc}(t) \leq 1 \qquad \forall t \tag{6-29}$$

$$E_{ac/dc}^{s}(t) = E_{ac/dc}^{s}(t-1) + Q.P_{ch}^{s,ac/dc}(t) - P_{dis}^{s,ac/dc}(t)/Q \qquad \forall t > 1 \tag{6-30}$$

$$E_{ac/dc}^{s}(t) = U_{ac/dc}^{s}(0) + Q.P_{ch}^{s,ac/dc}(t) - P_{dis}^{s,ac/dc}(t)/Q \qquad \forall t < 2 \tag{6-31}$$

$$E_{s}^{min} \leq E_{ac/dc}^{s}(t) \leq E_{s}^{max} \qquad \forall t \tag{6-32}$$

$$E_{ac/dc}^{e}(t) = E_{ac/dc}^{e}(t-1) + Q.P_{ch}^{e,ac/dc}(t) - P_{dis}^{e,ac/dc}(t)/Q \qquad \forall t > 1 \tag{6-33}$$

$$E_{ac/dc}^{e}(t) = U_{ac/dc}^{e}(0) + Q.P_{ch}^{e,ac/dc}(t) - P_{dis}^{e,ac/dc}(t)/Q \qquad \forall t < 2 \tag{6-34}$$

$$E_{e}^{min} \leq E_{ac/dc}^{e}(t) \leq E_{e}^{max} \qquad \forall t \tag{6-35}$$

$$P_{dis}^{e,ac/dc}(t) = 0 \qquad \forall t \in T_{out} \tag{6-36}$$

$$P_{ch}^{e,ac/dc}(t) = 0 \qquad \forall t \in T_{out} \tag{6-37}$$

$$E_{ac/dc}^{e}(t_l) \geq N.\lambda.D \qquad \forall t \tag{6-38}$$

6.3.2 Islanded mode

Microgrids could be disconnected from the main grid at PCC, in this case, hybrid microgrid needs to operate autonomously. Assuming there might not be sufficient available energy from generators to supply all loads at specific hours, operators must conduct a proper load shedding to implement a stable and reliable operation. Therefore, in islanded mode, the objective function of the tertiary level controller is minimizing total load shedding rates as:

$$L_{T}^{sh} = \sum_{t=1}^{24} \gamma^{ac}(t).\left(P_{l}^{ac}(t) + Q_{l}^{ac}(t)\right) + \gamma^{dc}(t).P_{l}^{dc}(t) \qquad \forall t \tag{6-39}$$

Constraints in this scenario are like those for grid-connected mode but there is no more power from the main grid. In addition, to minimize the load shedding rates, converters connected to PV systems operate in MPPT control mode. Load demand in power balance set equations is modified as follows:

$$\begin{cases} P_{l,i}^{ac}(t) = \left(1 - \gamma^{ac}(t)\right).P_l^{ac}(t) \\ Q_{l,i}^{ac}(t) = \left(1 - \gamma^{ac}(t)\right).Q_l^{ac}(t) \\ P_{l,i}^{dc}(t) = \left(1 - \gamma^{dc}(t)\right).P_l^{dc}(t) \qquad \forall t \end{cases} \tag{6-40}$$

6.3.3 NR power flow problem

To model NR power flow analysis in AC grids, buses need to be defined as one of the three types of buses including slack bus with voltage magnitude and phase angle are 1 and 0 respectively, which here it is the bus connected to the main grid in grid connected mode, *PV* buses with fixed active power generation and voltage magnitude, and the last type is *PQ* or load buses with scheduled active and reactive power. In this chapter, all converter buses are referred as load ones where schedule powers come from the tertiary level, and PCC bus and DC link are load buses connecting to AC and DC loads, and corresponding AC system frequency and voltage are regulated by the main grid. For a bus in AC subsystem, the injected active and reactive power are calculated as follows:

$$P_n^{ac} = |V_n|^2 G(n,n) + \sum_{\substack{j\in\Omega_{ac} \\ j\neq n}} [|V_n||V_m| G(n,m)\cos(\delta_n - \delta_m) + |V_n||V_m| B(n,m)\sin(\delta_n - \delta_m)] \qquad \forall t \tag{6-41}$$

$$Q_n^{ac} = -|V_n|^2 B(n,n) + \sum_{\substack{j\in\Omega_{ac} \\ j\neq n}} [|V_n||V_m| G(n,m)\sin(\delta_n - \delta_m) - |V_n||V_m| B(n,m)\cos(\delta_n - \delta_m)] \qquad \forall t \tag{6-42}$$

where n and m represent the different buses of the AC system, and G *and* B are respectively conductance and susceptance of the admittance matrix. In DC subgrid, however, there are only two categories for buses: P/load bus or V bus with fixed voltage magnitude. Due to the lack of frequency in DC grid, formulation for calculated active power is the following equation where admittance matrix has only conductance part g.

$$P_n^{dc} = |V_n|^2 g(n,n) + \sum_{\substack{j\in\Omega_{dc} \\ j\neq n}} |V_n||V_m| g(n,m) \qquad \forall t \tag{6-43}$$

Expanding (6-41) to (6-43) in Taylor's series about the initial estimate and neglecting all higher order terms, a set of linear equations as follows is extracted to calculate the difference between calculated and scheduled power and solved iteratively.

$$\begin{bmatrix} \Delta P^{ac} \\ \Delta Q^{ac} \\ \Delta P^{dc} \end{bmatrix} = \begin{bmatrix} \frac{\partial P^{ac}}{\partial \delta} & \frac{\partial P^{ac}}{\partial |V_{ac}|} & \frac{\partial P^{ac}}{\partial V_{dc}} \\ \frac{\partial Q^{ac}}{\partial \delta} & \frac{\partial Q^{ac}}{\partial |V_{ac}|} & \frac{\partial Q^{ac}}{\partial V_{dc}} \\ \frac{\partial P^{dc}}{\partial \delta} & \frac{\partial P^{dc}}{\partial |V_{ac}|} & \frac{\partial P^{dc}}{\partial V_{dc}} \end{bmatrix} \begin{bmatrix} \Delta \delta \\ \Delta |V_{ac}| \\ \Delta V_{dc} \end{bmatrix} \tag{ 6-44}$$

Note that for the AC bus connected to IC, scheduled active power is calculated by equation (6-3), which is the same for DC bus connected to IC with opposite sign since power losses in IC is neglected. For the case that active power is injected to DC grid, this calculated active power is considered as a generation power for DC link, and, inversely, it adds to the DC load when power is transferred from DC to AC grid. Reactive power for the AC bus connected to IC, however, comes from the optimization program. The interlinking process between MATLAB and GAMS is illustrated in Figure 6-7. Initially, data is loaded into MATLAB, followed by its transfer to GAMS. The tertiary level is addressed using Mixed Integer Linear Programming (MILP) via GAMS Cplex solver, then the optimal load sharing results, including scheduled active and reactive powers for all resources, are sent back from GAMS to MATLAB, where power flow problem is solved. Before solving PF, MATLAB checks the non-linear constraints (6-14) to (6-17) in each power flow iteration. By doing this, there is no need to run a non-linear optimization in GAMS, as PF is inherently a non-linear problem. If the reactive power value exceeds its limit, converter switches to PQ mode and keep its reactive power upper limit as a new reference. Then, new data is sent again to GAMS to solve a new optimization problem.

6.4 Case Study Analysis

Figure 6-8 shows an 11-bus AC/DC hybrid microgrid that is going to be installed for Italian pilot as a part of a project named HYPERRIDE. This microgrid is a part of Italian distribution system where is connected to the distribution station ASM at PCC (bus #2) through line 1 at 400 V, while $\pm$ 700 V DC lines are constructed in DC subgrid. In both AC and DC sides, there are PV systems as RESs, and the base apparent power is 100 kVA. In addition, flexible resources such as BESSs and EV stations are available in both subgrids. AC/DC converters are connected to the PCC bus through LCL filter, meanwhile DC ones are connected to the DC link (bus #7) via dc resistances [137]. IC couples both subgrids to share powers between them and help DC link voltage regulation in both operation modes. In islanded operating mode, the IC is also projected to transfer power between both AC and DC subgrids to guarantee power balance, where AC voltage and frequency restoration is reached.

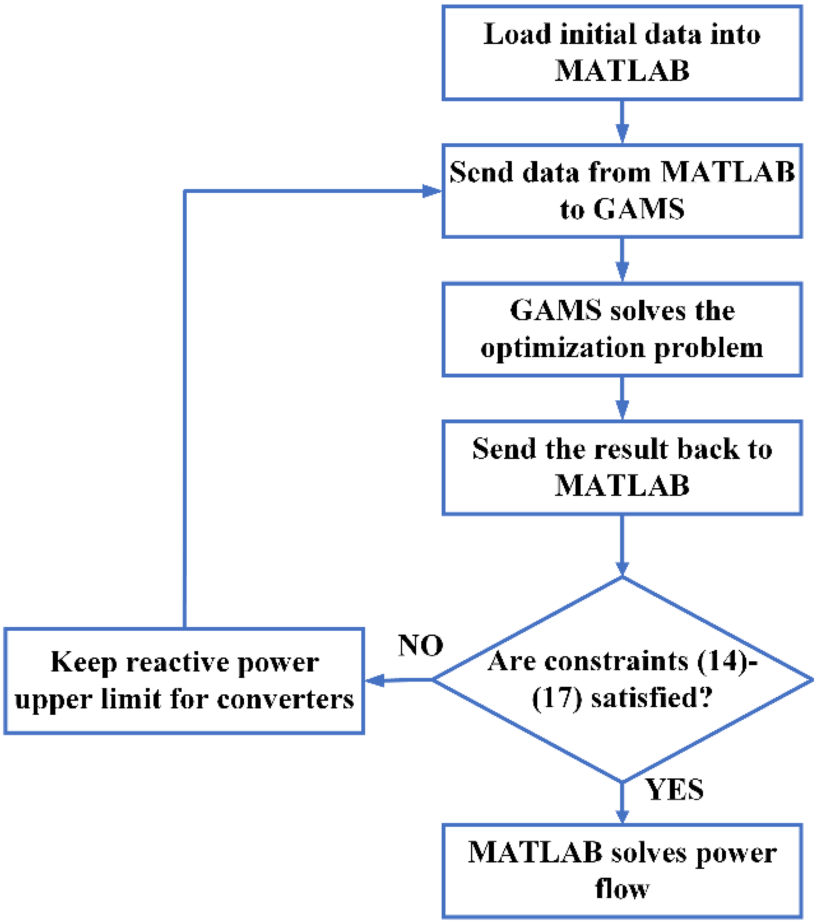

Figure 6-7. The interlinking process between MATLAB and GAMS.

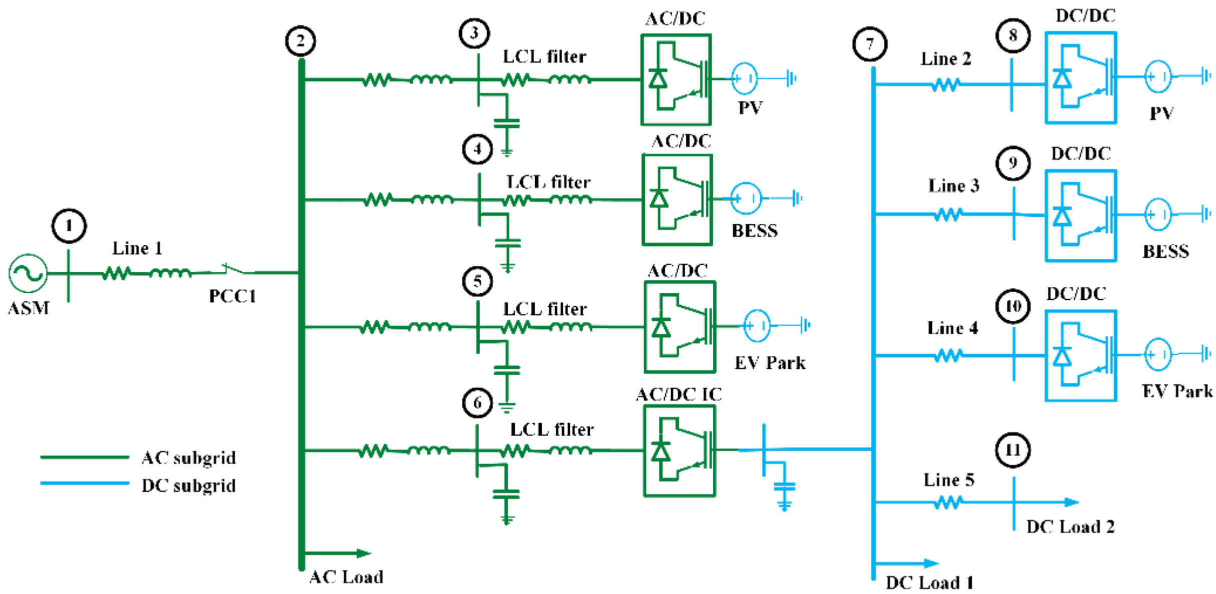

Figure 6-8. Terni AC/DC hybrid microgrid: Italian Pilot.

Since this microgrid has not been operated yet, hourly load data, irradiance to calculate PV output power, and EVs data are not available; therefore, corresponding data for another part of

Italian distribution systems are used referring to the database from ARERA, the Italian Regulatory Authority for Energy, Networks and the Environment providing the most recent technical reports on the energy transition in Europe and Italy [106-110]. This problem does not reduce the effectiveness and application of this work because a general and robust model has been proposed that may be conducted to any hybrid systems. The pattern for load consumption, and maximum generation of PV systems in a 24-hours day in April for the proposed case study are illustrated in Figure 6-9, where these values are in per unit (p.u.) system. However, the capacity of converters connected to PV, BESS, and EV station systems, and peak loads consumption have been designed and reported in [137] and presented at Table 6-2. In AC and DC subgrids, there is a small-scale parking lots for EVs each including five mid-size sedans with 10 kWh battery capacity, means that maximum available energy at each lot is 50 kWh. It is assumed that charging station is a fast charge type so that each EV could be fully recharged by one hour; therefore, maximum charge/discharge power is 50 kW at each time interval. In this chapter, the efficiency of converters in BESSs and EV parking lots is 95%.

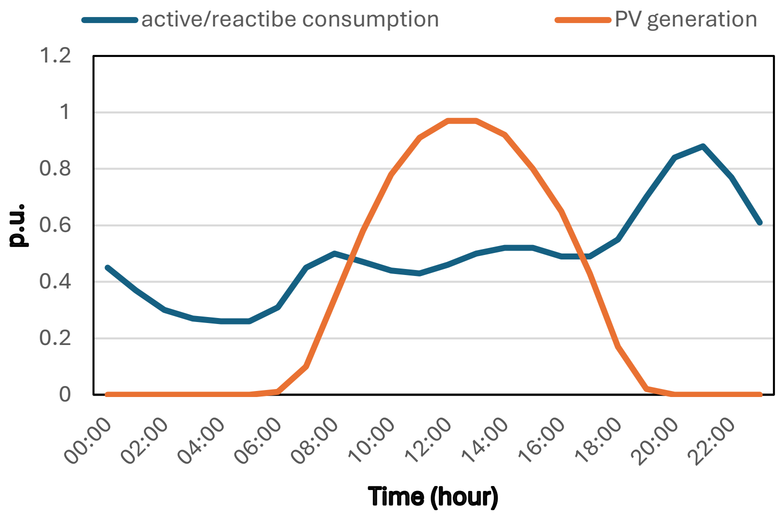

Figure 6-9. Hourly load demand and PV generation in p.u.

Table 6-2. Capacity of the resources and load demand in AC and DC subgrids.

subgrid	PV [kW]	BESS [kWh]	EV station [kWh]	Load [kW/kVar]
AC	10	50	50	30/10
DC	5	50	50	Load #1 → 20 Load #2 → 25

Energy price is one of the most noticeable parameters that could affect considerably the pattern of charging/discharging of the flexible resources, power purchased from the main grid, and finally power generated by the RESs and power flow calculations. In addition, it is clear that this parameter varies depending on the weekdays and the time a day. Therefore, taking a realistic energy price into account leads to improvement of the analysis. Table 6-3 represents the energy price for different days and hours in the Italian market in 2023.

Table 6-3. Energy price in Italian case study.

weekdays	Time (hour)	Price (€/kWh)
Monday-Friday	23:00-7:00	0.4121
Monday-Friday	7:00-8:00	0.4955
Monday-Friday	8:00-19:00	0.4417
Monday-Friday	19:00-23:00	0.4955

To conduct a more close-to-real model for EVs, many authors have implemented stochastic approaches like Monte Carlo Simulation (MCS) to characterize the pattern of leaving and arriving time at lots, and journey distance each day. These models are practical for the cases with a lot of EVs, while there is only a small fleet with five EVs. On the other hand, since it is aimed to calculate daily power flow considering the buses connected to EVs stations as load ones, it is required to have an active and a reactive power reference, while stochastic models aim to evaluate the effect of unpredictable specifics of EVs on other parameters. Therefore, deterministic pattern for EVs is proposed in this chapter, where it is assumed leaving and arriving time for these vehicles are 7:00 and 19:00, respectively. The average trip distance each day is 10 km and the initial energy available (state of charge) in EVs' batteries and BESS is 60% of the total capacity meaning 5 and 30 kWh each subgrid.

6.4.1 Power flow analysis in grid-connected mode

In this section, power flow problem is solved for 24 hours a day in grid-connected mode. First, tertiary controller, that is an optimization program, is solved, then active and reactive power generation by photovoltaic systems, and generation/consumption powers by BESS and EVs are called and sent to the operator to calculate power flow, and to the local controllers of the converters to perform primary control. It is worth to mention that local devices measure the frequency at PCC and dc voltage at DC link utilizing equation (6-3) to calculate active power transferred through the interlinking converter. Starting with the tertiary level, Figure 6-10 to Figure 6-13 illustrate the active and reactive powers generated by different sources for a day.

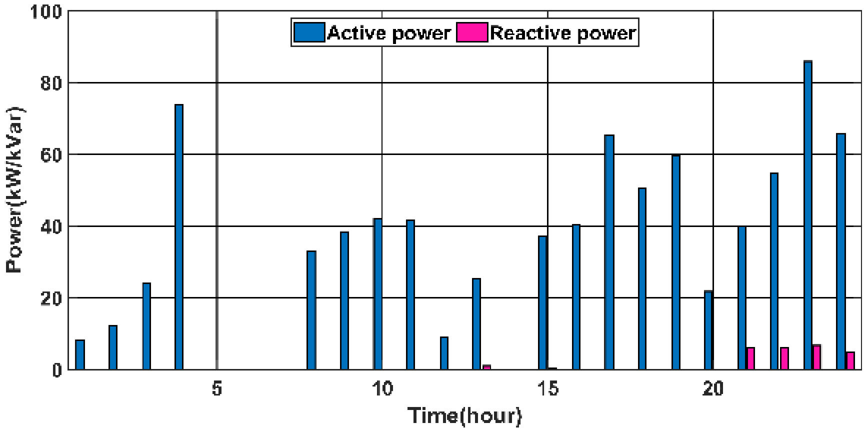

Figure 6-10. Hourly power purchased from the main grid.

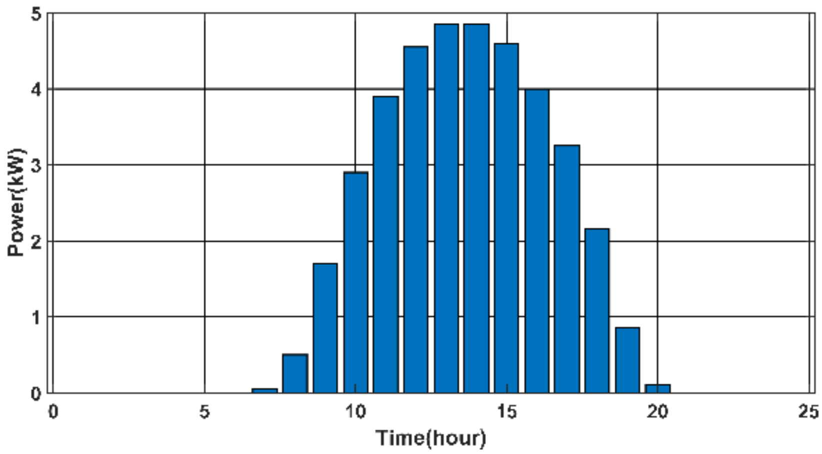

(a)

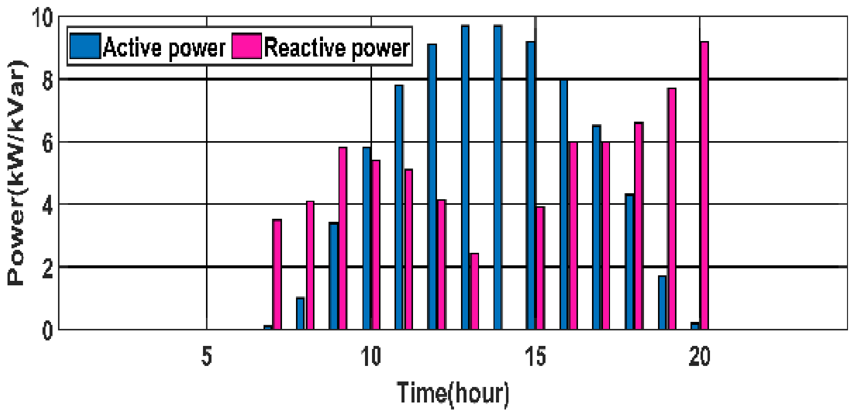

(b)

Figure 6-11. Hourly power generated by PV system: (a) DC grid, (b) AC grid.

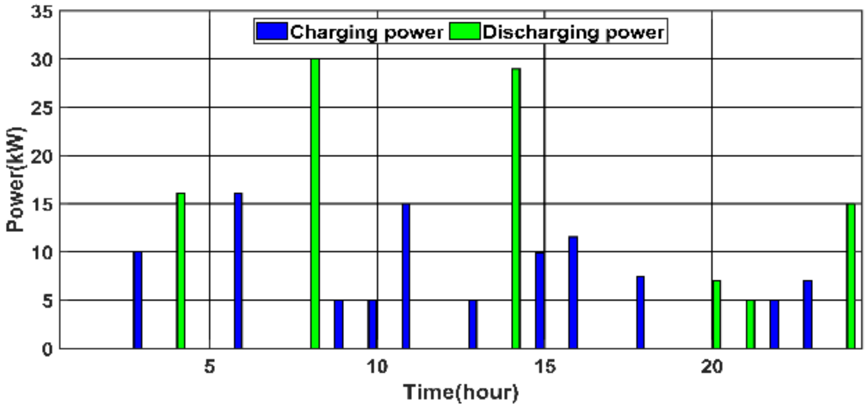

(a)

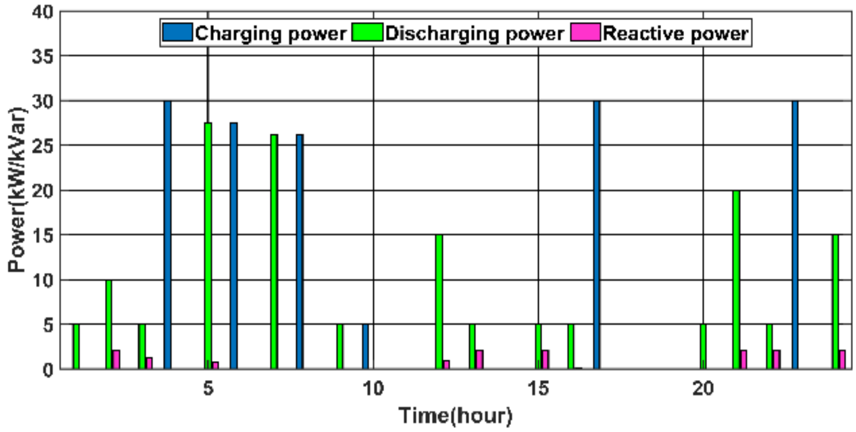

(b)

Figure 6-12. Hourly charging/discharging power at BESS: (a) DC grid, (b) AC grid.

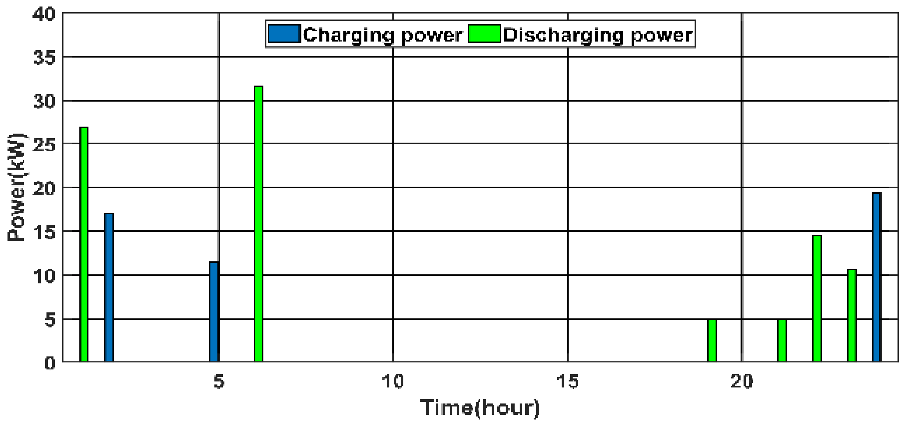

(a)

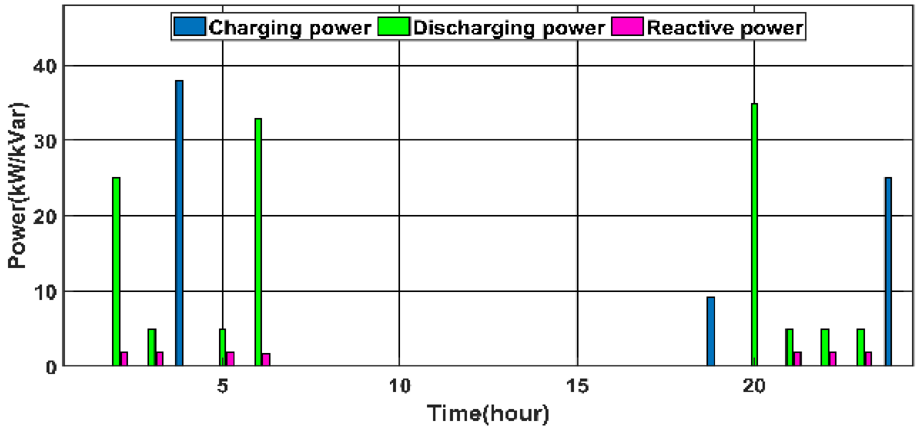

(b)

Figure 6-13. Hourly charging/discharging power at EV parking lot: (a) DC grid, (b) AC grid.

Figure 6-10 shows the active and reactive power purchased from the main grid. Figure 6-11 to Figure 6-13 depict power generated by PV systems, charging/discharging powers at BESSs units and EV parking lots, respectively, for both DC and AC subsystems. Looking at Figure 6-12 and Figure 6-13, it is clear that charging and discharging could not be issued simultaneously, and the corresponding converters at the AC grid inject reactive power only in discharging modes (see Figure 6-12 (b) and Figure 6-13 (b)). In addition, Figure 6-14 depicts the hourly active and reactive power exchange between AC and DC subgrids through the interlinking converter, where only at 1:00, 4:00, 6:00, 8:00 and 14:00 DC subgrid injects active and reactive power to the AC one. It is expected because DC grid has higher load demand than AC one (see Table 6-2).

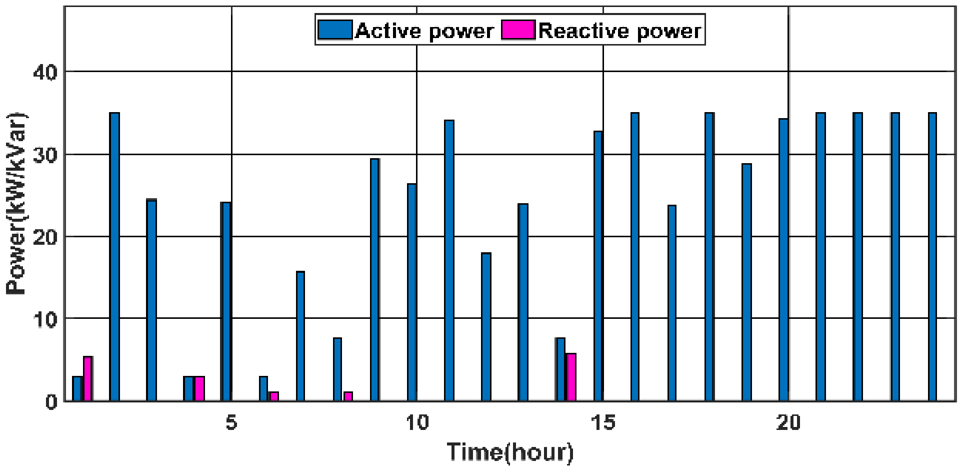

Figure 6-14. Hourly power transferred through interlinking converter.

At each hour, scheduled (reference) active and reactive powers for buses #3-5 in AC grid and active scheduled power for buses #8-10 in DC side come from the tertiary level (Figure

6-11 to Figure 6-13). Reactive powers in Figure 6-14 are utilized as the scheduled values for the bus #6 connected to the AC side of the IC, while the corresponding scheduled active power is calculated via equation (6-3). PCC bus #2, DC link bus #7, and bus #11 are considered as PQ/load buses with fixed hourly demands and negative scheduled active and reactive powers. Bus #1 is a slack connection with voltage magnitude 1 p.u. and phase angle 0. NR power flow model is implemented at each hour a day for the case study. Table 6-4 presents a comparison between power flow results for the proposed model and MATLAB/Simulink (power flow tool) including voltage magnitudes in p.u. and phase angles in radian. First column indicates Vn and δn which are voltage and phase angle of nth bus. The proposed power flow model is run by about 0.0155 second that is sufficiently fast. The simulation is run for 2 seconds, representing almost steady-state since voltage magnitudes and phase angles match those from the proposed model shown at Table IV with an error 4.0051e-11.

In addition, to show how converters' controllers work perfectly in steady-state, for both grid-connected and islanded modes a two-hour time interval is set each. To accomplish this, the microgrid under study, PV-storage systems, and parking lots, along with the corresponding controllers for the converters (Figure 6-2 to Figure 6-6), are designed and simulated using MATLAB/Simulink for

Table 6-4. NR power flow results comparison between the proposed model and MATLAB/Simulink for grid-connected mode.

	Proposed Model						MATLAB/Simulink					
time	1:00	3:00	5:00	7:00	9:00	11:00	1:00	3:00	5:00	7:00	9:00	11:00
V2	0.999937	0.999724	0.999816	0.999873	0.99954	0.999459	0.999937	0.999723	0.999815	0.999873	0.999539	0.999459
V3	0.999937	0.999724	0.999816	1.001115	1.001798	1.001742	0.999937	0.999723	0.999815	1.001115	1.001797	1.001742
V4	1.000248	1.000458	1.001767	1.00146	0.999851	0.999459	1.000248	1.000458	1.001766	1.001459	0.999850	0.999459
V5	0.999937	1.000741	1.000833	0.999873	0.99954	0.999459	0.999937	1.000740	1.000832	0.999873	0.999539	0.999459
V6	1.001987	0.998186	0.998293	0.998894	0.997705	0.997315	1.001986	0.998185	0.998293	0.998893	0.997704	0.997315
V7	1.000104	0.999314	0.99945	0.999506	0.998301	0.998309	1.000103	0.999313	0.999449	0.999506	0.998300	0.998309
V8	1.000103	0.999317	0.999452	0.99951	0.998377	0.998474	1.000103	0.999316	0.999451	0.999510	0.998376	0.998474
V9	1.000103	0.99891	0.999452	0.999508	0.998104	0.997706	1.000103	0.998910	0.999451	0.999508	0.998104	0.997706
V10	1.001195	0.999317	0.998984	0.999508	0.998308	0.998316	1.001194	0.999316	0.998984	0.999508	0.998307	0.998315
V11	0.999565	0.998991	0.999167	0.999152	0.997718	0.997798	0.999564	0.998991	0.999167	0.999152	0.997718	0.997797
δ2	-0.00315	-0.00928	0.000107	8.99e-5	-0.01475	-0.01598	-0.00314	-0.00927	0.000107	8.98e-05	-0.01474	-0.01598
δ3	-0.00315	-0.00928	0.000107	-9.33e-5	-0.01391	-0.01355	-0.00314	-0.00927	0.000107	-9.3e-05	-0.01390	-0.01354
δ4	-0.00138	-0.00759	0.009761	0.009302	-0.01298	-0.01598	-0.00137	-0.00758	0.009761	0.009302	-0.01297	-0.01598
δ5	-0.00315	-0.00764	0.001748	8.99e-5	-0.01475	-0.01598	-0.00314	-0.00763	0.001748	8.98e-05	-0.01474	-0.01598
δ6	-0.00246	-0.01777	-0.0083	-0.00537	-0.02484	-0.02772	-0.00245	-0.01777	-0.00830	-0.00536	-0.02483	-0.02772
time	14:00	16:00	18:00	20:00	22:00	24:00	14:00	16:00	18:00	20:00	22:00	24:00
V2	0.999973	0.999466	0.999346	0.999519	0.997034	0.997154	0.999973	0.999466	0.999346	0.999519	0.997034	0.997153
V3	1.000573	1.002079	1.001942	1.002774	0.997034	0.997154	1.000573	1.002078	1.001942	1.002773	0.997034	0.997153
V4	0.999973	0.999813	0.999346	0.99983	0.998054	0.998786	0.999973	0.999812	0.999346	0.999830	0.998054	0.998786
V5	0.999973	0.999466	0.999346	1.001627	0.998054	0.995545	0.999973	0.999466	0.999346	1.001626	0.998054	0.995544
V6	1.00248	0.997274	0.99716	0.997406	0.994882	0.994963	1.002479	0.997273	0.997160	0.997405	0.994881	0.994963
V7	1.00035	0.997864	0.997646	0.996798	0.996428	0.997615	1.000350	0.997863	0.997645	0.996798	0.996427	0.997614
V8	1.000546	0.998035	0.997743	0.996815	0.996442	0.997625	1.000546	0.998034	0.997742	0.996815	0.996442	0.997624
V9	1.001526	0.997403	0.997352	0.997095	0.996239	0.998234	1.001525	0.997402	0.997352	0.997095	0.996238	0.998234
V10	1.000349	0.997872	0.997655	0.996811	0.997034	0.996836	1.000348	0.997872	0.997655	0.996811	0.997033	0.996836
V11	0.999759	0.997252	0.996985	0.995876	0.995436	0.996934	0.999759	0.997252	0.996984	0.995876	0.995435	0.996933
δ2	-0.0001	-0.01541	-0.01938	-0.00793	-0.0208	-0.02527	-0.00010	-0.01540	-0.01937	-0.00793	-0.02080	-0.02526
δ3	0.003323	-0.01296	-0.01827	-0.00844	-0.0208	-0.02527	0.003322	-0.01295	-0.01827	-0.00843	-0.02080	-0.02526

$\delta 4$	-0.0001	-0.01365	-0.01938	-0.00616	-0.01915	-0.02007	-0.00010	-0.01364	-0.01937	-0.00616	-0.01915	-0.02007
$\delta 5$	-0.0001	-0.01541	-0.01938	0.004423	-0.01915	-0.03417	-0.00010	-0.01540	-0.01937	0.004423	-0.01915	-0.03416
$\delta 6$	0.002161	-0.02741	-0.03134	-0.01951	-0.03262	-0.03728	0.002160	-0.02740	-0.03134	-0.01951	-0.03261	-0.03728

two purposes. First, to demonstrate that the controllers work perfectly by following the references powers coming from the optimization in both grid-connected and islanded modes. It also proves that storage system in AC subgrid perfectly regulates voltage and frequency at PCC in islanded mode. Second, power flow toll in Simulink is used to perform power flow analysis, validating the power flow results from the proposed model (Table 6-4 and Table 6-5). In grid-connected operation mode, the simulation results, relating powers transferred through converters and dc link voltage, are exploited for 1 second, where the first half second represents the powers for the first hour, while the second half relates to the second hour of the time interval. Figure 6-15 to Figure 6-17show active and reactive powers imported from the main grid, and those from the PV, BESS, and EV lot, respectively, in the AC and DC subgrids at the time interval 3:00-4:00 a.m. Comparing these figures to Figure 6-10 to Figure 6-13, the powers imported from the main grid, PV generation, charging/discharging powers of the converters in BESS and EV parking lots perfectly match the set points that the tertiary controller sends to the local controllers. Note that PV systems in both AC and DC subsystems cannot generate power from 3:00 to 4:00 a.m. The storage system and parking lot in the AC subgrid start discharging (positive power) at 3:00, followed by discharging (negative power) at 4:00. In the DC subgrid, only BESS is active. It is first charged (power with a positive sign) and then starts discharging (negative power). Once all DGs follow the reference powers, the main grid injects active and reactive powers based on the values from optimization.

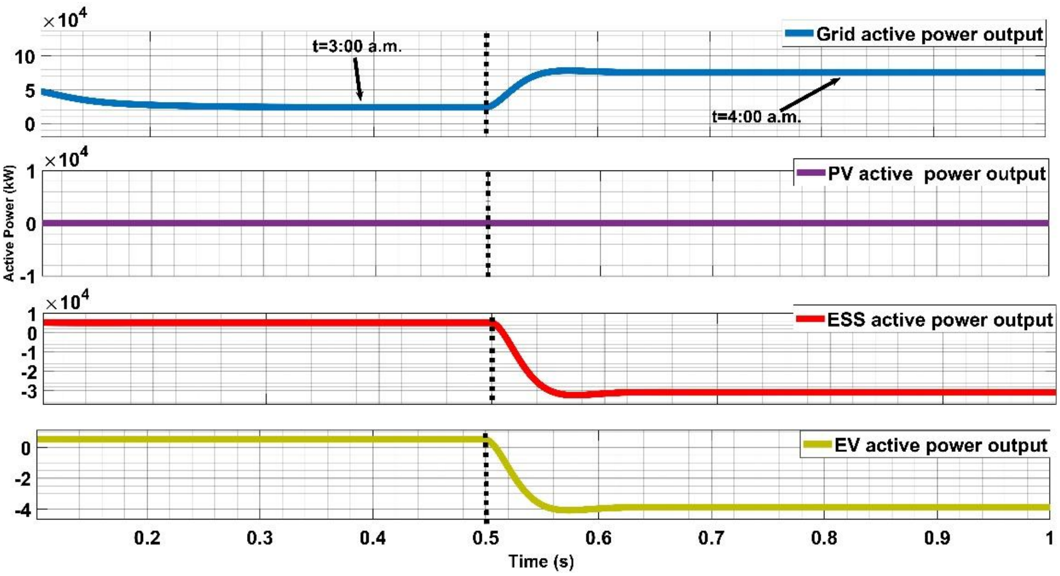

Figure 6-15. Active power flow in the AC subgrid.

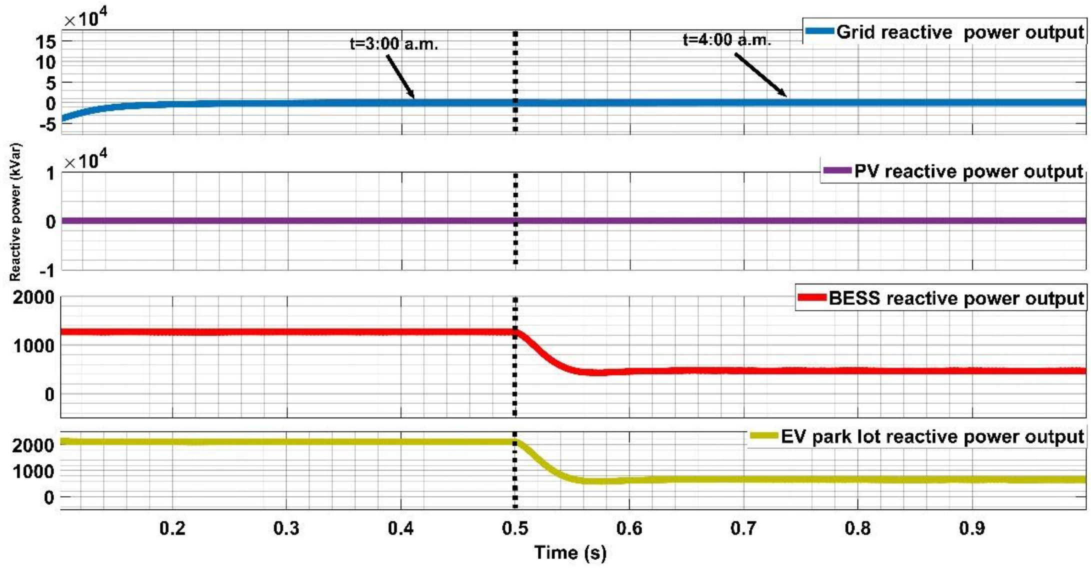

Figure 6-16. Reactive power flow in the AC subgrid.

These converters operate in current constant mode so that the corresponding controllers follow the references powers from the tertiary level. Figure 6-18 and Figure 6-19 depict the power exchange between two AC and DC subgrids through IC and dc link voltage respectively. IC follows a constant current mode where the reference active power is calculated by difference between normalized frequency and dc voltage leading to a stable dc voltage. In this case, at 3:00 active power is transferred from the AC side to the DC one (zero reactive power), whereas at 4:00 active and reactive powers are injected to the ac grid from the DC one.

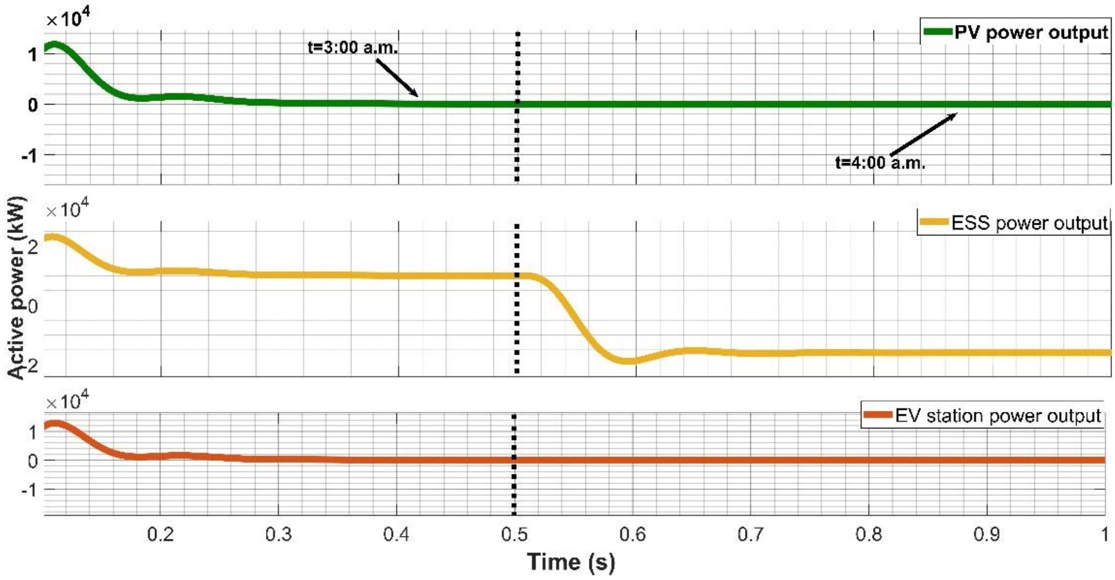

Figure 6-17. Active power flow in the DC subgrid.

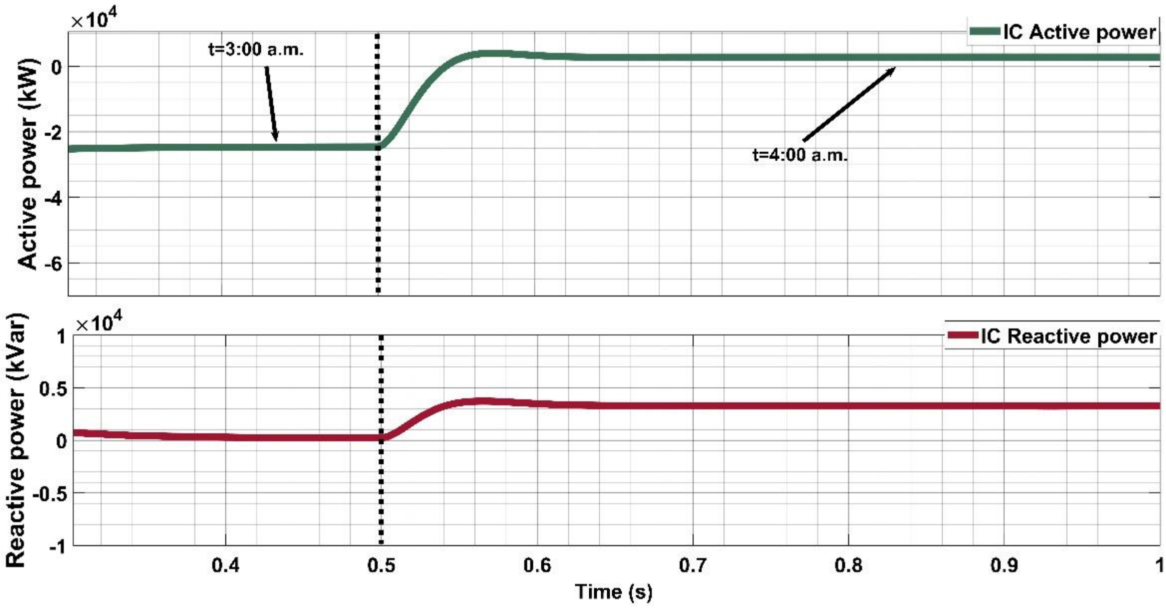

Figure 6-18. Active and reactive power flow in the IC.

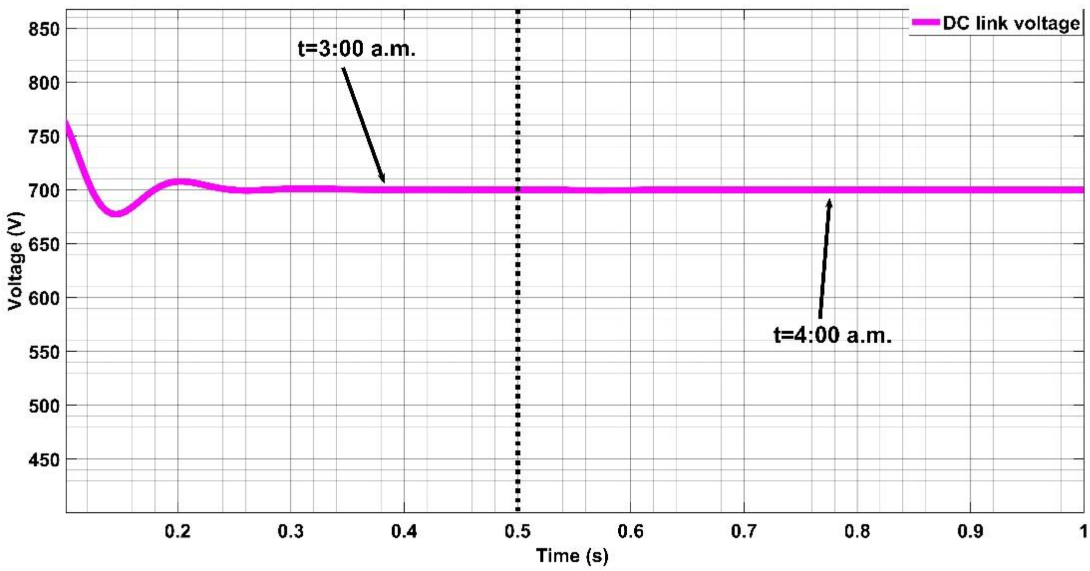

Figure 6-19. DC link voltage connected to IC.

6.4.2 Power flow analysis in islanded mode

Hierarchal power flow analysis is also conducted for the case study in islanded operating mode. To avoid repetitious expressions, only results and analysis related to island mode are discussed. In this case, the AC/DC hybrid grid is disconnected from the main grid. As is discussed in section III, in island mode, PV systems and flexible sources may not supply total AC and DC loads at each hour. So, the tertiary level optimizes the rate of load shedding so that the remind load could be powered. In such a case, converters connected to the PV systems, EV parking lots, BESS in DC system, and the IC follow the same corresponding control modes as those in grid-connected mode, but BESS in the AC grid switches to voltage source mode where it tries to follow the reference powers aiming to keep voltage and frequency in the reference values at PCC bus. Starting with the tertiary level, Figures 20-23 illustrate the active and reactive powers generated by different sources for a day. The note is that, since the hybrid grid is disconnected from the main grid, load consumption in DC grid is lower than AC one as well, IC injects active and reactive power to AC grid more hours than in grid-connected operating mode (see Fig. 23).

Power flow calculations by the proposed model and simulation are reported in Table V. Like in grid-connected mode, power flow results by simulation match those from the model perfectly by an error 2.0007e-13, where the proposed model takes 0.013 second which is meaningfully fast.

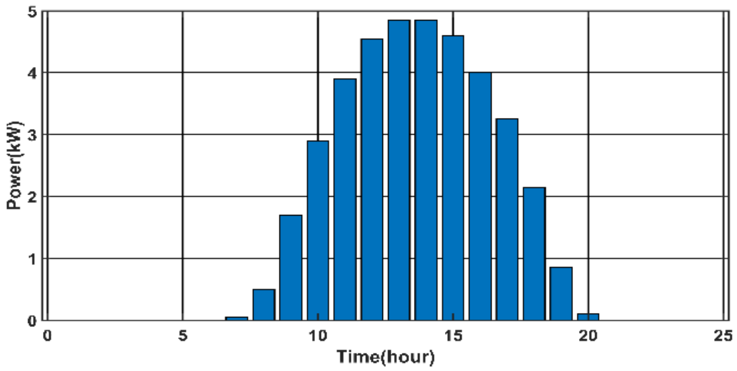

(a)

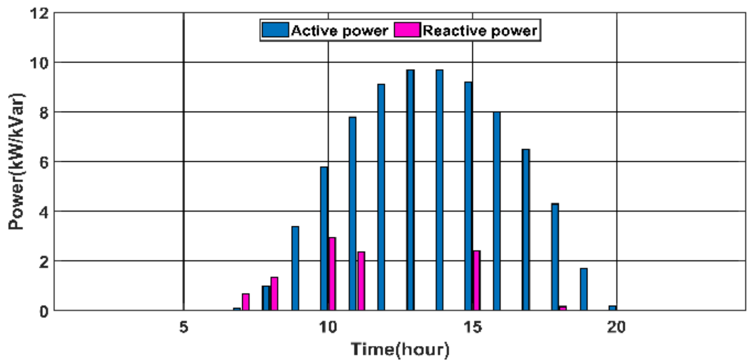

(b)

Figure 6-20. Hourly power generated by PV system: (a) DC grid, (b) AC grid.

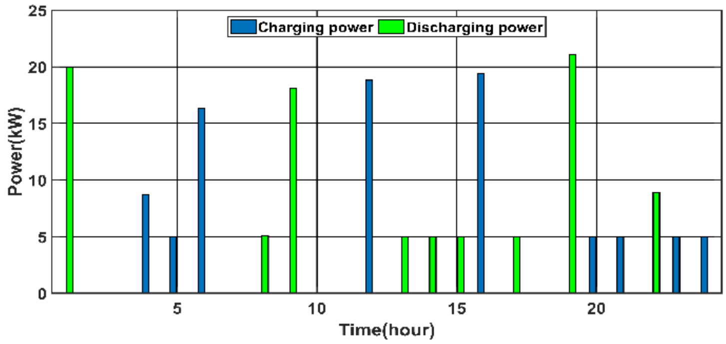

(a)

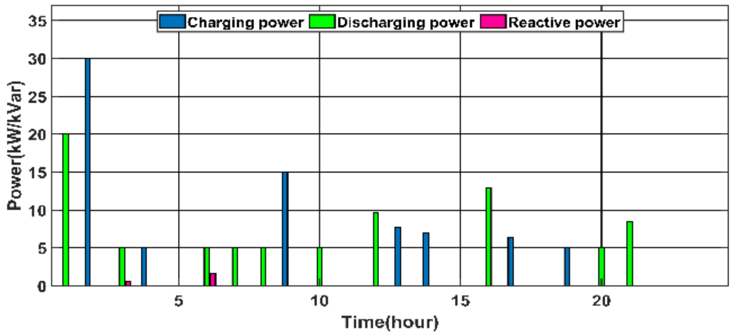

(b)

Figure 6-21. Hourly power generated by BESS system: (a) DC grid, (b) AC grid.

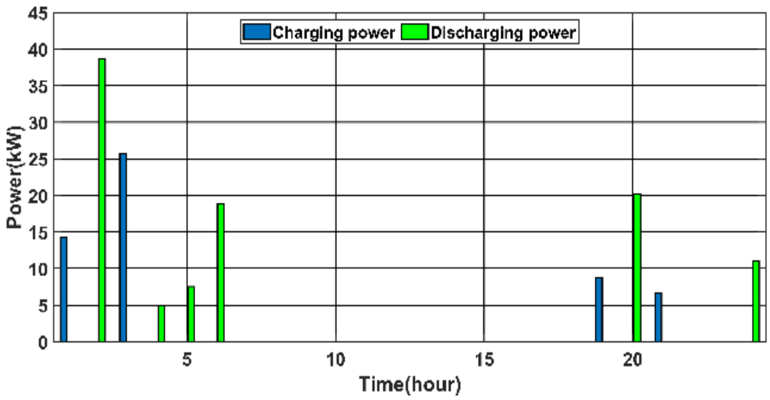

(a)

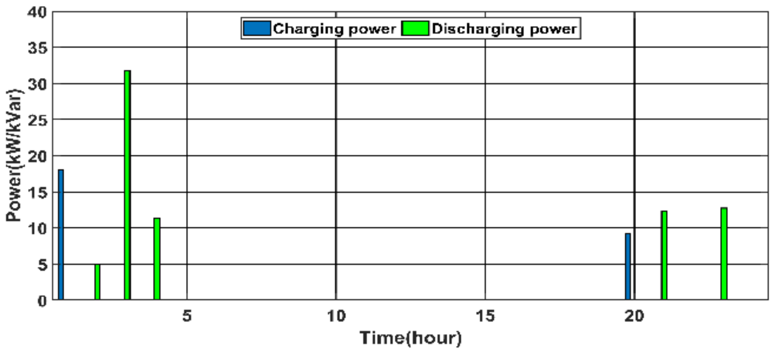

(b)

Figure 6-22. Hourly power generated by EV parking lot: (a) DC grid, (b) AC grid.

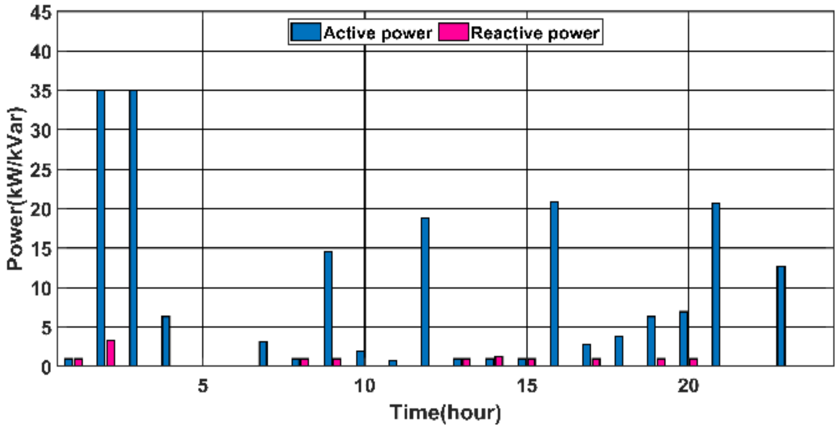

Figure 6-23. Hourly power exchange between AC and DC grids through IC.

To assess the behavior of the primary controller of the converters in islanded mode, the controlled hybrid AC/DC grid is simulated for one second (like that in grid-connected mode) in the period 9:00-10:00 a.m. using MATLAB/Simulink. Corresponding power outputs are illustrated in Fig. 24-27. Comparing these figures to figures 20-23, PV generation, charging/discharging powers of the converters in BESS and EV parking lots perfectly match the set points that the tertiary controller sends to the local controllers. Looking at Fig. 25, at 9:00 a.m. BESS is charged at a value lower than the reference point, while at 10:00 it starts discharging where its power output is a little higher than the reference value to keep voltage and frequency at PCC close to their nominal values. Voltage, frequency, and load current at PCC are depicted in Fig. 28, DC link voltage is shown in Fig. 29 as well. Although the operation mode of BESS, the rate of loads, and injected power direction at IC are changed for two hours, voltage and frequency at PCC and DC link voltage remain stable.

Table 6-5. NR power flow results comparison between the proposed model and MATLAB/Simulink for islanded mode.

	Proposed Model						MATLAB/Simulink					
time	1:00	3:00	5:00	700	9:00	11:00	1:00	3:00	5:00	7:00	9:00	11:00
V2	0.999893	0.999939	1	0.999928	0.999893	0.999745	0.999893	0.999939	1	0.999928	0.999893	0.999745
V3	0.999896	0.999941	1	1.000172	1.000087	1.00103	0.999896	0.999941	1	1.000172	1.000087	1.00103
V4	1.001018	1.000422	1	1.000211	0.999055	0.999754	1.001018	1.000422	1	1.000211	0.999055	0.999754
V5	0.998887	1.001719	1	0.999931	0.999896	0.999754	0.998887	1.001719	1	0.999931	0.999896	0.999754
V6	1.000306	0.997979	1	0.999757	1.001069	0.999716	1.000306	0.997979	1	0.999757	1.001069	0.999716
V7	0.999975	1.000275	0.999991	1.000014	0.999862	0.999989	0.999975	1.000275	0.999991	1.000014	0.999862	0.999989
V8	0.999975	1.000274	0.999991	1.000016	0.999932	1.000148	0.999975	1.000274	0.999991	1.000016	0.999932	1.000148
V9	1.000788	1.000274	0.999788	1.000014	1.000599	0.999989	1.000788	1.000274	0.999788	1.000014	1.000599	0.999989
V10	0.999396	0.999228	1.000297	1.000014	0.999863	0.999989	0.999396	0.999228	1.000297	1.000014	0.999863	0.999989
V11	0.999867	0.999949	0.999934	0.999943	0.999745	0.999885	0.999867	0.999949	0.999934	0.999943	0.999745	0.999885
$\delta 2$	-0.0002	-0.00011	2.83e-15	-0.00013	-0.0002	-0.00047	-0.0002	-0.00011	2.83e-15	-0.00013	-0.0002	-0.00047
$\delta 3$	-0.0002	-0.00011	2.84e-15	-0.00014	0.001004	0.002125	-0.0002	-0.00011	2.84e-15	-0.00014	0.001004	0.002125
$\delta 4$	0.006873	0.001616	2.84e-15	0.001636	-0.0055	-0.00047	0.006873	0.001616	2.84e-15	0.001636	-0.0055	-0.00047
$\delta 5$	-0.00656	0.011095	2.84e-15	-0.00013	-0.0002	-0.00047	-0.00656	0.011095	2.84e-15	-0.00013	-0.0002	-0.00047
$\delta 6$	8.65e-05	-0.01249	2.84e-15	-0.00123	0.004895	-0.00071	8.65e-05	-0.01249	2.84e-15	-0.00123	0.004895	-0.00071
time	14:00	16:00	18:00	20:00	22:00	24:00	14:00	16:00	18:00	20:00	22:00	24:00

V2	0.999866	1	0.999982	0.999893	1	1	0.999866	1	0.999982	0.999893	1	1
V3	1.000415	1.000449	1.000283	0.999908	1	1	1.000415	1.000449	1.000283	0.999908	1	1
V4	0.999481	1.000723	0.999982	1.000177	1	1	0.999481	1.000723	0.999982	1.000177	1	1
V5	0.999871	1	0.999982	0.999382	1	1	0.999871	1	0.999982	0.999382	1	1
V6	1.000367	0.998829	0.99977	1.000641	1	1	1.000367	0.998829	0.99977	1.000641	1	1
V7	0.999943	1.00015	1.000009	0.993783	0.999968	0.999978	0.999943	1.00015	1.000009	0.993783	0.999968	0.999978
V8	1.000141	1.000312	1.000097	0.993787	0.999968	0.999978	1.000141	1.000312	1.000097	0.993787	0.999968	0.999978
V9	1.000147	0.999361	1.000009	0.993578	1.00033	0.999775	1.000147	0.999361	1.000009	0.993578	1.00033	0.999775
V10	0.999944	1.00015	1.000009	0.99461	0.999968	1.00043	0.999944	1.00015	1.000009	0.99461	0.999968	1.00043
V11	0.999826	1.000026	0.999875	0.993594	0.999767	0.99984	0.999826	1.000026	0.999875	0.993594	0.999767	0.99984
$\delta 2$	-0.00025	2.84e-15	-3.3e-05	-0.0002	2.83e-15	2.83e-15	-0.00025	2.84e-15	-3.39e-5	-0.0002	2.83e-15	2.83e-15
$\delta 3$	0.003183	0.002828	0.001475	-0.00013	2.84e-15	2.84e-15	0.003183	0.002828	0.001475	-0.00013	2.84e-15	2.84e-15
$\delta 4$	-0.00271	0.004556	-3.3e-05	0.00157	2.84e-15	2.84e-15	-0.00271	0.004556	-3.37e-5	0.00157	2.84e-15	2.84e-15
$\delta 5$	-0.00025	2.85e-15	-3.3e-05	-0.00344	2.84e-15	2.84e-15	-0.00025	2.85e-15	-3.37e-5	-0.00344	2.84e-15	2.84e-15
$\delta 6$	2.08e-05	-0.00738	-0.00137	0.002196	2.84e-15	2.84e-15	2.08e-05	-0.00738	-0.00137	0.002196	2.84e-15	2.84e-15

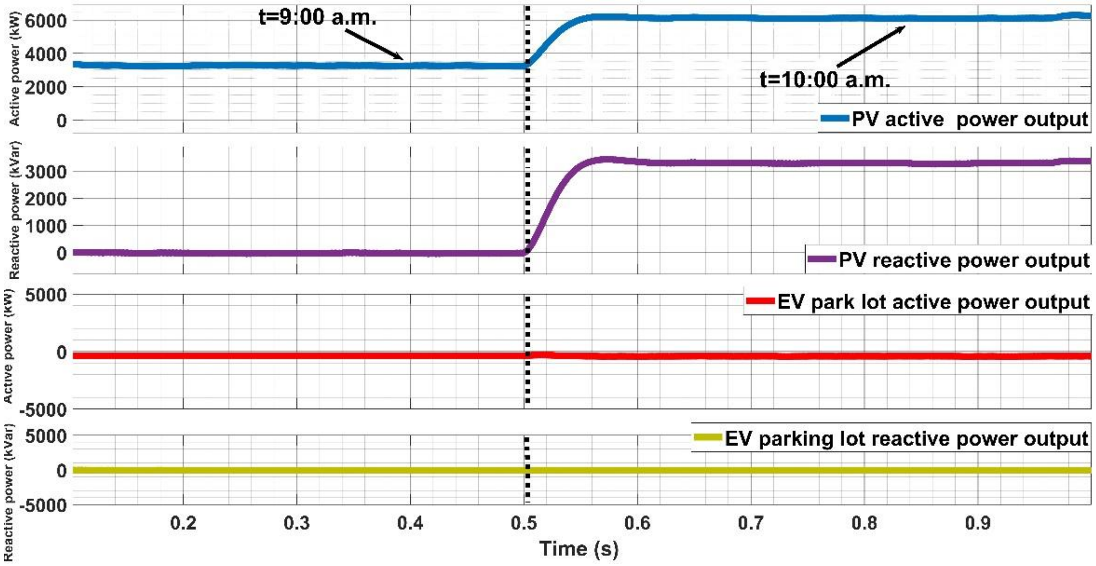

Figure 6-24. Active and reactive powers of PV system and parking lot in AC side.

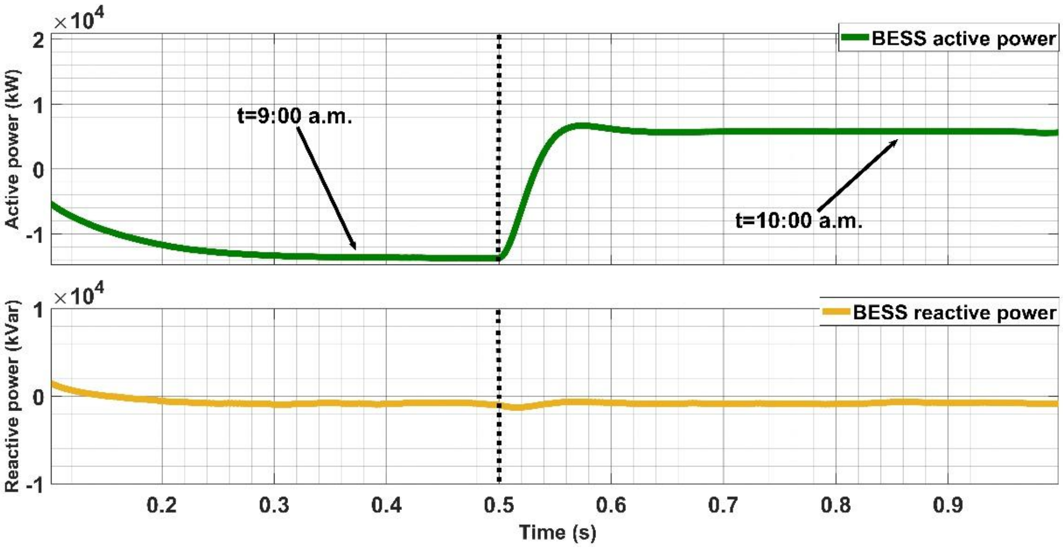

Figure 6-25. Active and reactive powers of BESS in AC side.

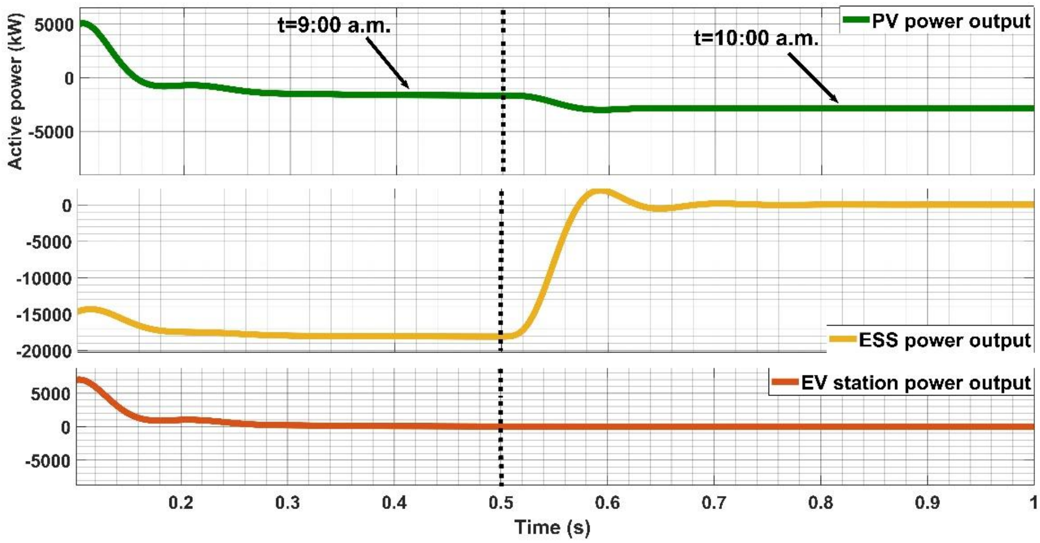

Figure 6-26. Active power flow in DC subgrid.

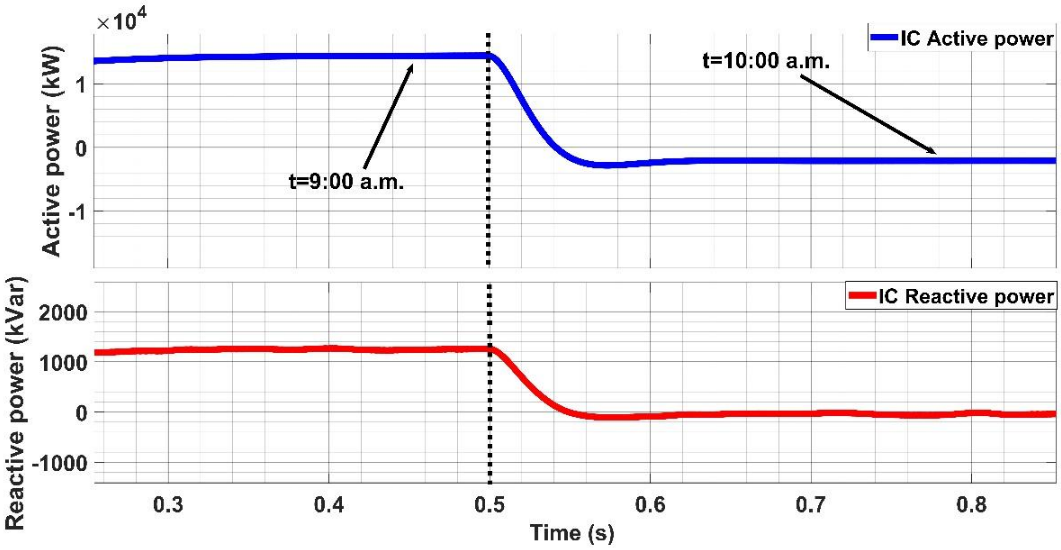

Figure 6-27. Active and reactive power flow in the IC.

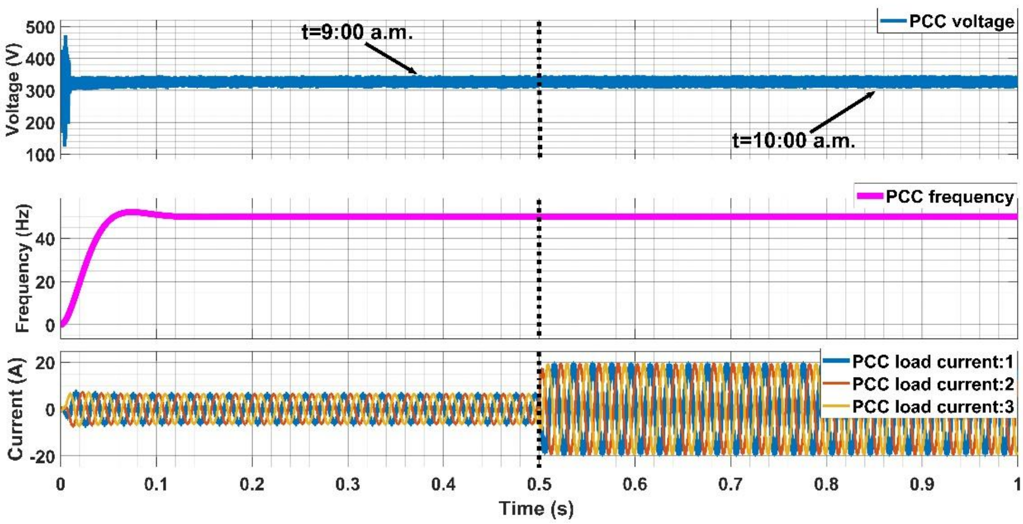

Figure 6-28. Voltage, frequency, and load current at PCC.

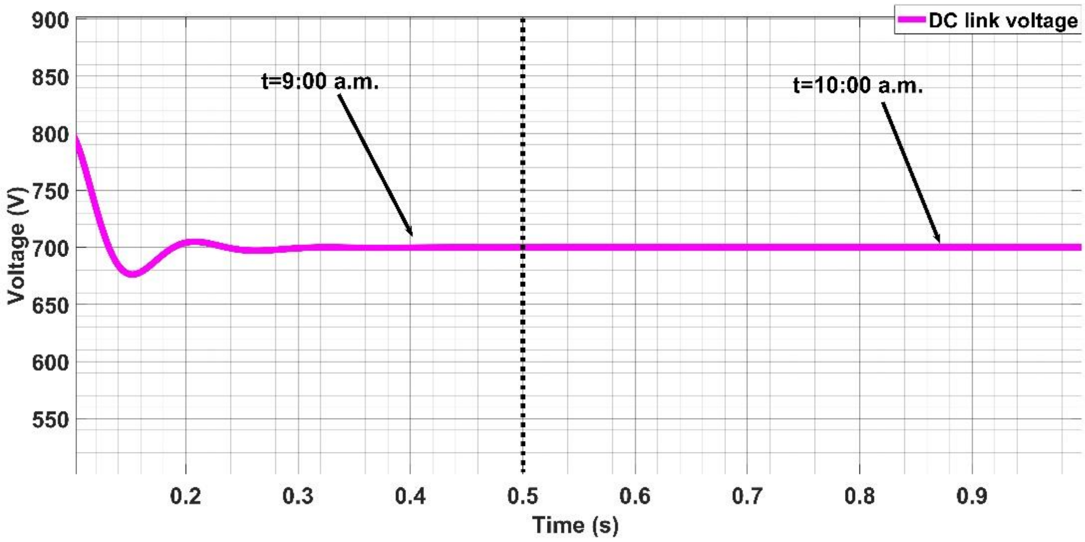

Figure 6-29. DC link voltage.

6.5 Key findings and conclusion

This chapter proposes a power flow analysis for a two-level controlled AC/DC hybrid microgrid in both grid-connected and islanded operating modes. In grid-connected mode, the tertiary level controller, playing energy management system role, minimizes the daily cost of the energy purchased from the utility, leading to active and reactive power references calculation. These scheduled power set-points are then sent to the converters' controller connected to the RESs and the flexible resources and are used in Newton-Raphson power flow calculations. Local controller adopts current control mode as the primary controller to generate and follow the power references. In islanded mode, however, tertiary level tries to minimize the load shedding to obtain a stable and reliable load supply. To keep a stable voltage and frequency in the AC system, the converter connected to the storage system implements P- ω/Q-V droops to generate voltage and frequency references, meanwhile tries to produce powers close to the corresponding references. Other sources, however, remain in current control mode. In both operation modes, interlinking converter plays the most significant role to transmit power between two grids. The difference between DC link voltage and frequency is used as a droop control to identify the direction of injected power so that voltage of dc link and frequency at PCC (especially in islanded mode) are kept stable. Power flow equations are solved using the unified NR technique sufficiently fast. Results from the optimization program are obtained for the proposed case study and shown at bar charts. In islanded mode, it is noticeable that some loads must be shedded since RESs and storage systems may not power them. Power flow analysis results from simulated hybrid grid by Simulink perfectly match with those from the NR model with a high accuracy. In addition, control schemes are simulated and results at graphs represent controllers precisely follows the set points came from the optimization level, and frequency stability in islanded mode. The point is that the proposed methodology is a general model applicable to real existing grids with diverse configurations comprising various resources and loads. These highlights mentioned above prove the effectiveness, precision model with a sufficient convergence speed. Power flow analysis model proposed in this chapter could be implemented for other vital issues in power systems such as fault and cascading failure analysis, stability, among others.

Appendix 1

NOMENCLATURE

Indices and Sets	
t	Index for time interval
n, m	Index for bus in AC/DC grids
Ω_{ac}	Set of buses in AC grid
Ω_{dc}	Set of buses in DC grid
T_{out}	Set of hours EVs are out of the parking lot
Parameters	
k_{ic}^{p}	Active power droop coefficient for interlinking converter
ω/ω^{*}	Operation and reference frequency [Hz]
$\omega^{max}/\omega^{min}$	Upper and lower limit for frequency [Hz]
V_{dc}^{*}	Reference voltage at DC link [V]
$V_{dc}^{max}/V_{dc}^{min}$	Upper and lower limit for DC link voltage [V]
c_g	Price of power purchased from the main grid [€]
P_l^{ac}/P_l^{dc}	Active power consumption in AC and DC grids [kW]
Q_l^{ac}	Reactive power consumption in AC grids [kVar]
M	Large positive constant
P_g^{max}/Q_g^{max}	Upper limit for active and reactive power purchased from the main grid [kW/kVar]
P_{max}^{pv}	Upper limit for active power generated by PV systems [kW]
P_{ic}^{max}	Active power transmission capacity of the IC [kW]
S_{ic}/S_{pv}	Apparent power of the interlinking and the converter connected to PV systems [kVA]
S_s/S_e	Apparent power of the converters connected to BESS and EV parking lot [kVA]
$P_{dis}^{s,min}/P_{dis}^{s,max}$	Lower and upper limit for discharging power at BESS in AC and DC grids [kW]
$P_{ch}^{s,min}/P_{ch}^{s,max}$	Lower and upper limit for charging power at BESS in AC and DC grids [kW]

$P_{dis}^{e,min}$ $/P_{dis}^{e,max}$	Lower and upper limit for discharging power at EV lot in AC and DC grids [kW]
$P_{ch}^{e,min}$ $/P_{ch}^{e,max}$	Lower and upper limit for charging power at EV lot in AC and DC grids [kW]
$U_{ac/dc}^{s}(0)$	Initial available energy at BESS in AC and DC grids [kWh]
$U_{ac/dc}^{e}(0)$	Initial available energy at EV's parking lot in AC and DC grids [kWh]
E_{s}^{max}/E_{s}^{min}	Upper and lower limit for stored energy at BESS in AC and DC grids [kWh]
E_{e}^{max}/E_{e}^{min}	Upper and lower limit for stored energy at EV parking lot in AC and DC grids [kWh]
Q	Efficiency of the batteries in storage systems and EV parking lots [%]
N	Total number of EVs in each subgrid
D	Average distance of movement each EV traverses a day [Km]
t_l	Time that EVs leave parking lot
λ	Discharge rate of EVs' battery per Km [kW/Km]
G/B	Conductance/susceptance of the admittance matrix in AC grid
g	Conductance matrix in DC grid

Variables

C_T	Total price for importing power from the main grid [€]
P_g	Active power injected from the main grid [kW]
Q_g	Reactive power injected from the main grid [kVar]
P_{ac}^{pv}/Q_{ev}^{dis}	Active and reactive power generated by PV in AC grid [kW/kVar]
$P_{dis}^{s,ac}/P_{ch}^{s,ac}$	Charging/discharging active power at BESS in AC grid [kW]
$P_{dis}^{e,ac}/P_{ch}^{e,ac}$	Charging/discharge active power at EV parking lot in AC grid [kW]
Q_{ac}^{s}/Q_{ac}^{ev}	Reactive power generated by BESS and EV parking lot in AC grid [kVar]
P_{ic}/Q_{ic}	Active and reactive power transferred through the IC [kW/kVar]
P_{dc}^{pv}	Active power generated by PV in DC grid [kW]
$P_{dis}^{s,dc}/P_{ch}^{s,dc}$	Charging/discharging active power at BESS in DC grid [kW]
$P_{dis}^{e,dc}/P_{ch}^{e,dc}$	Charging/discharge active power at EV parking lot in DC grid [kW]
$I_{dis}^{s,ac}/I_{ch}^{s,ac}$	Binary variable showing charging/discharging status of BESS in AC grid
$I_{dis}^{e,ac}/I_{ch}^{e,ac}$	Binary variable showing charging/discharging status at EV parking lot in AC grid

$I_{dis}^{s,dc}/I_{ch}^{s,dc}$	Binary variable showing charging/discharging status of BESS in DC grid
$I_{dis}^{e,dc}/I_{ch}^{e,dc}$	Binary variable showing charging/discharging status at EV parking lot in DC grid
I_{ic}	Binary variable showing the direction of power transferred by IC
$E_{ac/dc}^{s}/E_{ac/dc}^{e}$	Energy available at BESS and EV parking lot in both AC/DC grids [kWh]
L_{T}^{sh}	Total load shedded
γ^{ac}/γ^{dc}	Rate of load shedding in AC and DC grids
$P_{l,i}^{ac}/Q_{l,i}^{ac}$	Active/reactive power consumption in islanded mode in AC grid [kW/kVar]
$P_{l,i}^{dc}$	Active power consumption in island mode in DC grid [kW]
P_{n}^{ac}/Q_{n}^{ac}	Active/reactive power injected to the *n*th bus in AC grid [kW/kVar]
P_{n}^{dc}	Active power injected into the *n*th bus in DC grid [kW]
$\lvert V_n\rvert/\lvert V_m\rvert$	Voltage magnitude of the *n*th/*m*th bus [p.u.]
δ_n/δ_m	Phase angle of the *n*th/*m*th bus [radians]

Acknowledgement

The PH D course has been funded thanks to the national programme “PON Programma Operativo Nazionale 2014-2020 - Dottorati Innovativi con caratterizzazione industriale”, Azione: I.1 - Dottorati di ricerca innovativi (2014IT16M2OP005).

The studies in chapters 2 and 6 have been developed within the framework of a research collaboration agreement between the University of Palermo and ENEA, funded by the Research Fund for the Italian Electrical System under the Contract Agreement “Accordo di Programma 2019-2021 – PTR_19_21_ENEA_PRG_10” between ENEA and the Ministry of Economic Development - Progetto 2.7.

The study presented in chapter 6 has been developed within the framework of the research project HYPERRIDE that has received funding from the European Union H2020 Framework Programme (H2020 / 2014-2020) under Grant Agreement No 957788.

List of publications

List of Journal publications

- Hierarchical-power-flow-based energy management for alternative/direct current hybrid microgrids. Salar Moradi, Gibran David Agundis Tinajero, Juan C. Vasquez, Gaetano Zizzo, Josep M. Guerrero, Eleonora Riva Sanseverino, Sustain. Energy, Grids Netw., vol. 38, Apr. 2024. https://doi.org/10.1016/j.segan.2024.101384

- Optimal nanogrid planning at building level. Salar Moradi, Vahid Vahidinasab, Gaetano Zizzo, Int J Electr Power Energy Syst, Vol153, 2023. https://doi.org/10.1016/j.ijepes.2023.109409

- A stochastic approach for self-healing capability evaluation in active islanded AC/DC hybrid microgrids. Salar Moradi, G. Zizzo, S. Favuzza, and F. Massaro,Sustain. Energy, Grids Netw., vol. 33, Mar. 2023. https://doi.org/10.1016/j.segan.2022.100982

- A General Methodology for Short-circuit Calculations in Hybrid AC/DC Microgrids. Favuzza S, Mitolo M, Moradi S, Musca R, Zizzo G. IEEE Trans Ind Appl 2023;59. https://doi.org/10.1109/TIA.2023.3234232

List of Conference publications

- Energy Management System in Grid-Connected Small-Scale AC/DC Microgrids Including Renewable Sources and Flexible Loads. Salvatore Favuzza, Salar Moradi, Rossano Musca, Gaetano Zizzo, BLORIN, 2022, 212-217. https://doi.org/10.1109/BLORIN54731.2022.10027932

- Predictions in Resilient Hybrid AC/DC Grids Leveraged by an Interoperable and Secure ICT Platform. M. Mammina; A. Rossi; D. Arnone; G. Zizzo; Salar Moradi; Paul Smith, 2022 EEEIC / I&CPS Europe. https://doi.org/10.1109/EEEIC/ICPSEurope54979.2022.9854625

- Dynamic Control of Static Converters for the Transition from Grid-on to Grid-off Operation of AC/DC Microgrids. S. Favuzza; M. G. Ippolito; F. Massaro; Salar Moradi; R. Musca, 2022 EEEIC / I&CPS Europe. https://doi.org/10.1109/EEEIC/ICPSEurope54979.2022.9854668

- A Simulation Analysis for Assessing the Reliability of AC/DC Hybrid Microgrids – Part II: Port Area and Residential Area. A. Bonì; S. Favuzza; M. G. Ippolito; F. Massaro; Salar Moradi; R. Musca, 2022 EEEIC / I&CPS Europe. https://doi.org/10.1109/EEEIC/ICPSEurope51590.2021.9584607

- A Simulation Analysis for Assessing the Reliability of AC/DC Hybrid Microgrids – Part I: Underground Station and Car Parking. A. Bonì; S. Favuzza; M. G. Ippolito; F. Massaro; Salar Moradi; R. Musca, 2022 EEEIC / I&CPS Europe. https://doi.org/10.1109/EEEIC/ICPSEurope51590.2021.9584826

References

[1] S. Parhizi, H. Lotfi, A. Khodaei, and S. Bahramirad, "State of the art in research on microgrids: A review," *IEEE access,* vol. 3, pp. 890-925, 2015.

[2] H. Jiayi, J. Chuanwen, and X. Rong, "A review on distributed energy resources and MicroGrid," *Renewable and Sustainable Energy Reviews,* vol. 12, no. 9, pp. 2472-2483, 2008.

[3] R. A. Kaushik and N. M. Pindoriya, "A hybrid AC-DC microgrid: Opportunities & key issues in implementation," in *2014 International Conference on Green Computing Communication and Electrical Engineering (ICGCCEE)*, 2014: IEEE, pp. 1-6.

[4] T. Dragičević, X. Lu, J. C. Vasquez, and J. M. Guerrero, "DC microgrids—Part II: A review of power architectures, applications, and standardization issues," *IEEE transactions on power electronics,* vol. 31, no. 5, pp. 3528-3549, 2015.

[5] T. Dragičević, X. Lu, J. C. Vasquez, and J. M. Guerrero, "DC microgrids—Part I: A review of control strategies and stabilization techniques," *IEEE Transactions on power electronics,* vol. 31, no. 7, pp. 4876-4891, 2015.

[6] S. Pannala, N. Patari, A. K. Srivastava, and N. P. Padhy, "Effective control and management scheme for isolated and grid connected DC microgrid," *IEEE Transactions on Industry Applications,* vol. 56, no. 6, pp. 6767-6780, 2020.

[7] V. Boscaino, J. Guerrero, I. Ciornei, L. Meng, E. R. Sanseverino, and G. Zizzo, "Online optimization of a multi-conversion-level DC home microgrid for system efficiency enhancement," *Sustainable cities and society,* vol. 35, pp. 417-429, 2017.

[8] V. Narayanan, S. Kewat, and B. Singh, "Solar PV-BES based microgrid system with multifunctional VSC," *IEEE Transactions on Industry Applications,* vol. 56, no. 3, pp. 2957-2967, 2020.

[9] J. Khodabakhsh and G. Moschopoulos, "Simplified hybrid AC–DC microgrid with a novel interlinking converter," *IEEE Transactions on Industry Applications,* vol. 56, no. 5, pp. 5023-5034, 2020.

[10] A. Bonì *et al.*, "A Simulation Analysis for Assessing the Reliability of AC/DC Hybrid Microgrids–Part I: Underground Station and Car Parking," in *2021 IEEE International Conference on Environment and Electrical Engineering and 2021 IEEE Industrial and Commercial Power Systems Europe (EEEIC/I&CPS Europe)*, 2021: IEEE, pp. 1-6.

[11] A. Bonì *et al.*, "A simulation analysis for assessing the reliability of AC/DC hybrid microgrids–Part II: Port area and residential area," in *2021 IEEE International Conference on Environment and Electrical Engineering and 2021 IEEE Industrial and Commercial Power Systems Europe (EEEIC/I&CPS Europe)*, 2021: IEEE, pp. 1-6.

[12] J. J. Justo, F. Mwasilu, J. Lee, and J.-W. Jung, "AC-microgrids versus DC-microgrids with distributed energy resources: A review," *Renewable and sustainable energy reviews,* vol. 24, pp. 387-405, 2013.

[13] E. Unamuno and J. A. Barrena, "Hybrid ac/dc microgrids—Part I: Review and classification of topologies," *Renewable and Sustainable Energy Reviews,* vol. 52, pp. 1251-1259, 2015.

[14] E. Unamuno and J. A. Barrena, "Hybrid ac/dc microgrids—Part II: Review and classification of control strategies," *Renewable and Sustainable Energy Reviews,* vol. 52, pp. 1123-1134, 2015.

[15] J. M. Guerrero, P. C. Loh, T.-L. Lee, and M. Chandorkar, "Advanced control architectures for intelligent microgrids—Part II: Power quality, energy storage, and AC/DC microgrids," *IEEE Transactions on industrial electronics,* vol. 60, no. 4, pp. 1263-1270, 2012.

[16] F. Nejabatkhah, Y. W. Li, and H. Tian, "Power quality control of smart hybrid AC/DC microgrids: An overview," *Ieee access,* vol. 7, pp. 52295-52318, 2019.

[17] M. N. Ambia, K. Meng, W. Xiao, and Z. Y. Dong, "Nested formation approach for networked microgrid self-healing in islanded mode," *IEEE Transactions on Power Delivery,* vol. 36, no. 1, pp. 452-464, 2020.

[18] Z. Wang and J. Wang, "Self-healing resilient distribution systems based on sectionalization into microgrids," *IEEE Transactions on Power Systems,* vol. 30, no. 6, pp. 3139-3149, 2015.

[19] W. Sun, S. Ma, I. Alvarez-Fernandez, R. Roofegari nejad, and A. Golshani, "Optimal self-healing strategy for microgrid islanding," *IET Smart Grid,* vol. 1, no. 4, pp. 143-150, 2018.

[20] M. Al Owaifeer and M. Al-Muhaini, "MILP-based technique for smart self-healing grids," *IET Generation, Transmission & Distribution,* vol. 12, no. 10, pp. 2307-2316, 2018.

[21] Y. Jia, C. S. Lai, Z. Xu, S. Chai, and K. P. Wong, "Adaptive partitioning approach to self-sustained smart grid," *IET Generation, Transmission & Distribution,* vol. 11, no. 2, pp. 485-494, 2017.

[22] S. A. Arefifar, Y. A.-R. I. Mohamed, and T. H. El-Fouly, "Comprehensive operational planning framework for self-healing control actions in smart distribution grids," *IEEE Transactions on Power Systems,* vol. 28, no. 4, pp. 4192-4200, 2013.

[23] H. Lin *et al.*, "Self-healing attack-resilient PMU network for power system operation," *IEEE Transactions on Smart Grid,* vol. 9, no. 3, pp. 1551-1565, 2016.

[24] A. Golshani, W. Sun, Q. Zhou, Q. P. Zheng, and J. Tong, "Two-stage adaptive restoration decision support system for a self-healing power grid," *IEEE Transactions on Industrial Informatics,* vol. 13, no. 6, pp. 2802-2812, 2017.

[25] A. Golshani, W. Sun, Q. Zhou, Q. P. Zheng, J. Wang, and F. Qiu, "Coordination of wind farm and pumped-storage hydro for a self-healing power grid," *IEEE Transactions on Sustainable Energy,* vol. 9, no. 4, pp. 1910-1920, 2018.

[26] A. Golshani, W. Sun, and K. Sun, "Advanced power system partitioning method for fast and reliable restoration: toward a self-healing power grid," *IET Generation, Transmission & Distribution,* vol. 12, no. 1, pp. 42-52, 2018.

[27] M. Zadsar, M. R. Haghifam, and S. M. Miri Larimi, "Approach for self-healing resilient operation of active distribution network with microgrid," *IET Generation, Transmission & Distribution,* vol. 11, no. 18, pp. 4633-4643, 2017.

[28] A. Elmitwally, M. Elsaid, M. Elgamal, and Z. Chen, "A fuzzy-multiagent self-healing scheme for a distribution system with distributed generations," *IEEE Transactions on Power Systems,* vol. 30, no. 5, pp. 2612-2622, 2014.

[29] J. B. Leite and J. R. S. Mantovani, "Development of a self-healing strategy with multiagent systems for distribution networks," *IEEE Transactions on Smart Grid,* vol. 8, no. 5, pp. 2198-2206, 2016.
[30] Z. Wang, B. Chen, J. Wang, and C. Chen, "Networked microgrids for self-healing power systems," *IEEE Transactions on smart grid,* vol. 7, no. 1, pp. 310-319, 2015.
[31] A. Sujil, R. Kumar, and R. C. Bansal, "Multiagent-based autonomous energy management system with self-healing capabilities for a microgrid," *IEEE Transactions on Industrial Informatics,* vol. 15, no. 12, pp. 6280-6290, 2018.
[32] Z. Wang, B. Chen, and J. Wang, "Decentralized energy management system for networked microgrids in grid-connected and islanded modes," *IEEE Transactions on Smart Grid,* vol. 7, no. 2, pp. 1097-1105, 2015.
[33] WEC, "World Energy Trilemma Index," ed: World Energy Council London, UK, 2018.
[34] The Active Building Centre (ABC) [Online] Available: https://es.catapult.org.uk/about/active-building-centre/
[35] B. Mohammadi-Ivatloo and F. Jabari, *Operation, planning, and analysis of energy storage systems in smart energy hubs*. Springer, 2018.
[36] S. Bracco, F. Delfino, G. Piazza, F. Foiadelli, and M. Longo, "Nanogrids with renewable sources, electrical storage and vehicle-to-home systems in the household sector: analysis for a single-family dwelling," in *2019 IEEE Milan PowerTech*, 2019: IEEE, pp. 1-6.
[37] W. Tushar, T. K. Saha, C. Yuen, D. Smith, and H. V. Poor, "Peer-to-peer trading in electricity networks: An overview," *IEEE transactions on smart grid,* vol. 11, no. 4, pp. 3185-3200, 2020.
[38] B. Nordman and K. Christensen, "Local power distribution with nanogrids," in *2013 International green computing conference proceedings*, 2013: Ieee, pp. 1-8.
[39] M. Ban, M. Shahidehpour, J. Yu, and Z. Li, "A cyber-physical energy management system for optimal sizing and operation of networked nanogrids with battery swapping stations," *IEEE Transactions on Sustainable Energy,* vol. 10, no. 1, pp. 491-502, 2017.
[40] H. Lotfi and A. Khodaei, "AC versus DC microgrid planning," *IEEE Transactions on Smart Grid,* vol. 8, no. 1, pp. 296-304, 2015.
[41] H. Lotfi and A. Khodaei, "Hybrid AC/DC microgrid planning," *Energy,* vol. 118, pp. 37-46, 2017.
[42] R. P. Chandrasena, F. Shahnia, A. Ghosh, and S. Rajakaruna, "Operation and control of a hybrid AC-DC nanogrid for future community houses," in *2014 Australasian Universities Power Engineering Conference (AUPEC)*, 2014: IEEE, pp. 1-6.
[43] S. Senemar, M. Rastegar, M. Dabbaghjamanesh, and N. Hatziargyriou, "Dynamic structural sizing of residential energy hubs," *IEEE Transactions on Sustainable Energy,* vol. 11, no. 3, pp. 1236-1246, 2019.
[44] N. Liu *et al.*, "Online energy sharing for nanogrid clusters: A Lyapunov optimization approach," *IEEE Transactions on Smart Grid,* vol. 9, no. 5, pp. 4624-4636, 2017.
[45] S. Teleke, L. Oehlerking, and M. Hong, "Nanogrids with energy storage for future electricity grids," in *2014 IEEE PES T&D Conference and Exposition*, 2014: IEEE, pp. 1-5.

[46] M. Heidari, T. Niknam, M. Zare, and S. Niknam, "Integrated battery model in cost-effective operation and load management of grid-connected smart nano-grid," *IET Renewable Power Generation,* vol. 13, no. 7, pp. 1123-1131, 2019.

[47] M. R. Sandgani and S. Sirouspour, "Energy management in a network of grid-connected microgrids/nanogrids using compromise programming," *IEEE Transactions on Smart Grid,* vol. 9, no. 3, pp. 2180-2191, 2016.

[48] H. Farzin, M. Fotuhi-Firuzabad, and M. Moeini-Aghtaie, "A stochastic multi-objective framework for optimal scheduling of energy storage systems in microgrids," *IEEE Transactions on Smart Grid,* vol. 8, no. 1, pp. 117-127, 2016.

[49] N. B. Arias, A. Tabares, J. F. Franco, M. Lavorato, and R. Romero, "Robust joint expansion planning of electrical distribution systems and EV charging stations," *IEEE Transactions on Sustainable Energy,* vol. 9, no. 2, pp. 884-894, 2017.

[50] S. Sheng, P. Li, C.-T. Tsu, and B. Lehman, "Optimal power flow management in a photovoltaic nanogrid with batteries," in *2015 IEEE Energy Conversion Congress and Exposition (ECCE)*, 2015: IEEE, pp. 4222-4228.

[51] J. Kumar, A. Agarwal, and N. Singh, "PV fed hybrid energy storage system supported DC microgrid," in *2019 IEEE 1st International conference on energy, systems and information processing (ICESIP)*, 2019: IEEE, pp. 1-6.

[52] J. Kumar, A. Agarwal, and N. Singh, "Design, operation and control of a vast DC microgrid for integration of renewable energy sources," *Renewable Energy Focus,* vol. 34, pp. 17-36, 2020.

[53] J. Kumar, A. Agarwal, and N. Singh, "Multipurpose water storage tank based DC microgrid system for isolated communities," *Energy Storage,* vol. 4, no. 4, p. e308, 2022.

[54] J. Kumar, A. Agarwal, and V. Agarwal, "Optimized design of mini-grid system for hilly region," *IETE Journal of Research,* vol. 68, no. 1, pp. 678-689, 2022.

[55] R. A. G. Burbano, M. L. O. Gutierrez, J. A. Restrepo, and F. G. Guerrero, "IED design for a small-scale microgrid using IEC 61850," *IEEE Transactions on Industry Applications,* vol. 55, no. 6, pp. 7113-7121, 2019.

[56] E. Shirazi and S. Jadid, "Cost reduction and peak shaving through domestic load shifting and DERs," *Energy,* vol. 124, pp. 146-159, 2017.

[57] H. Firoozi and H. Khajeh, "Optimal day-ahead scheduling of distributed generations and controllable appliances in microgrid," in *2016 Smart Grids Conference (SGC)*, 2016: IEEE, pp. 1-6.

[58] A. Azarhooshang, D. Sedighizadeh, and M. Sedighizadeh, "Two-stage stochastic operation considering day-ahead and real-time scheduling of microgrids with high renewable energy sources and electric vehicles based on multi-layer energy management system," *Electric Power Systems Research,* vol. 201, p. 107527, 2021.

[59] B. Ramachandran, S. K. Srivastava, and D. A. Cartes, "Intelligent power management in micro grids with EV penetration," *Expert Systems with Applications,* vol. 40, no. 16, pp. 6631-6640, 2013.

[60] M. Beaudin and H. Zareipour, "Home energy management systems: A review of modelling and complexity," *Renewable and sustainable energy reviews,* vol. 45, pp. 318-335, 2015.

[61] T. Sattarpour, D. Nazarpour, and S. Golshannavaz, "A multi-objective HEM strategy for smart home energy scheduling: A collaborative approach to support microgrid operation," *Sustainable cities and society,* vol. 37, pp. 26-33, 2018.

[62] K. H. Chua, Y. S. Lim, and S. Morris, "Battery energy storage system for peak shaving and voltage unbalance mitigation," *International Journal of Smart Grid and Clean Energy,* vol. 2, no. 3, pp. 357-363, 2013.

[63] M. AL-Dhaifallah, Z. M. Ali, M. Alanazi, S. Dadfar, and M. H. Fazaeli, "An efficient short-term energy management system for a microgrid with renewable power generation and electric vehicles," *Neural Computing and Applications,* vol. 33, no. 23, pp. 16095-16111, 2021.

[64] P. S. Kumar, R. Chandrasena, V. Ramu, G. Srinivas, and K. V. S. M. Babu, "Energy management system for small scale hybrid wind solar battery based microgrid," *IEEE access,* vol. 8, pp. 8336-8345, 2020.

[65] Short-Circuit Currents in DC Auxiliary Installations in Power Plants and Substations, IEC 61660 series [Online] Available: https://webstore.iec.ch/publication/5700

[66] S. Skok, S. Tesnjak, and S. Stefan, "Transient analysis of auxiliary DC installations in power plants and substations," in *2004 IEEE/PES Transmision and Distribution Conference and Exposition: Latin America (IEEE Cat. No. 04EX956)*, 2004: IEEE, pp. 277-280.

[67] A. Vicenzutti, E. De Din, and G. Sulligoi, "Transient short circuit analysis in DC on-board distribution systems fed by synchronous generators through 6-pulse diode rectifiers," in *2015 International Conference on Electrical Systems for Aircraft, Railway, Ship Propulsion and Road Vehicles (ESARS)*, 2015: IEEE, pp. 1-6.

[68] A. Vicenzutti, G. Sulligoi, R. Cuzner, and V. Singh, "Simplified analytical modeling and experimental validation of diode bridge rectifier operation during rail-to-rail short-circuit faults in synchronous generator-fed DC distribution systems," in *2017 IEEE Second International Conference on DC Microgrids (ICDCM)*, 2017: IEEE, pp. 596-601.

[69] R. Bleilevens and A. Moser, "Algebraic modelling of converters without DC fault ride-through capability for short circuit current calculation of DC distribution grids," in *2018 53rd international universities power engineering conference (UPEC)*, 2018: IEEE, pp. 1-6.

[70] A. Wasserrab and G. Balzer, "Calculation of short circuit currents in HVDC systems," in *2011 46th International Universities' Power Engineering Conference (UPEC)*, 2011: VDE, pp. 1-6.

[71] J. Das, "Arc flash hazard calculations in LV & MV DC systems-part i-short-circuit calculations," in *Conference Record of 2013 Annual IEEE Pulp and Paper Industry Technical Conference (PPIC)*, 2013: IEEE, pp. 81-92.

[72] N. M. Santos, V. F. Pires, and J. F. Silva, "The HVDC dual transmission system under DC short-circuit faults," in *2019 IEEE 28th International Symposium on Industrial Electronics (ISIE)*, 2019: IEEE, pp. 1002-1007.

[73] P. V. Radu, M. Lewandowski, A. Szelag, and M. Steczek, "Short-circuit fault current modeling of a dc light rail system with a wayside energy storage device," *Energies,* vol. 15, no. 10, p. 3527, 2022.

[74] Railway Applications - Fixed Installations - D.C. Switchgear Part 1: EN 50123-1:2003 General [Online] Available: https://standards.iteh.ai/catalog/standards/clc/88485d43-0340-4863-a98e-b57ba84f7041/en-50123-1-2003

[75] S. Wang, G. Zheng, Y. Zhao, W. Zhang, and X. Li, "Single-ended Protection Scheme For VSC-HVDC Grids Based On High-Frequency Component Of Fault Current," *Journal of Applied Science and Engineering,* vol. 26, no. 2, pp. 185-195, 2022.

[76] I. Almutairy and M. Alluhaidan, "Protecting a low voltage DC microgrid during short-circuit using solid-state switching devices," in *2017 IEEE Green Energy and Smart Systems Conference (IGESSC)*, 2017: IEEE, pp. 1-6.

[77] L. Yixiang, W. Xiangheng, W. Shanming, S. Pengsheng, and M. Weiming, "Analysis of the DC side sudden short circuit of three-phase/twelve-phase synchronous generator system," in *PowerCon 2000. 2000 International Conference on Power System Technology. Proceedings (Cat. No. 00EX409)*, 2000, vol. 2: IEEE, pp. 903-908.

[78] S. Moussa, M. J. B. Ghorbal, J. A. Ziani, and I. Slama-Belkhodja, "Residual-based short-circuit fault detection and isolation in LVDC microgrid," *Sustainable Energy Technologies and Assessments,* vol. 54, p. 102803, 2022.

[79] S. Yuan, J. Yan, Y. Yu, C. Zhao, G. Su, and X. Li, "Calculation method of short-circuit fault current in flexible DC grid," *Energy Reports,* vol. 8, pp. 461-468, 2022.

[80] B. Li, X. Jiao, W. Wen, W. Wang, and B. Li, "Study on calculation method for steady-state short-circuit current of MMC during a DC pole-to-pole fault," *IEEE Transactions on Power Delivery,* vol. 37, no. 4, pp. 2492-2502, 2021.

[81] X. Feng, L. Qi, and Z. Wang, "Estimation of short circuit currents in mesh DC networks," in *2014 IEEE PES General Meeting| Conference & Exposition*, 2014: IEEE, pp. 1-5.

[82] M. M. A. Abdelaziz, H. E. Farag, E. F. El-Saadany, and Y. A.-R. I. Mohamed, "A novel and generalized three-phase power flow algorithm for islanded microgrids using a newton trust region method," *IEEE transactions on power systems,* vol. 28, no. 1, pp. 190-201, 2012.

[83] S. Chopra, G. M. Vanaprasad, G. D. A. Tinajero, N. Bazmohammadi, J. C. Vasquez, and J. M. Guerrero, "Power-flow-based energy management of hierarchically controlled islanded AC microgrids," *International Journal of Electrical Power & Energy Systems,* vol. 141, p. 108140, 2022.

[84] M. H. Moradi, V. B. Foroutan, and M. Abedini, "Power flow analysis in islanded Micro-Grids via modeling different operational modes of DGs: A review and a new approach," *Renewable and Sustainable Energy Reviews,* vol. 69, pp. 248-262, 2017.

[85] G. D. A. Tinajero, M. Nasir, J. C. Vasquez, and J. M. Guerrero, "Comprehensive power flow modelling of hierarchically controlled AC/DC hybrid islanded microgrids," *International Journal of Electrical Power & Energy Systems,* vol. 127, p. 106629, 2021.

[86] H. M. Ahmed, A. B. Eltantawy, and M. Salama, "A generalized approach to the load flow analysis of AC–DC hybrid distribution systems," *IEEE Transactions on Power Systems,* vol. 33, no. 2, pp. 2117-2127, 2017.

[87] E. Aprilia, K. Meng, M. Al Hosani, H. H. Zeineldin, and Z. Y. Dong, "Unified power flow algorithm for standalone AC/DC hybrid microgrids," *IEEE Transactions on smart grid,* vol. 10, no. 1, pp. 639-649, 2017.

[88] A. A. Hamad, M. A. Azzouz, and E. F. El Saadany, "A sequential power flow algorithm for islanded hybrid AC/DC microgrids," *IEEE Transactions on Power Systems,* vol. 31, no. 5, pp. 3961-3970, 2015.

[89] I. M. U. M. Newton, "A Novel Approach to Solve Power Flow for Islanded Microgrids Using Modified Newton Raphson with Droop Control of DG."

[90] M. E. Nassar, A. A. Hamad, M. Salama, and E. F. El-Saadany, "A novel load flow algorithm for islanded AC/DC hybrid microgrids," *IEEE Transactions on Smart Grid,* vol. 10, no. 2, pp. 1553-1566, 2017.

[91] A. Eajal, M. A. Abdelwahed, E. El-Saadany, and K. Ponnambalam, "A unified approach to the power flow analysis of AC/DC hybrid microgrids," *IEEE Transactions on sustainable energy,* vol. 7, no. 3, pp. 1145-1158, 2016.

[92] G. Agundis-Tinajero *et al.*, "Extended-optimal-power-flow-based hierarchical control for islanded AC microgrids," *IEEE Transactions on Power Electronics,* vol. 34, no. 1, pp. 840-848, 2018.

[93] M. Zolfaghari, M. Abedi, and G. B. Gharehpetian, "Power flow control of interconnected AC–DC microgrids in grid-connected hybrid microgrids using modified UIPC," *IEEE Transactions on Smart Grid,* vol. 10, no. 6, pp. 6298-6307, 2019.

[94] P. C. Loh, D. Li, Y. K. Chai, and F. Blaabjerg, "Autonomous control of interlinking converter with energy storage in hybrid AC–DC microgrid," *IEEE transactions on industry applications,* vol. 49, no. 3, pp. 1374-1382, 2013.

[95] F. Nejabatkhah and Y. W. Li, "Overview of power management strategies of hybrid AC/DC microgrid," *IEEE Transactions on power electronics,* vol. 30, no. 12, pp. 7072-7089, 2014.

[96] Z. Yi, W. Dong, and A. H. Etemadi, "A unified control and power management scheme for PV-battery-based hybrid microgrids for both grid-connected and islanded modes," *IEEE Transactions on Smart Grid,* vol. 9, no. 6, pp. 5975-5985, 2017.

[97] J.-H. Teng, S.-W. Luan, D.-J. Lee, and Y.-Q. Huang, "Optimal charging/discharging scheduling of battery storage systems for distribution systems interconnected with sizeable PV generation systems," *IEEE Transactions on Power Systems,* vol. 28, no. 2, pp. 1425-1433, 2012.

[98] B. Papari, C. S. Edrington, I. Bhattacharya, and G. Radman, "Effective energy management of hybrid AC–DC microgrids with storage devices," *IEEE transactions on smart grid,* vol. 10, no. 1, pp. 193-203, 2017.

[99] P. Teimourzadeh Baboli, M. Shahparasti, M. Parsa Moghaddam, M. R. Haghifam, and M. Mohamadian, "Energy management and operation modelling of hybrid AC–DC microgrid," *IET Generation, Transmission & Distribution,* vol. 8, no. 10, pp. 1700-1711, 2014.

[100] A. A. A. Radwan and Y. A.-R. I. Mohamed, "Networked control and power management of AC/DC hybrid microgrids," *IEEE Systems Journal,* vol. 11, no. 3, pp. 1662-1673, 2014.

[101] Z. S. Molaee, E. Rokrok, and M. Doostizadeh, "A unified power flow approach using VSC-efficiency for AC-DC distribution systems operating at grid connected and islanded modes," *International Journal of Electrical Power & Energy Systems,* vol. 130, p. 106906, 2021.
[102] C. Liu, B. Zhang, Y. Hou, F. F. Wu, and Y. Liu, "An improved approach for AC-DC power flow calculation with multi-infeed DC systems," *IEEE Transactions on Power Systems,* vol. 26, no. 2, pp. 862-869, 2010.
[103] Y.-S. Tzeng, N. Chen, and R.-N. Wu, "A detailed RL fed bridge converter model for power flow studies in industrial AC/DC power systems," *IEEE Transactions on Industrial Electronics,* vol. 42, no. 5, pp. 531-538, 1995.
[104] L. Jia, Y. Zhu, S. Du, and Y. Wang, "Analysis of the transition between multiple operational modes for hybrid AC/DC microgrids," *CSEE Journal of power and Energy Systems,* vol. 4, no. 1, pp. 49-57, 2018.
[105] Renewable Energy Report
[106] Eurostat, Energy, transport and environment statistic [Online] Available: https://ec.europa.eu/eurostat/web/products-statistical-books/-/ks-dk-20-001
[107] A. K. Raturi, "Renewables 2019 global status report," 2019.
[108] T. SpA, "Snam SpA,“Documento di descrizione degli scenari 2022”," *Italian. Available online: https://download. terna. it/terna/Documento_Descrizione_Scenari_2022_8da74044f6ee28d. pdf.*
[109] I. IRENA, "global energy transformation: A roadmap to 2050 (2019 edition), international renewable energy agency," abu dhabi, Tech. rep, 2019.
[110] E. IRENA, "storage and renewables: Costs and markets to 2030, 2017," ed.
[111] "Analisi di impatto dell’introduzione della tariffa bioraria obbligatoria," RSE, 2012. [Online]. Available: https://www.rse-web.it/rapporti/analisi-di-impatto-dellintroduzione-della-tariffa-bioraria-obbligatoria-315241/
[112] ARERA, Dati sulla continuità del servizio elettrico [Online] Available: https://www.arera.it/sasfrontendcse/estrattoreLink
[113] H. Farzin, M. Fotuhi-Firuzabad, and M. Moeini-Aghtaie, "Stochastic energy management of microgrids during unscheduled islanding period," *IEEE Transactions on Industrial Informatics,* vol. 13, no. 3, pp. 1079-1087, 2016.
[114] "GAMS, Cplex 12." GAMS. https://www.gams.com/33/docs/S_CPLEX.html (accessed.
[115] A. R. Jordehi, "How to deal with uncertainties in electric power systems? A review," *Renewable and sustainable energy reviews,* vol. 96, pp. 145-155, 2018.
[116] "PNIEC (piano nazionale integrato per l’energia e il clima)," 2019. [Online]. Available: https://www.mimit.gov.it/images/stories/documenti/PNIEC_finale_17012020.pdf
[117] A. Sangwongwanich, Y. Yang, and F. Blaabjerg, "High-performance constant power generation in grid-connected PV systems," *IEEE Transactions on Power Electronics,* vol. 31, no. 3, pp. 1822-1825, 2015.
[118] A. Sangwongwanich, Y. Yang, F. Blaabjerg, and H. Wang, "Benchmarking of constant power generation strategies for single-phase grid-connected photovoltaic systems," *IEEE Transactions on Industry Applications,* vol. 54, no. 1, pp. 447-457, 2017.

[119] L. Qu and W. Qiao, "Constant power control of DFIG wind turbines with supercapacitor energy storage," *IEEE Transactions on Industry Applications,* vol. 47, no. 1, pp. 359-367, 2010.
[120] Solar home electricity data. (2014) Ausgrid [Online] Available: https://www.ausgrid.com.au/Industry/Our-Research/Data-to share/ Solar-home-electricitydata.
[121] Electric cars available in Australia [Online] Available: https://www.canstarblue.com.au/vehicles/electric-cars-available-australia/
[122] Journey to work in Australia [Online] Available: https://www.abs.gov.au/ausstats/abs@.nsf/Lookup/by.
[123] Distributed Generation Renewable Energy Estimate of Costs [Online] Available: https://www.nrel.gov/analysis/tech lcoe re cost est.html.
[124] S. M. Schoenung, "Energy storage systems cost update: a study for the DOE Energy Storage Systems Program," Sandia National Laboratories (SNL), Albuquerque, NM, and Livermore, CA …, 2011.
[125] List of Converters Prices [Online] Available: https://www.alibaba.com/trade/search?fsb=y&IndexArea=product
[126] Converters [Online] Available: https://www.amazon.com/s?k=converter&ref=nb sb noss.
[127] "ARERA, "Energia Elettrica, Condizioni economiche per i clienti del Servizio di maggior tutela"." https://www.autorita.energia.it/allegati/dati_documenti/prezzi//elettricitanon-domestici.xls. (accessed.
[128] H. M. Ahmed, A. B. Eltantawy, and M. M. Salama, "A planning approach for the network configuration of AC-DC hybrid distribution systems," *IEEE Transactions on Smart Grid,* vol. 9, no. 3, pp. 2203-2213, 2016.
[129] J. M. Guerrero, J. C. Vasquez, J. Matas, L. G. De Vicuña, and M. Castilla, "Hierarchical control of droop-controlled AC and DC microgrids—A general approach toward standardization," *IEEE Transactions on industrial electronics,* vol. 58, no. 1, pp. 158-172, 2010.
[130] L. Che, M. Shahidehpour, A. Alabdulwahab, and Y. Al-Turki, "Hierarchical coordination of a community microgrid with AC and DC microgrids," *IEEE Transactions on smart grid,* vol. 6, no. 6, pp. 3042-3051, 2015.
[131] F. Mumtaz, M. Syed, M. Al Hosani, and H. Zeineldin, "A novel approach to solve power flow for islanded microgrids using modified Newton Raphson with droop control of DG," *IEEE transactions on sustainable energy,* vol. 7, no. 2, pp. 493-503, 2015.
[132] J. Rocabert, A. Luna, F. Blaabjerg, and P. Rodriguez, "Control of power converters in AC microgrids," *IEEE transactions on power electronics,* vol. 27, no. 11, pp. 4734-4749, 2012.
[133] S. Peyghami, H. Mokhtari, and F. Blaabjerg, "Autonomous operation of a hybrid AC/DC microgrid with multiple interlinking converters," *IEEE Transactions on Smart Grid,* vol. 9, no. 6, pp. 6480-6488, 2017.
[134] J. C. Vasquez, J. M. Guerrero, A. Luna, P. Rodríguez, and R. Teodorescu, "Adaptive droop control applied to voltage-source inverters operating in grid-connected and

islanded modes," *IEEE transactions on industrial electronics,* vol. 56, no. 10, pp. 4088-4096, 2009.

[135] S. Moradi, G. Zizzo, S. Favuzza, and F. Massaro, "A stochastic approach for self-healing capability evaluation in active islanded AC/DC hybrid microgrids," *Sustainable Energy, Grids and Networks,* vol. 33, p. 100982, 2023.

[136] S. Moradi, V. Vahidinasab, and G. Zizzo, "Optimal nanogrid planning at building level," *International Journal of Electrical Power & Energy Systems,* vol. 153, p. 109409, 2023.

[137] https://zenodo.org/communities/hyperride/records?q=&l=list&p=1&s=10&sort=newest (accessed.

[138] S. Favuzza, M. Mitolo, R.Musca, andG. Zizzo, "Short-circuit calculations in hybrid AC/DC microgrids," in Proc. IEEE/IAS 58th Ind. Commercial Power Syst. Tech. Conf., 2022, pp. 1–6.

[139] IEEE Recommended Practice for the Design of DC Power Systems for Stationary Applications, IEEE Standard 946-2020, Piscataway, NJ, USA, 2020.